1972

Reaction mechanism and mechanics in shale-induced concrete popouts

Derwin Crockett Merrill
Iowa State University

Recommended Citation

Merrill, Derwin Crockett, "Reaction mechanism and mechanics in shale-induced concrete popouts " (1972). *Retrospective Theses and Dissertations*. 5268.
https://lib.dr.iastate.edu/rtd/5268

INFORMATION TO USERS

This dissertation was produced from a microfilm copy of the original document. While the most advanced technological means to photograph and reproduce this document have been used, the quality is heavily dependent upon the quality of the original submitted.

The following explanation of techniques is provided to help you understand markings or patterns which may appear on this reproduction.

1. The sign or "target" for pages apparently lacking from the document photographed is "Missing Page(s)". If it was possible to obtain the missing page(s) or section, they are spliced into the film along with adjacent pages. This may have necessitated cutting thru an image and duplicating adjacent pages to insure you complete continuity.

2. When an image on the film is obliterated with a large round black mark, it is an indication that the photographer suspected that the copy may have moved during exposure and thus cause a blurred image. You will find a good image of the page in the adjacent frame.

3. When a map, drawing or chart, etc., was part of the material being photographed the photographer followed a definite method in "sectioning" the material. It is customary to begin photoing at the upper left hand corner of a large sheet and to continue photoing from left to right in equal sections with a small overlap. If necessary, sectioning is continued again — beginning below the first row and continuing on until complete.

4. The majority of users indicate that the textual content is of greatest value, however, a somewhat higher quality reproduction could be made from "photographs" if essential to the understanding of the dissertation. Silver prints of "photographs" may be ordered at additional charge by writing the Order Department, giving the catalog number, title, author and specific pages you wish reproduced.

University Microfilms

300 North Zeeb Road
Ann Arbor, Michigan 48106

A Xerox Education Company

72-26,933

MERRILL, Derwin Crockett, 1934-
REACTION MECHANISM AND MECHANICS IN
SHALE-INDUCED CONCRETE POPOUTS.

Iowa State University, Ph.D., 1972
Engineering, civil

University Microfilms, A XEROX Company, Ann Arbor, Michigan

Reaction mechanism and mechanics in shale-induced concrete popouts

by

Derwin Crockett Merrill

A Dissertation Submitted to the
Graduate Faculty in Partial Fulfillment of
The Requirements for the Degree of
DOCTOR OF PHILOSOPHY

Major: Civil Engineering

Approved:

Signature was redacted for privacy.

In Charge of Major Work

Signature was redacted for privacy.

For the Major Department

Signature was redacted for privacy.

For the Graduate College

Iowa State University
Ames, Iowa

1972

TABLE OF CONTENTS

TABLE OF CONTENTS (Continued)

PART I. REACTION MECHANISM

INTRODUCTION

Certain shale particles located near the surface in portland cement concrete cause a surface blemish called a concrete popout. The concrete popouts studied in this investigation were nearly conical in shape and about 1/16 inch deep and from 1/8 to 1/2 inch in diameter at the surface. A plan view photograph of actual popouts on a floor with a red colored surface is shown in Figure 1. Popouts on an uncolored floor are shown in Figure 2. At the apex of each conical popout there was a small shale particle varying in color from light grey to almost black. The popout at the bottom-center of the photograph in Figure 2 clearly shows the shale particle location near the center of the popout crater. The bottom view of concrete popouts shown by the photomicrographs in Figures 3 and 4 also clearly display the reactive shale aggregate.

Popouts have long been regarded as a nuisance in Iowa and adjoining states. The problem is becoming more serious because of the increased use of smooth finished concrete. Popouts are especially objectionable in permanently colored concrete floors since the underlying uncolored concrete is exposed by the popout.

Discussions with concrete producers and tradesmen indicated that they believed the popouts resulted when water caused the shale to swell. The simple expansion due to absorption of water seemed unlikely since the shale-containing aggregate is usually taken from below the water table, has been wet for thousands of years, and is generally not dried before it is put into the concrete. It was therefore concluded that

Figure 1. Concrete popouts on a red floor

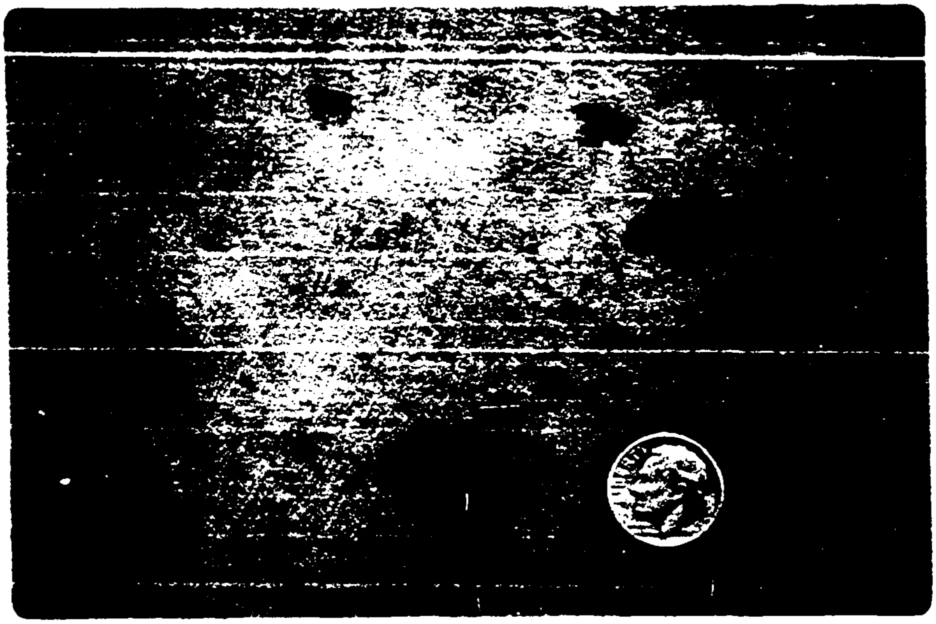

Figure 2. Concrete popouts on an uncolored floor

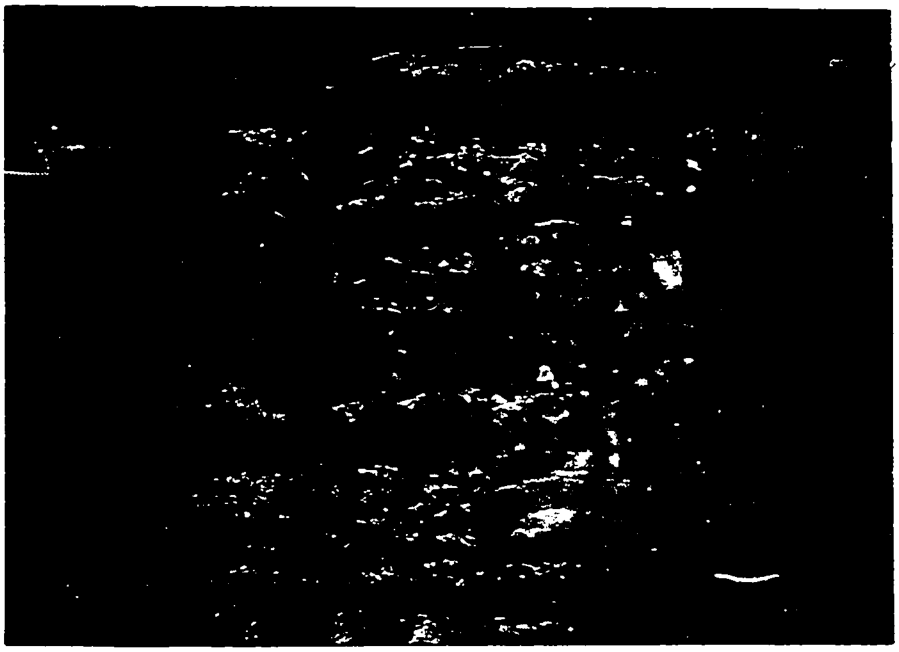

Figure 3. Concrete popout--bottom view

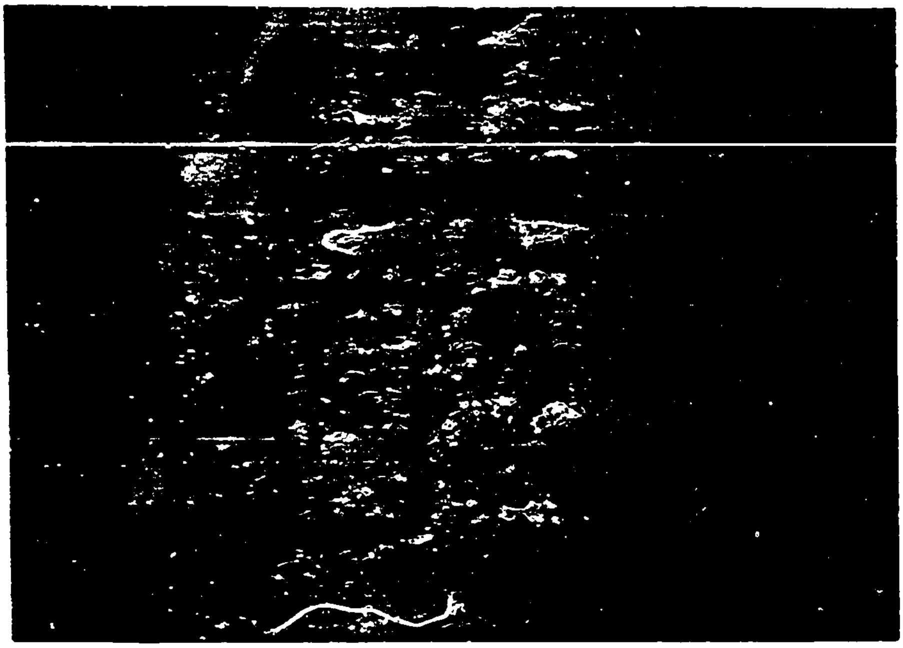

Figure 4. Photomicrograph of expansive shale in a concrete popout

the reaction must be chemical in nature rather than physical.

Conversations with people concerned with the popout problem also revealed that they were unable to obtain concrete popouts in laboratory specimens. Also, the field conditions resulting in popouts seemed quite variable and, therefore, unpredictable.

CASE HISTORIES

Since, as previously indicated, the variables that affect concrete popouts were not well defined, a rather thorough field investigation was undertaken to determine what these variables were. The case histories summarized below are representative results of the field investigation.

Case 1. Tilt-up Slabs

Several tilt-up type slabs were cast on top of each other in a horizontal position. A bond breaker was placed between each slab and each slab was cured one day before the next slab was cast. Popouts occurred on both top and bottom surfaces of the slab. At the same time these tilt-up slabs were cast, an on-grade school floor was being placed with the same concrete mixture. No popouts occurred on the floor.

The concrete mixtures placed on both jobs contained the same cement, limestone coarse aggregate, sand, and admixtures, and were placed and finished by the same contractor. Some of the differences were: The haul distance was 1½ miles for the tilt-up slabs and 5 miles for the school floor. A bond breaker was used on the tilt-up slabs but not on the school floor. The tilt-up slabs were cast on top of each other.

Case 2. Tile-Covered Concrete

Concrete floors for a school were placed in the spring, covered with asphalt tile the next fall and used the following winter and spring.

No popouts were reported. The school was then closed up for the summer. Ventilation was lacking and some windows didn't have sun shades. The temperature and relative humidity inside the school were high. Even though the concrete was now over 1 year old, numerous popouts occurred creating bumps in the tile. Examination of a removed tile showed a shale particle in the center of each popout.

Case 3. Heated Concrete

In winter construction it is common practice to heat the aggregate and/or water used to make concrete. A floor was placed in a warm hospital basement using heated concrete. Numerous popouts had occurred by the morning after placement.

Case 4. Curing Compound-Covered Concrete

A curing compound was sprayed on part of a sidewalk, but the contractor ran out of the compound before spraying was completed. The part sprayed with curing compound popped; the rest of the sidewalk had no popouts.

Case 5. Painted Concrete

A four-year-old concrete floor showed no signs of popouts. The floor was then partially painted. Popouts occurred on the part of the floor that was painted but not on the part left exposed.

Case 6. Effects of Cement Brand

The west half of a warehouse floor was placed using one brand of cement and the east half was placed using a second brand of cement. All other concrete ingredients were the same. The west half of the floor experienced severe popouts, and the east half had very few popouts.

Case 7. Exuded Gel

A fire station floor on grade exhibited extensive popouts three days after placement. The floor was given a very smooth hard finish. A decision was made to take the floor out with a jackhammer. The replacement floor was also given a smooth hard finish and also had numerous popouts. One of the popouts grew like a mushroom, popping up on a stem of gel that apparently solidified as the stem was exposed to the air. Figure 5 is a photomicrograph of the popout perched on the gel stem.

Case 8. Water-Cleaned Concrete

A five-year-old home was sold. After moving in, the new owner washed down the basement floor with a water hose. The previously sound concrete exhibited rather severe popping even though the floor was five years old.

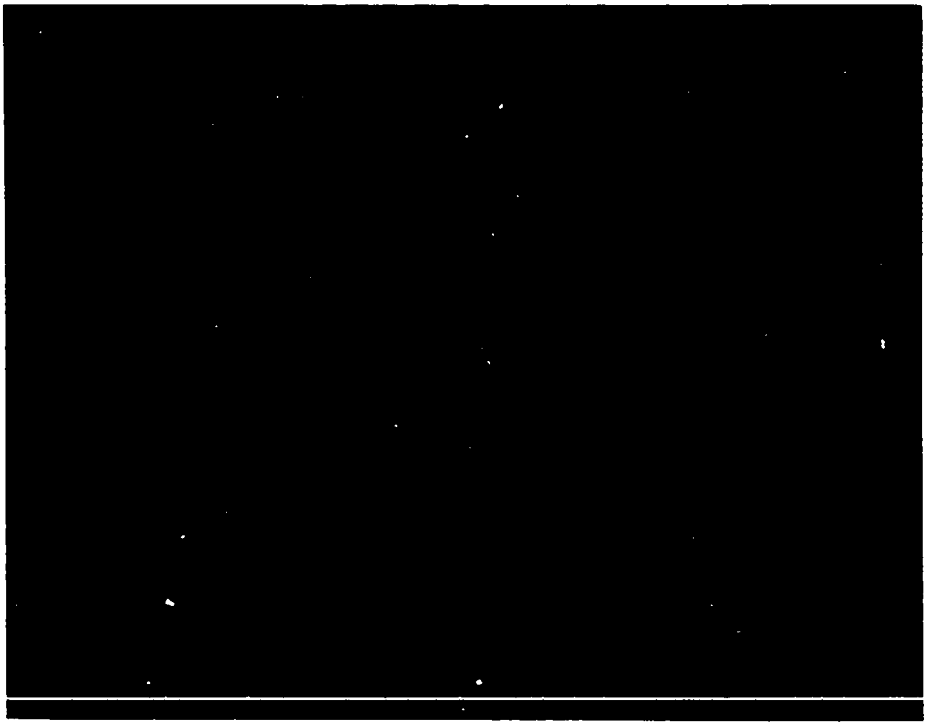

Figure 5. Photomicrograph of a popout perched on a gel stem

DISCUSSION OF CASE HISTORIES

The only apparent common denominator in all field investigations was the existence of a small black, brown, or grey shale particle at the apex of each concrete popout. Nearly all contractors, ready-mixed concrete producers, and tradesmen interviewed felt that the popouts were caused by the shale particles absorbing water and swelling. Case history 7 seemed to indicate that there was a chemical reaction involved rather than a simple physical swelling of the shale particle. Alkali-aggregate reaction was suspected.

The field investigation was of some help in determining the variables that affected concrete popouts but was not completely conclusive. It seemed that the cement brand had some affect upon the popout reaction (Case 6). Based upon Case 7 it was postulated that the reaction involved alkali in the cement attacking the shale to form an alkali-silica gel which can imbibe water and swell almost without bounds. For this hypothesis to be correct the shale must have a reactive silica present. The alkali content in the cement would then become a critical variable.

The higher the concrete temperature the greater the chance for popouts (Cases 1, 2, and 3). In Case 1, stacking of the tilt-up slabs one on top of the other at one day intervals would not allow the heat of hydration to be dissipated to the extent it would be in a single slab. This would raise the temperature of the concrete in the slabs and accelerate the deleterious popout reaction.

Tile, paint, and curing compounds increased the chances for concrete popouts (Cases 2, 4, and 5). Also the presence of water caused popouts (Case 8). The tile, paint, and curing compounds increased the relative humidity in the concrete as did the washing of the floor in Case 8. It was postulated that an increase in the relative humidity increased the chance for popouts to occur.

The type of finish affects the chances for popouts (Case 7). Apparently the smoother the finish the greater the chances for the popouts to occur. In fact, shale-induced concrete popouts on surfaces not finished with a trowel, such as walls, have not been reported as being a problem. Most case histories involved floors placed on the ground and given a smooth finish.

The field investigation indicated that the effects of the following variables upon the concrete popout reaction should be studied in the laboratory.

1. Temperature
2. Relative humidity
3. Alkali content of the cement
4. Type of finish applied to the concrete
5. Amount of sand-size shale present in the concrete.

LITERATURE REVIEW AND THEORY

A review of the literature revealed no published research on concrete popouts *per se* prior to this research. There is, however, a large amount of literature describing the effects of alkali attack on reactive aggregates to cause massive expansion and subsequent structural failure. The literature dealing with the mechanism involved in massive expansion will be reviewed because of the possible similarity to the expansion causing a concrete popout surface blemish.

Reactive Aggregates

Thomas E. Stanton (1) published the first paper attributing deleterious expansion of some concretes to a chemical reaction between the alkalis in the cement and reactive aggregates. Since that time much research has been done to elucidate the causes and effects of the reaction. Excellent historical reviews are available (2, 3).

The soluble alkalis Na_2O and K_2O present in portland cement attack aggregates that have silica in a reactive form. Some of the aggregates and aggregate constituents that are known to be reactive are opal, chalcedony, tridymite, cristobalite, zeolite, heulandite, and glassy to cryptocrystalline rhyolites, dacites, andesites (and their tuffs) and certain phyllites (4, 5, 6).

Opal is a highly condensed silica gel (7). In vitreous forms of silica and in silica gels the structure is random, whereas in crystalline forms of silica the structure is ordered (8). The random silica structure is subject to alkali attack, while an ordered silica structure such as quartz is not subject to alkali attack to any appreciable extent.

Carman (8) lists several methods of artificially forming silica sols, and indicates that the basic unit of a silica sol is orthosilicic acid (H_4SiO_4) which is a hydrated silicon-oxygen tetrahedron. The particle size of silica sols freshly formed in an aqueous solution increases with time. Eventually at concentrations greater than 1 percent the increasing silica sol particles will condense to form a gel which cannot be peptized in an aqueous solution, so the process is irreversible. Further drying causes gel shrinkage where more silicon-oxygen tetrahedra link to form a continuous three dimensional network with the composition of SiO_2. Tetrahedra in random arrangement result in amorphous silica such as opal, whereas in a regular or ordered arrangement they result in quartz, cristobalite or tridymite. When only two hydrated SiO_2 tetrahedra join, $H_6Si_2O_7$ results. When three tetrahedra join, $H_8Si_3O_{10}$ results, etc. Therefore the degree of surface hydration and the change from a sol to a gel to a rigid silica structure depends upon the number of joined silicon-oxygen tetrahedra. Carman (8) also indicates that alkalies such as NaOH added to a silica sol or gel can peptize the particles. Low NaOH concentrations will remove H^+ ions attached to the silica particles leaving a negative surface charge and Na^+ ions in the diffuse layer.

$$\text{-- Si --OH} + Na^+ + OH^- = \text{--Si --}O^- \, Na^+ + H_2O$$

Higher NaOH concentrations will break Si-O-Si links.

$$\text{--Si --O --Si--} + 2NaOH = 2 \text{ --Si --}O^- \, Na^+ + H_2O$$

At SiO_2:Na_2O molar ratios of 2:1 the solution probably contains NaH_3SiO_4 salt and at lower ratios the salts $Na_2\ H_2\ SiO_4$ and Na_4SiO_4 are formed (8, p. 970). Carman (8) represents unhydrated and hydrated silica surfaces by the two-dimensional diagram shown in Figure 6.

Reaction Mechanism

Powers and Steinour (7) used Carman's (8) two dimensional representation of unhydrated and hydrated silica to postulate a mechanism for alkali-aggregate reaction. As alkalis break O---H or Si---O bonds the degradation of the silica gel results in an alkali-silica which can imbibe water and swell almost without bounds. Kalousek's (9a) research presented an apparent anomoly. He showed that when SiO_2-aq was placed in water with Na_2O and CaO the solid phase in equilibrium with the solution was a non-expansive lime-alkali-silica complex. The swelling alkali-silica gel did not form in the presence of the Ca^{++} ion. Since the pore water in concrete always contains $Ca(OH)_2$ it would seem that on the basis of Kalousek's findings, a non-expansive lime-alkali-silica complex would form in preference to the swelling alkali-silica gel.

Powers and Steinour (7) suggested that the work of van der Burgh and Vivian may explain this apparent anomaly. Both showed that when a sodium silica gel was placed in a saturated $Ca(OH)_2$ solution a layer of white precipitate about 0.5 mm thick formed. This precipitate was evidently a lime-alkali-silica complex through which calcium ions could not pass but hydrogen and hydroxyl ions could pass. The sodium silica,

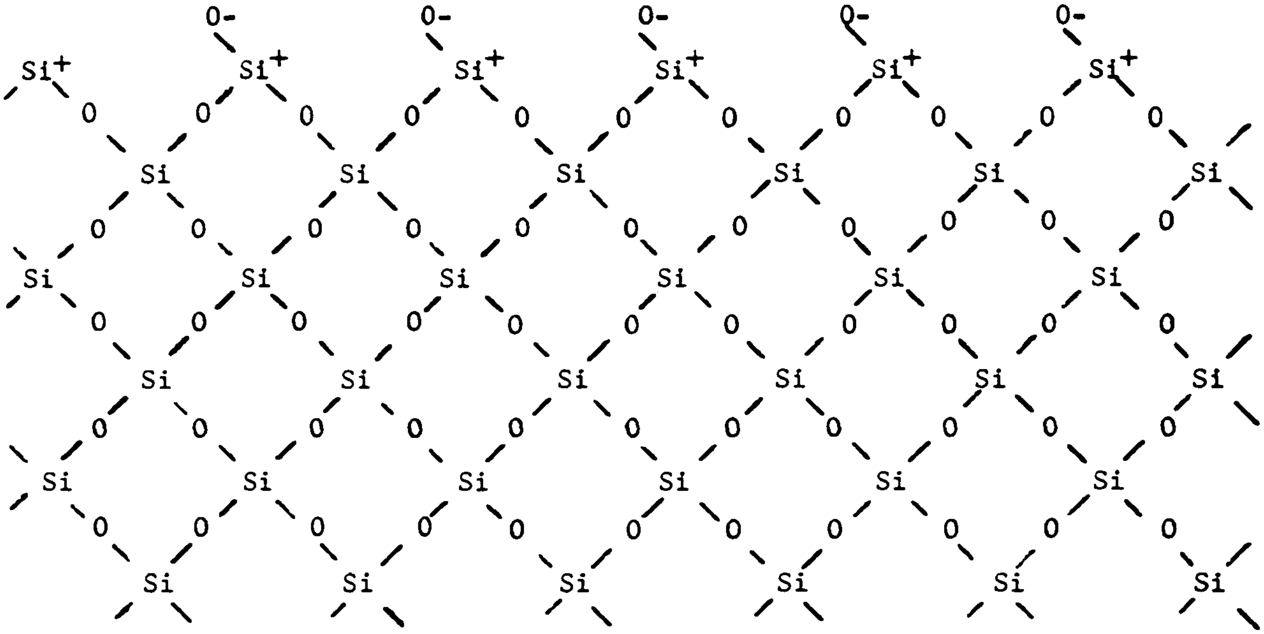

(a) Unhydrated surface

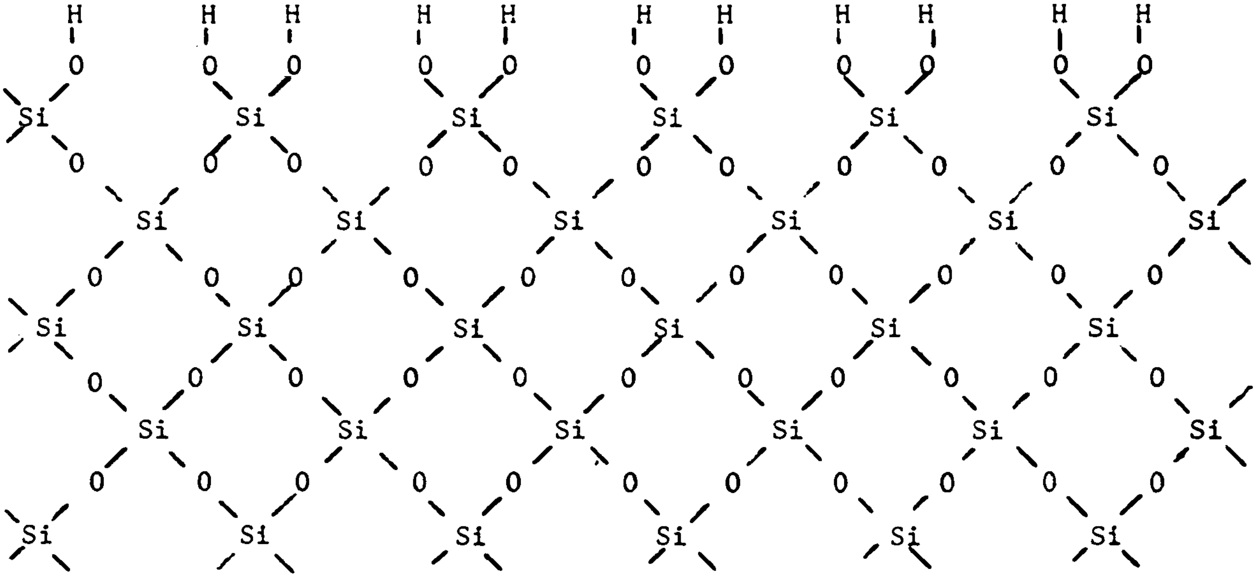

(b) Hydrated surface

Figure 6. Diagrammatic two-dimensional representation of silica structure

therefore, imbibed water and became less viscous. Powers and Steinour (7) concluded that when reactive aggregate is present in concrete

> ...the initial attack of the alkali and lime builds up a zone of lime-alkali-silica complex which, when it reaches requisite thickness, hinders the diffusion of calcium ions across the boundary region of the reactive particle but at the same time allows alkali and water to pass.
>
> ...When lime diffusion is hindered the alkali-aggregate reaction produces an expansive gel....

Osmotic pressure

When a solution is separated from the solvent by a membrane permeable to the solvent molecules but impermeable to the solute molecules a pressure in the solution is developed. This pressure is called osmotic pressure. It occurs because the chemical potential of the solvent in solution is less than the chemical potential of the pure solvent. Moore (9 b) indicates that the lowering of the chemical potential produced by the dilution of A in the solution is:

$$\Delta u = RT \ln \frac{P_A}{P_A^o} \qquad (1)$$

For chemical equilibrium this lowering of the potential must be exactly offset by an increase in the solution pressure, π.

$$\Delta u = \int_o^{\pi} \overline{V}_A \; dP \qquad (2)$$

For equilibrium: $\int_o^{\pi} \overline{V}_A \; dP = -RT \ln \frac{P_A}{P^o_A}$ (3)

Hansen (10) suggested that osmotic pressure is the mechanism whereby reactive aggregates expand: the hardened cement paste is considered to be the semi-permeable membrane, the solution is the alkali silicate, and the solvent is the concrete pore water. The membrane would permit alkali hydroxides and water to pass into an alkali silicate solution but would not allow silicate to pass out through the membrane to relieve pressures. Therefore osmotic pressures were considered responsible for the disruption of concrete containing alkalis and reactive aggregate.

McConnell *et al.* (2) confirmed Hansen's osmotic pressure theory by constructing a cell with a mortar disc separating distilled water from sodium silicate. Movement of water through the mortar disc and into the sodium silicate created pressures in excess of 550 psi, which was the maximum capacity of the pressure gauge. As the concentration of sodium silicate was increased the osmotic pressures developed also increased.

Gel swelling

Vivian (11) on the other hand, observed that mortar around opal cracked before the opal particle lost its well defined edge. He concluded, therefore, that expansion must be from opaline gel swelling rather than osmotic pressure of a sol or solution as proposed by Hansen.

Powers and Steinour (7) reconciled the apparent conflict between the "gel swelling" versus "osmotic pressure" theories of expansion by declaring that the actual mechanism could be either of the above depending upon the amount of moisture present. An opal aggregate can imbibe water and swell by a process similar to the expansion of a clay particle. The terms "solid", "gel", "sol", and "solution" are terms applied to differentiate between the state of dissolution of a solid, and clear-cut boundaries are non-existent. Van Olphen (12) indicated that a solid clay with only a few water layers could theoretically exert swelling pressures as high as 60,000 psi. Olson, Handy, and Demirel (13) measured the swelling pressure of the last five layers of water in calcium montmorillonite. The fourth and fifth layers exerted swelling pressures of between 0 and 92 psi; the third layer about 920 psi and the second layer between 11,400 and 16,000 psi. The swelling pressure of the first absorbed water layer could not be obtained since the machine capacity of 27,300 psi was insufficient to remove the first absorbed water layer. Therefore van Olphen's (12) 60,000 psi value seems to be high for all but the first water layer. He also indicated that if the clay platelets become separated by sufficient water then the electrical double-layer repulsion forces dominate rather than surface hydration energy. In this case the repulsive forces give rise to osmotic swelling pressures which are a function of platelet separation and can range from 147 psi for close particle spacing to 1.47 psi for wide particle separation (12).

The expansive pressures developed in an expanding sodium silica gel are probably very much like the expansive pressures developed by clay. The above literature indicates that the lower the water content of the gel the higher the pressures developed. No well defined line of demarkation between hydration pressures and osmotic pressures has been defined.

Osmotic pressures are lower than hydration pressures and are associated with a higher moisture content in the swelling complex.

Conversely, the higher hydration pressures are associated with a lower moisture content in the swelling complex.

CEMENT PROPERTIES

Type I Cement from Missouri

The cement used to make the concrete test slabs was Type I portland cement manufactured in 1967 from Kansas City, Missouri. The chemical analysis of the cement is given in Table 1.

Table 1. Chemical analysis of portland cement

Component	Percent	Component	Percent
CaO	64.7	Na_2O	0.22
SiO_2	22.5	K_2O	0.52
Al_2O_3	4.41	Total alkali as Na_2O	0.56
Fe_2O_3	2.23		
MgO	2.8	C_3S	53.5
SO_3	2.2	C_2S	24.2
Ignition loss	0.8	C3A	7.9
Insoluble residue	0.0	C_4AF	6.8

This particular cement was selected because the total alkali was 0.56 percent. ASTM Designation C33-64 requires that when deleteriously reactive materials are present in the fine aggregate either a cement containing less than 0.6 percent alkalies calculated as sodium oxide should be used or a pozzolanic material that will prevent harmful expansion should be used.

Type I Cements from Iowa

The alkali content of several Type I cements from Iowa, manufactured in 1967, was determined by a DU-2 spectrophotometer with an attached flame photometer. Standard solutions were prepared, a calibration curve obtained and the sample was digested and prepared all in accordance with the recommendations given in Chemical Analysis of Hydraulic Cement (ASTM Designation: C114-67). The alkali contents shown in Table 2 are the sum of sodium oxide (Na_2O) and potassium oxide (K_2O) converted to equivalent Na_2O.

Table 2. Iowa cement alkali content

Cement	% alkali
1	0.47
2	0.58
3	0.41
4	0.63
5	0.96
6	0.47
7	0.98
8	0.40
9	0.68
10	0.57

REACTIVE AGGREGATE IDENTIFICATION

Debye-Scherrer Powder Camera Measurements

The first phase of the experimental program was to determine the mineralogical composition of the sand-size shale particles which were at the apex of each concrete popout. Since the gathering of sufficient reactive particles for a diffractometer powder sample would be rather time-consuming, it was decided that the smaller camera powder sample would be used. Sufficient material for a Debye-Scherrer X-ray camera specimen was obtained by removing the reactive material from the apex of a concrete popout.

A reactive particle having cross-sectional dimensions of about 0.5 mm was partially embedded in modelling clay. The clay was then mounted on the shaft of the camera so that the reactive particle would be in direct line with the X-ray beam. A non-reacted shale particle was hand-picked from sand and X-rayed to compare the results with the reactive material causing the concrete popout.

The specimens were examined using a Debye-Scherrer camera and a Chromium X-ray tube with a vanadium filter. The exposed films were developed, dried, and reflection lines were measured with a millimeter scale fastened to a light box. From the camera radius, $r = 360^{\circ}/2\pi =$ 57.3 mm, a reflection distance measured in millimeters is equal to the diffraction angle, θ in degrees. The center of each reflection was estimated to the nearest 0.1 mm. In the case of wide reflections the width of the reflection was either measured or indicated as "medium" or "broad". The d-spacing value in Angstroms for each reflection was computed from Bragg's Law.

Results and Analysis

The d-spacing values for the reflections from the popout center and unreacted shale for 2θ values from 10° to 40° are shown in Table 3. All of the peaks except quartz were very broad. The width of the peaks for the unreacted shale is reported in Table 3. The broad nature of these peaks indicatesa fine crystallite size or poorly crystallized material.

Table 3. d-spacing values in Angstroms of reflections from X-ray powder camera[a]

Popout center	Mineral	Unreacted shale
5.58 b,m		
4.11 b,s	Cristobalite and opal	3.96 - 4.57 b,s
3.33 s	Quartz	3.32 s
2.53 b,m	Cristobalite and quartz	2.44 - 2.61 b,m

[a] b, broad band; s, strong reflection; m, moderate reflection.

The broad peaks at 4.11 Å and 2.53 Å reported in Table 3 are in agreement with the broad peaks reported by Franks and Swineford (14) for massive opal from the Kimball Member, Ogallala Formation, Scott County, Kansas. They concluded that hydrated low-cristobalite that is disordered by differing amounts of low-tridymite is an integral part of the opal structure.

Both the popout center and the unreacted shale particle handpicked from sand contained opal, cristobalite, and quartz with similar reflection intensities. It therefore seems reasonable that the shale particles in the sand are responsible for the deleterious popout reaction. The only peak that did not match was the one at 5.58 Å, which was in the zone of intense random X-ray scatter. The X-ray film was quite dark in this area on both films, and the scatter on the film for untreated shale could have masked the 5.58 Å reflection. An X-ray diffractogram presented later (Figure 7) indicates that the 5.58 Å peak could result from montmorillonite.

Geologic Origin

Attempts to delineate the area of concrete popout occurrence in Iowa were resisted by a natural reticence on the part of cement and concrete producers to advertise the problem, because of the possibility of repairs or replacements at their expense. Most of the occurrences were in northern and in central Iowa, in concrete utilizing Pleistocene outwash sands. The sands were derived from melting glacial ice, and ultimately derived from pulverization of bedrock by glacial scour.

Cristobalite, opaline silica and montmorillonite have been found in many clay sediments of geological young deposits (15, p. 436). With increasing sediment age the quartz content increases and the cristobalite content decreases by inversion to quartz. For this reason, it appears that the most likely bedrock source is Cretaceous shales, which comprise the uppermost bedrock in approximately the northwestern one-fourth of Iowa (16).

SHALE SPECIFIC GRAVITY AND ABSORPTION

Theory

Bulk specific gravity is defined in ASTM E12 as "The ratio of a weight in air of a given volume of a permeable material (including both permeable and impermeable voids normal to the material) at a stated temperature to the weight in air of an equal volume of distilled water at a stated temperature". The apparent specific gravity is defined as "The ratio of the weight in air of a given volume of the impermeable portion of a permeable material (that is, the solid matter including its impermeable pores or voids) at a stated temperature to the weight in air of an equal volume of distilled water at a stated temperature."

The total shale particle volume, V_t, is composed of the volume of solids, V_s, the volume of permeable voids, V_p, and the volume of impermeable voids, V_i. The definitions are expressed as equations in Table 4 along with equations derived from the definitions for the pycnometer and buoyancy tests.

Test Procedure

Three methods were used to determine the specific gravity of the shale. In the first method the pycnometer described in the Standard Method of Test for Specific Gravity of Soils (ASTM Designation, D854-58) was used. Hand-picked particles ranging in size from 1/16 inch to 1/8 inch in diameter were soaked in water 48 hours. The particles were

Table 4. Specific gravity equations[a]

Type of specific gravity	Definition equation	Pycnometer equation	Buoyancy equation
Bulk (oven-dry)	$\frac{W_o}{V_t \gamma_w}$	$\frac{W_o}{W_{ssd}-(W_a-W_b)}$	$\frac{W_o}{W_{ssd}-W_{iw}}$
Bulk (saturated-surface-dry)	$\frac{W_{ssd}}{V_t \gamma_w}$	$\frac{W_{ssd}}{W_{ssd}-(W_a-W_b)}$	$\frac{W_{ssd}}{W_{ssd}-W_{iw}}$
Apparent	$\frac{W_o}{(V_t-V_p)\gamma_w}$	$\frac{W_o}{W_o-(W_a-W_b)}$	$\frac{W_o}{W_o-W_{iw}}$

[a] W_o = weight in grams of oven-dry sample in air; V_t = total volume in cc of aggregate particle; γ_w = unit weight of water in gm/cc; V_p = volume in cc of permeable pores; W_{ssd} = weight in grams of saturated-surface-dry sample in air; W_a = weight in grams of pycnometer containing sample and filled with water; W_b = weight in grams of pycnometer filled with water; W_{iw} = weight in grams of saturated sample in water.

The percent absorption is defined in equation 4:

$$\frac{(W_{ssd}-W_o)\ 100}{W_o} \qquad (4)$$

then dried in absorbent towels until the surface sheen was absent and immediately weighed to determine the saturated-surface-dry weight. The shale particles were placed in the pycnometer, distilled water was added and the pycnometer was weighed. The shale particles were then oven-dried for 24 hours and weighed again. The weight of the pycnometer filled with only distilled water was also determined. From the above weights the following values were computed:

1. Percent absorption
2. Bulk specific gravity (oven-dry)
3. Bulk specific gravity (saturated-surface-dry)

4. Apparent specific gravity.

The buoyancy technique was the second method used to determine the specific gravity and the percent absorption. A single 3/4 inch shale particle was soaked in water for 48 hours after which it was surface dried and immediately weighed to determine the saturated-surface-dry weight. A string was then tied to the shale particle and the particle was submerged in water. The string was fastened to a balance and the weight of the shale submerged in water was determined. The string without the shale particle attached was submerged to the same distance as when the shale was attached and the string was weighed. The shale particle was oven-dried for 24 hours and weighed again. From the above weights the following values were computed:

1. Percent absorption
2. Bulk specific gravity (oven-dry)
3. Bulk specific gravity (saturated-surface-dry)
4. Apparent specific gravity.

The heavy liquid technique was the third method used to determine the specific gravity of shale. Solutions of tetrabromoethane and carbon tetrachloride were mixed in proportions such that oven-dried 1/16 inch to 1/8 inch shale particles were just held in suspension. The heavy liquid was strained and placed in a 25 ml volumetric flask. Weights of the empty flask and the heavy liquid filled flask provided the information necessary to determine the specific gravity of the liquid. Since the shale particles were just held in suspension by the heavy liquid, the specific gravity of the shale was the same as the specific gravity of the liquid.

Results and Analysis

The absorption calculated from equation 4 and the specific gravities determined in the heavy liquid test and calculated from the equations given in Table 4 are shown in Table 5.

Table 5. Shale specific gravity and absorption

Type of specific gravity	Method		
	Pycnometer	Buoyancy	Tetrabromoethane+ carbon tetrachloride
Bulk (oven-dry)	1.35	1.50	
Bulk (saturated-surface-dry)	1.81	1.88	
Apparent	2.50	2.42	
In heavy liquid			2.33
Absorption, %	34.3	25.1	

The percent absorption for the shale in Table 5 is over ten times the percent absorption for most Iowa river aggregates. This large percent absorption is responsible for the large variations in the specific gravities shown in Table 5 for any one test method. The percent absorption in the buoyancy method is lower than the percent absorption in the pycnometer method because of the large difference in particle size--only one 3/4 inch shale particle was used in the buoyancy method whereas many 1/16 inch to 1/8 inch shale particles were used in the pycnometer test. For a given internal shale structure the small particles should have a higher absorption than the large particle because the average surface-to-void distance is much less for the small particles, allowing water to saturate a higher percentage of voids in small particles than in a large particle.

The difference in percent absorption can be used to explain the difference in defined specific gravities for the different tests. Failure to obtain a high degree of saturation in the large shale caused the bulk specific gravity (oven-dry) to be higher for the buoyancy test than it was for the pycnometer test on the smaller shale particles. The apparent specific gravity for the buoyance test was lower than the apparent specific gravity for the pycnometer test because of the lower percent absorption for the buoyancy test.

The Method of Test for Lightweight Pieces in Aggregate (ASTM Designation: C123-64) requires flotation of a saturated-surface-dry aggregate on a heavy liquid with a specific gravity of 2.00. Since the shale had a saturated-surface-dry specific gravity of 1.88 as determined by the buoyancy test it should float, but if the lightweight particle test were conducted on an oven-dry specimen the shale would sink, since it can float only if the specific gravity of the liquid is higher than 2.33 as shown in Table 5. This is because the heavy liquid is absorbed into the shale.

Specifications for Concrete Aggregates (ASTM Designation: C33-64) require that the maximum percent by weight of total sample for lightweight particles be 0.5 where the surface appearance of concrete is of importance, and 1.0 in all other concrete.

Five Iowa sand samples were tested for lightweight particles by placing the sample in a heavy liquid with a specific gravity of 2.4. The results are shown in Table 6.

Table 6. Percentages of particles floating with a 2.4 specific gravity liquid

Sand sample	Percent, shale, coal and lignite
A	0.5
B	3.2
C	2.1
D	0.4
E	2.4

Sand samples B, C and E should be rejected because of excessive lightweight particles even though they may pass the Specification for Concrete Aggregates (ASTM Designation: C33-64) which requires the lightweight particle test to be made on a liquid with a specific gravity of 2.0. Although ASTM Designation C123-64 predicts the amount of deleterious coal and lignite, it fails to predict the amount of deleterious shale because the shale will not float on a heavy liquid with a specific gravity of 2.0.

CEMENT-SHALE REACTION KINETICS

X-ray Powder Measurements

The effects of time, temperature and relative humidity on the cement-shale reaction were determined by preparing, curing and running a semi-quantitative X-ray analysis on cured cement-shale pastes. Equal parts by weight of water, type I cement, and shale ground to pass the number 100 sieve were mixed to form a paste. The pastes were then subjected to different curing times, temperatures, and relative humidities as shown in Table 7.

Table 7. Cement-shale paste variables

Reaction time	Temperature °F	Relative humidity %
0,3,8,24,72 hours 7,14,28 days	75, 95, 115	75, 100

The required relative humidity was achieved by placing a saturated salt solution in the bottom of a small plastic jar. A relative humidity of about 75 percent was achieved by placing a saturated NaCl solution in the plastic jar. An excess of NaCl was added to insure the existence of the solid phase in the saturated solution. Selman (17) showed that the relative humidity of a saturated NaCl solution is dependent upon temperature and varies from 75.1 percent relative humidity at 75°F to 74.5 percent relative humidity at 115°F. The 100 percent relative humidity was obtained by placing distilled demineralized water in the bottom of the plastic jars.

The cement-shale pastes were placed on a plastic perch in the controlled humidity jars so that the water or saturated salt solutions were not in contact with the paste. Greased vacuum lids were fastened securely to the jars and the jars were then placed in ovens set at the various temperatures shown in Table 7. Lids were loosened and re-tightened after 3 and 8 hours in the constant temperature ovens to allow pressure equilibration between the inside of the jars and atmospheric pressure.

Specimens were removed from the oven at the reaction times given in Table 7 and were immediately placed in a vacuum desiccator until such time as they could be X-rayed. Sufficient sample was available for the powder diffractometer to be used for this phase of the project. A copper tube and nickel filter were used. The beam slit was 3°; medium resolution Soller slit and 0.2° detector slit were used. A line focus with a 4° target-beam angle was used. The scanning rate was 2° per minute and the chart speed 1 inch per minute.

The specimen was compacted into a brass ring under 1,000 psi by a method developed by Handy (18). The brass ring was mounted on the diffractometer and an X-ray pattern was obtained. Peak counts were obtained by setting the diffractometer at a 2θ angle of 21.8° and summing radiation counts on diffraction peaks over a 100 second interval with automatic print-out occurring every 10 seconds. The peak counts were corrected for background by making five 10 second counts on each side of the peak at 2θ angles of 19.0° and 24.0°. This method of peak height determination was used with the specimen in both the stationary and the spinning mode. The specimen was spun by a motorized friction drive bearing against the periphery of the brass ring sample mount. From such peak counts the effects of curing time, temperature, and relative humidity upon the cement-shale reaction products could be determined.

Results and Analysis

The X-ray powder diffractograms for 100 percent shale, 50 percent shale--50 percent cement unreacted, and 50 percent shale--50 percent cement reacted for 28 days at 115°F and 100 percent relative humidity are shown in Figure 7. The major component of the shale is opal containing cristobalite, 4.07 Å, and possibly some tridymite, 4.27 Å, which could be masked by the 4.26 Å quartz peak. The shale also contains quartz, 3.34 Å, and montmorillonite, 16.9 Å.

Tricalcium silicate, C_3S, is the major component of unhydrated portland cement and is the only component giving significant peaks in Figure 7. Dicalcium silicate, C_2S, is the second major component of unreacted portland cement. Several C_2S and C_3S peaks are either coincidental or nearly so. Therefore the C_2S peaks are not indicated in Figure 7.

As can be seen in Figure 7 for cement and shale cured at 100 percent relative humidity for 28 days, the opal-cristobalite peak has

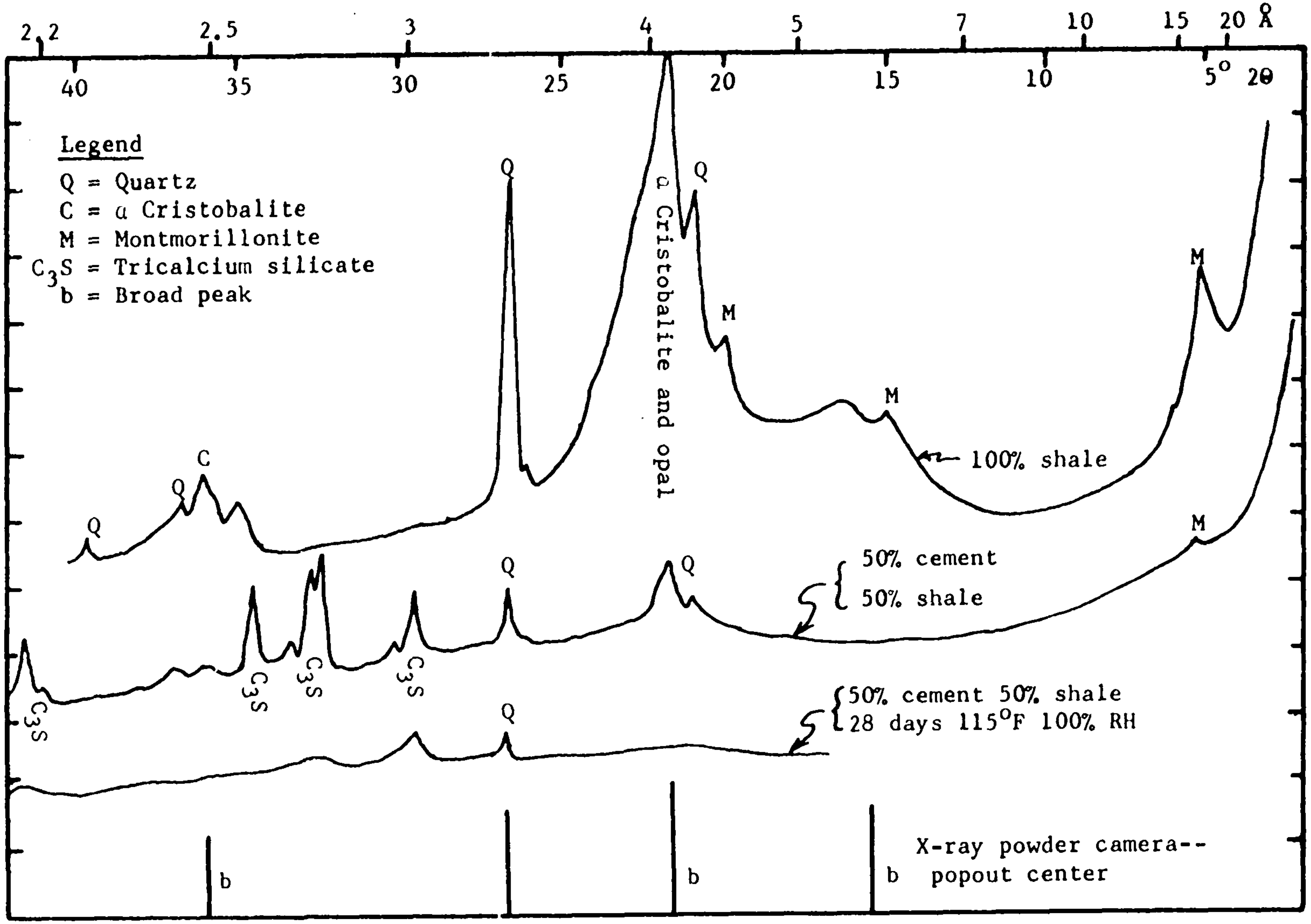

Figure 7. X-ray diffractograms of reactive shale

practically vanished and the reaction products are non-crystalline. Based upon the information presented in the literature review it is probable that when cement, shale and water react, the opal and cristobalite in the shale are attacked by the alkalis in the cement to form a calcium-alkali-silica complex. When all of the alkali has reacted, the $Ca(OH)_2$ produced when cement hydrates also can react with pulverized opal and cristobalite to form calcium-silica-hydrate gel which also is not well crystallized.

The Debye-Scherrer camera powder measurements on a popout center are shown for comparison with the shale X-ray diffractogram. The height of each line is drawn relative to the estimated diffraction intensity, and broad lines are indicated by the letter "b" in Figure 7.

The reaction rates for the opal-cristobalite component of the shale reacting with cement paste at various temperatures and relative humidities are shown in Table 8, the percentages remaining being calculated from X-ray peak-height counts at 21.8° 2 θ and representing the average values for the specimen in the stationary and spinning mode. The counts for the zero time or non-reacted specimens were used to calculate the percent of opal and cristobalite remaining. This method is semi-quantitative and the fact that the specimen cured at 115°F and 100 percent relative humidity for 3 hours had a calculated percent remaining of 106 indicated that the results are only approximate.

The data given in Table 8 are presented graphically in Figure 8 for specimens cured at 100 percent relative humidity and in Figure 9 for specimens cured at 75 percent relative humidity. At 100 percent

Table 8. Percent opal and cristobalite remaining after reacting with cement paste

Relative humidity %	Temp. °F	Curing time						
		3 hr.	8 hr.	24 hr.	3 days	7 days	14 days	28 days
100	75	98	87	89	76	76	56	48
100	95	97	97	81	66	55	27	22
100	115	106	73	65	34	14	11	11
75	75	100	95	90	89	83	75	71
75	95	99	88	75	61	46	35	33
75	115	100	99	73	61	56	52	52

relative humidity the opal and cristobalite reacts with the cement at greater rates as temperature increases. At 75 percent relative humidity the opal and cristobalite reaction rate also increases with temperature except for the 115°F specimen; up to one day curing time the 95°F and 115°F specimens have about the same reaction rate. Since the specimens are initially mixed with sufficient water to form a paste, the relative humidity inside the specimen would start out at 100 percent at zero curing time and decrease to 75 percent at some future time. The specimens were not instrumented to determine the micro-climate inside them. It can be assumed that the higher the temperature the more rapidly the micro-climate approached the climate surrounding the specimen. A relative humidity of 75 percent in the 115°F specimen was certainly reached at an earlier time than it was in the 95°F specimen. This slowed down the reaction rate in the 115°F specimen since the opal and cristobalite reaction rate decreases as the relative humidity decreases.

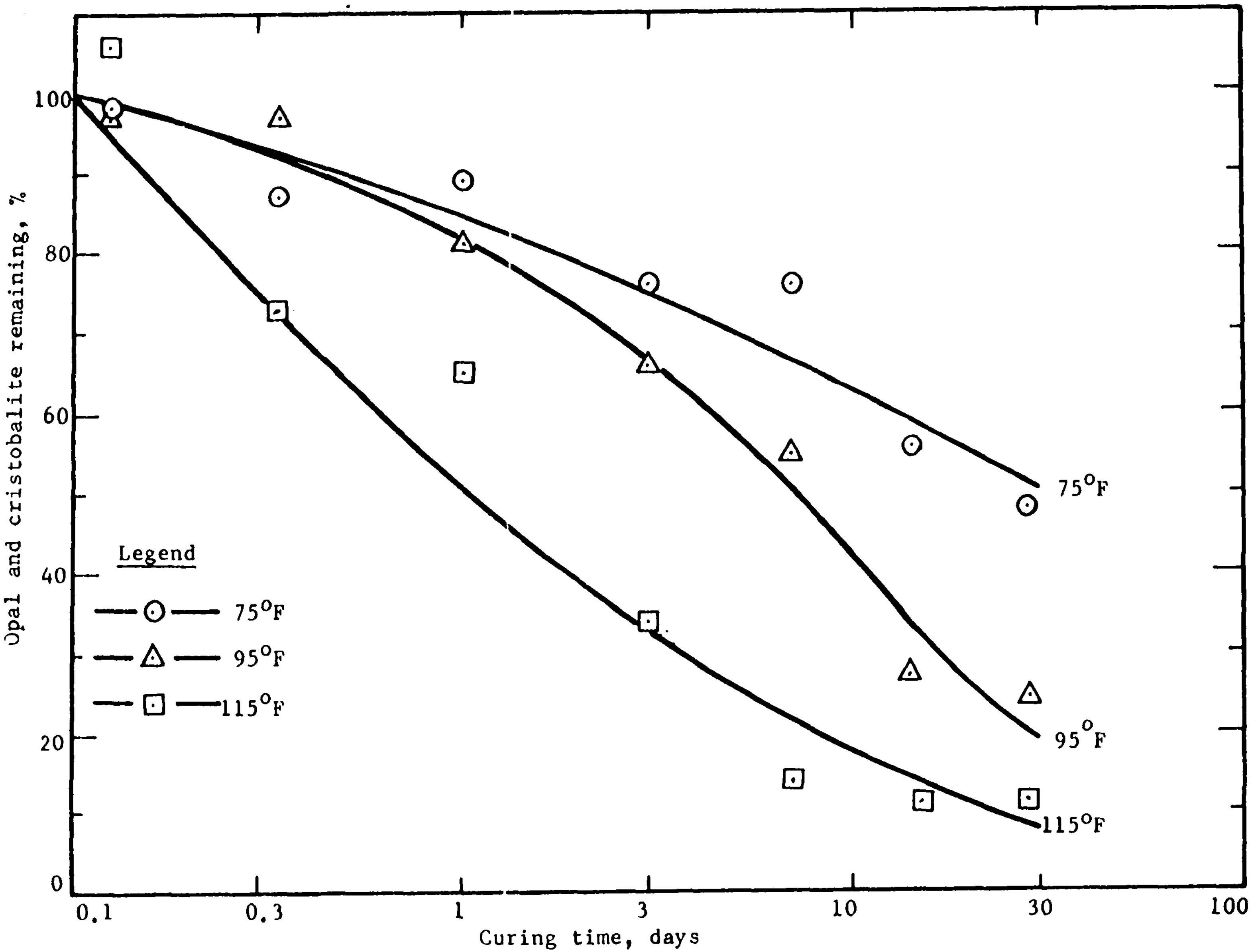

Figure 8. Opal and cristobalite depletion--50% cement, 50% shale, 100% relative humidity

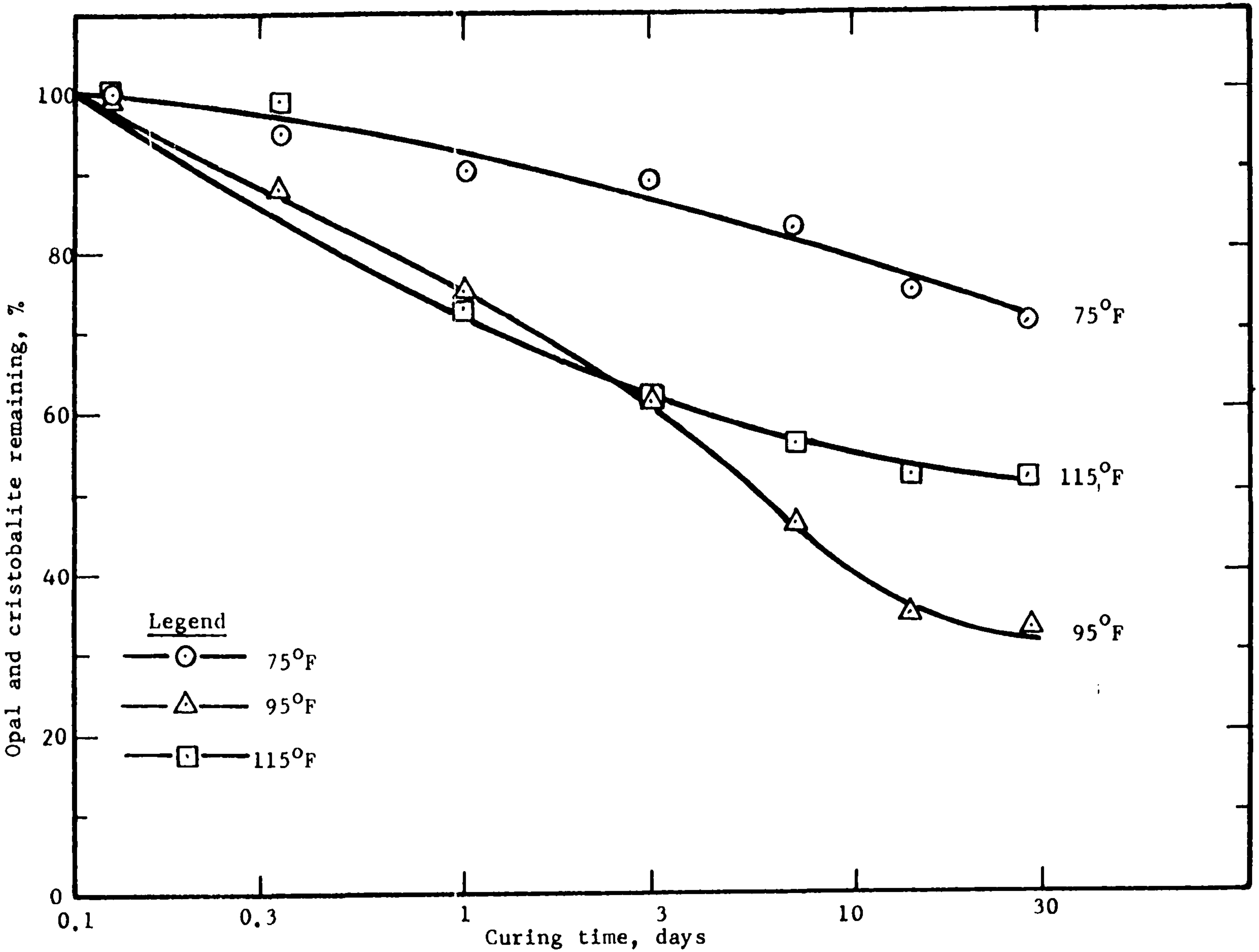

Figure 9. Opal and cristobalite depletion--50% cement, 50% shale, 75% relative humidity

The kinetics of the chemical reactions involved in the conversion of reactive silica to a calcium-alkali-silica complex cannot be specifically determined because of the multiplicity of the reacting components present. Information about the rate with which reactive silica is used up can be obtained by making some simplifying assumptions and applying the first-order rate equation (9b)

$$\frac{dx}{dt} = K\,(a-x) \qquad (5)$$

where K is the rate constant. It is assumed that the initial concentration, "a", of the reactive silica is 100 percent and that x is the percent of reactive silica changed from opal and cristobalite to a calcium-alkali-silica complex at time t as determined by the X-ray peak-height count method. Also $\frac{dx}{dt}$ is the rate of formation of the calcium-alkali-silica complex. Since $x = 0$ at $t = 0$ equation 5 can be integrated to give

$$\ln \frac{a}{a-x} = K\,t \qquad (6)$$

If $\ln \frac{a}{a-x}$ is plotted versus time t, the first order rate constant, K, can be determined and is the slope of the line. The first-order equation values for $\ln \frac{a}{a-x}$ for use in such a plot are given in Table 9. These values are plotted in Figure 10 for the 100 percent relative humidity specimens and Figure 11 for the 75 percent humidity specimens. The points at 0.125 days are not plotted because of congestion in this area of the graph, but were used in the regression analysis which was made for each relative humidity and temperature combination. Only points to the left of the stepped line shown in Table 9 were used

Table 9. First-order rate equation values for opal-cristobalite depletion

Relative humidity %	Temp. °F	$\ln\frac{a}{a-x}$ for a curing time in days of						
		0.125	0.333	1	3	7	14	28
100	75	0.015	0.135	0.111	0.278	0.270	0.576	0.732
100	95	0.035	0.031	0.208	0.408	0.598	1.306	1.496
100	115	0.070	0.312	0.431	1.070	1.973	2.254	2.163
75	75	-0.003	0.047	0.104	0.119	0.191	0.285	0.341
75	95	0.009	0.132	0.282	0.489	0.772	1.050	1.108
75	115	0.000	0.012	0.313	0.501	0.573	0.654	0.654

in the regression analysis. Also the value $\ln\frac{a}{a-x}$ equals zero at time equal zero was used in the regression analysis even though it is not shown in Table 9. Values to the right of the stepped line in Table 9 were not used because of the obvious deviation from the first-order rate equation at the longer times and higher temperatures.

The first-order rate constant, K, for the linear regression lines shown in Figures 10 and 11 along with the correlation coefficient, r, and the intercept, b, are given in Table 10.

Table 10. First-order rate constants for opal-cristobalite depletion

Relative humidity,%	Temp. °F	Rate constant K, days^{-1}	Correlation coefficient,r	Intercept b	Applicability limits, days
100	75	0.0364	0.95	0.0656	0-14
100	95	0.0895	0.99	0.0423	0-14
100	115	0.2806	0.98	0.0835	0-7
75	75	0.0191	0.95	0.0368	0-14
75	95	0.1069	0.96	0.0765	0-7
75	115	0.1761	0.95	0.0082	0-3

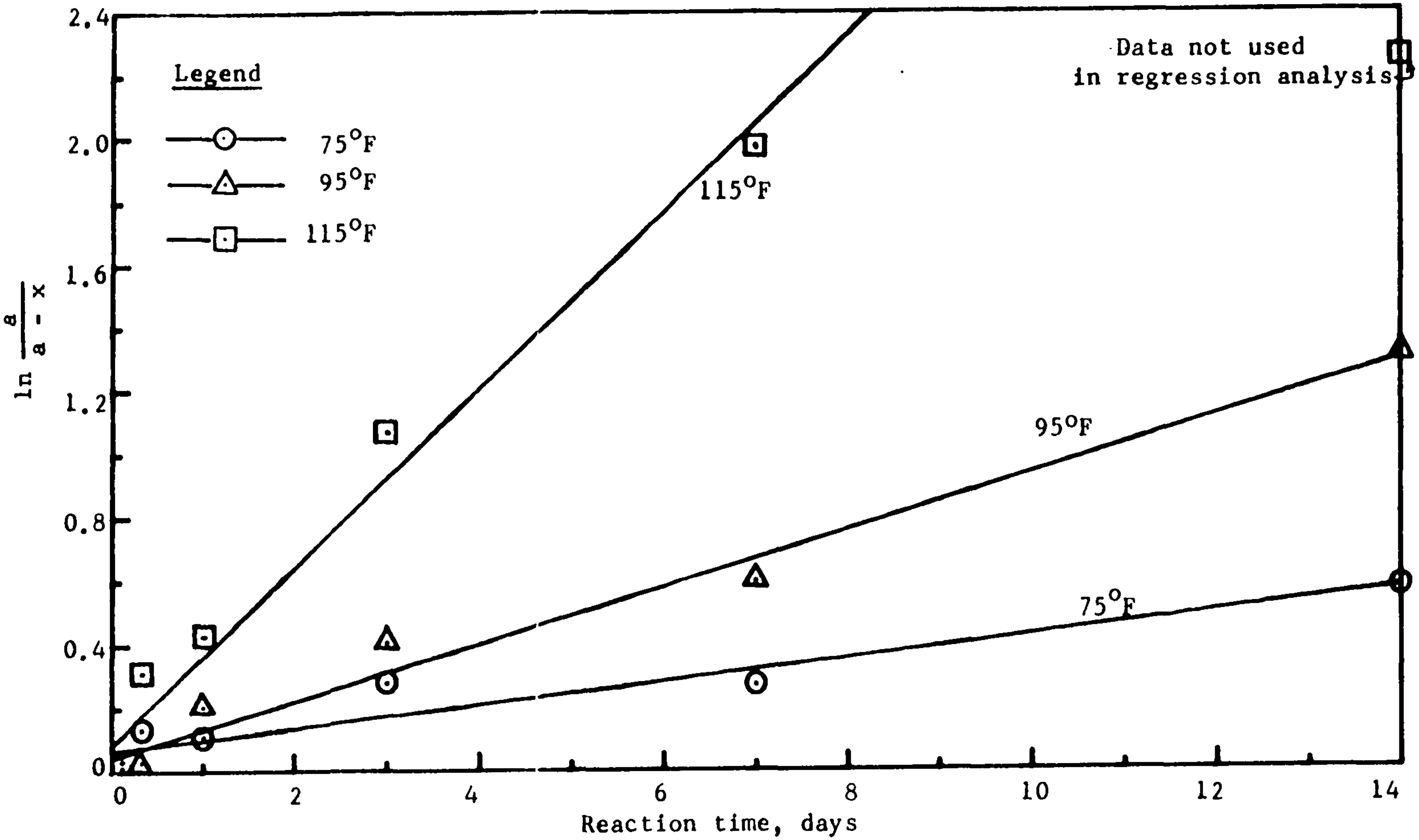

Figure 10. Rate of opal-cristobalite depletion, 100% relative humidity

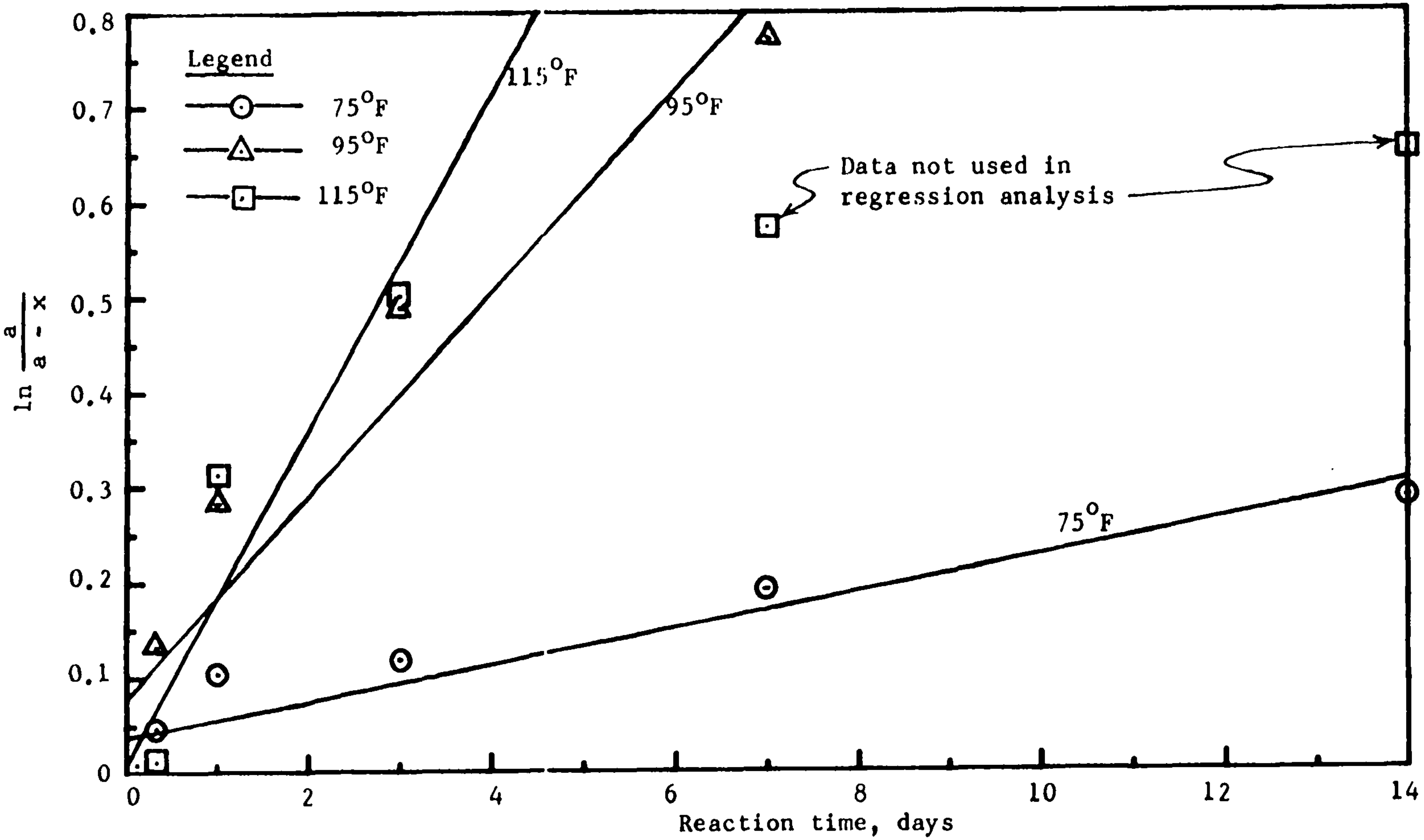

Figure 11. Rate of opal-cristobalite depletion, 75% relative humidity

Considering that the X-ray peak-height count method of tracing the rate of reactive silica depletion is semi-quantitative, the correlation coefficients of 0.95+ shown in Table 10 indicate that the reaction is a first-order one at least for the earlier reaction times. The rate constants, K, shown in Table 10 can then be used in Equation 6 to determine the percent of reactive silica, x, that has been changed to calcium-alkali-silica complex at a given time, temperature and relative humidity.

CONCRETE POPOUT TEST SLABS

Test Procedure

Three series of 2 ft by 2 ft by 3 3/4 inch concrete slabs were made and tested. Each series contained 12 slabs. The concrete mix proportions by weight were 1.00 part type I portland cement described in Table 1, 2.47 parts river sand, and 2.81 parts river gravel with a water-cement ratio of 0.50 for all slabs in each series.

An alkali solution containing 1 mole of NaOH and 1.3 moles of KOH diluted to one liter was used in batches requiring alkali contents higher than the 0.56 percent in the cement. One ml of the 2.3 normal alkali solution contains 0.040 gm NaOH and 0.0723 gm KOH. Since 1 gm NaOH is equivalent to 0.775 gm Na_2O and 1 gm KOH is equivalent to 0.84 gm K_2O, one ml of the 2.3 normal alkali solution would contain an equivalent of 0.031 gm Na_2O and 0.0608 gm K_2O. On an equivalent total alkali basis one gm of K_2O is equivalent to 0.66 gm Na_2O, giving for one ml an equivalent of 0.031 gm Na_2O + 0.0401 gm Na_2O or 0.0711 gm Na_2O.

A batch containing 22.5 lb of cement with an initial alkali content of 0.56 percent would require an additional 0.44 percent alkali to bring the total alkali up to 1.0 percent. Therefore an amount of alkali solution equal to $0.44\ (22.5\ \text{lb})\ \left(\frac{454\ \text{gm}}{\text{lb}}\right)\left(\frac{\text{ml } 2.3\ \text{N alkali solution}}{0.0711\ \text{gm } Na_2O}\right)$ or 632 ml was included in the mix water for all batches requiring a total alkali content expressed as Na_2O of 1.0 percent. In those batches requiring a total alkali content of 1.5 percent, 1350 ml of 2.3 N alkali solution was included in the mix water.

The sand contained 0.77 percent shale. Crushed shale passing the number ten sieve but retained on the number 20 sieve was used in those slabs requiring a shale content above 0.77 percent.

Fly ash from Kansas City, Missouri, colored toppings, type of finish and curing conditions were other variables investigated. Tables 11 and 12 indicate the conditions tested for Series 1 and 3. Series 2 was identical to Series 1 except for curing conditions. Therefore, a table is not included for Series 2.

Table 11. Test slabs - Series 1

Slab no.	Shale, % by wt. sand	Alkali, % by wt. cement	Fly ash, % by wt. cement	Popout density popouts/100 sq.in.
1	0.77	0.56		0
2	0.77	1.0		50
3	0.77	1.5		120
4	1.54	0.56		0
5	1.54	1.0		25
6	1.54	1.5		70
7	2.31	0.56		0
8	2.31	1.0		25
9	2.31	1.5		65
10	2.31	0.56	25	5
11	2.31	1.0	25	35
12	2.31	1.5	25	15

The slabs in Series 1 were cast and struck off immediately. About 1/2 hour after casting, each slab was again struck off and was then wood floated and edged. At about three and five hours after casting, each slab was steel troweled as shown in Figure 12. Twenty-four hours after casting, the slabs were removed from the forms and placed in the constant temperature and humidity chamber shown in Figure 13. The sloping roof of the chamber was constructed with one by fours with a polyethelene cover on top and bottom. A temperature of 115°F and a relative humidity of 95+ percent was maintained by thermostatically controlled radiators and ejection of low pressure steam into the chamber. The sloping roof structure prevented the dripping of condensate on slabs. A fan was used to assure an even distribution of air temperature and humidity. After 7 days in the curing chamber the slabs were photographed and the popout density was determined.

Series 2 was identical to Series 1 except for curing conditions. Twenty-four hours after placement, the Series 2 slabs were removed from the forms and submerged in water for 7 days. The water temperature was maintained at 70 ± 2°F and the air temperature was 75 ± 3°F. The curing water was sampled several times during the 7 days the concrete slabs were submerged. The alkali concentration of the water was determined by flame photometry. The ratio of concrete volume to curing water volume was 1.36. After 7 days flood-curing the slabs were placed in the constant temperature (115°F) and relative humidity (95 + percent) for 7 more days. The slabs were then photographed and the popout density was determined.

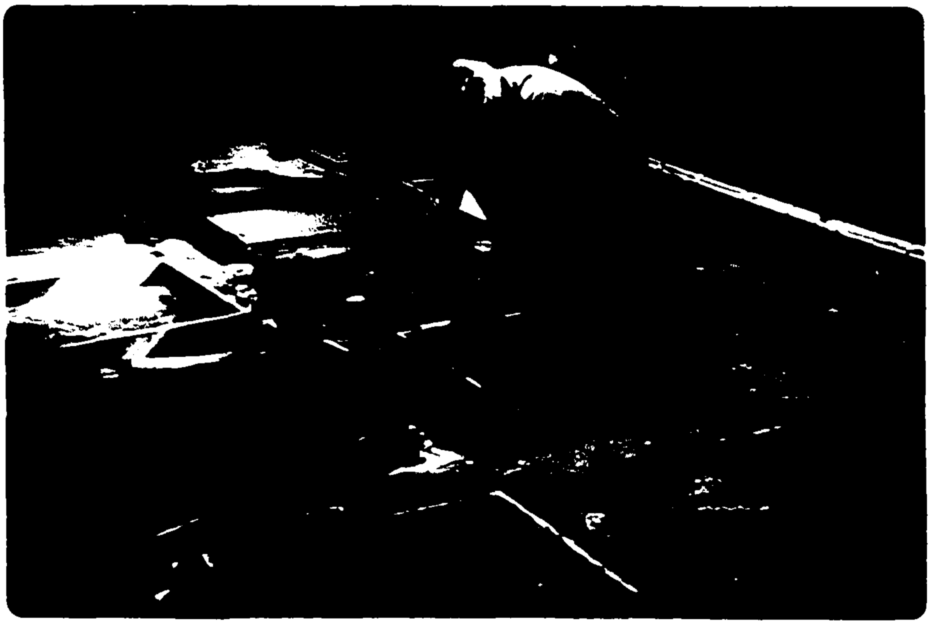

Figure 12. Concrete test slabs

Figure 13. Constant temperature-humidity chamber

Table 12. Test slabs - Series 3

Slab no.	Alkali, % by wt. of cement	Shale dust[a] %	Fly ash[a] %	Colored topping shake	Finish	Popout density popouts/100 sq.in.
1	1.0	0	0	none	troweled	35
2	1.0	0	0	none	broomed	0
3	1.0	0	0	none	broomed	0
4	1.0	0	0	red	troweled	15
5	1.0	0	0	green	troweled	50
6	1.0	0	15	red	troweled	5
7	1.0	0	15	green	troweled	5
8	1.0	15	0	red	troweled	0
9	1.0	15	0	green	troweled	0
10	0.56	0	0	none	troweled	5
11	1.0	0	0	none	troweled	85
12	1.5	0	0	none	troweled	110

[a] Percentage by weight of shake added to the colored topping shake only.

All slabs in Series 3 contained 1.54 percent shale, and all except 10, 11, 12 contained 1.0 percent alkali. Slabs 10, 11, and 12 were also the only ones containing air-entrainment, having respectively 5.9, 6.2, and 6.6 percent air entrained. Slabs 1, 10, 11 and 12 were steel troweled twice as were the slabs in Series 1. Slabs 2 and 3 were given a broomed finish after being troweled once.

Slabs 5 through 10 in Series 3 had two pounds of a colored topping shake spread over each slab in two applications. The first application of 1.33 pounds of the shake was spread on the slabs shortly after the first troweling. As soon as water was absorbed into the shake, it was troweled. Then the final 0.67 pounds of shake was spread on the slab and troweled in as soon as it was moistened by absorption from the slab. Fly ash in the amount of 15 percent by weight of the shake was added to the shake placed on slabs 6 and 7. Shale dust passing the number 20 sieve was added to the shake placed on slabs 8 and 9 in the amount of 15 percent by weight of the shake. All slabs were cured in the same manner as those of Series 1.

Results and Analysis

Photographs of the 12 Series 1 slabs are shown in Figure 14. The popout density given in Table 11, increases as the alkali content of the cement increases, whereas an increase in shale content did not increase the popout density. In fact, as shown in Figure 15, for a given alkali content, the higher the shale content the fewer the popouts. The higher reactive surface area present in slabs containing higher percentages of shale could distribute the reaction sites sufficiently to cause fewer disruptive sites.

It was expected that fly ash would use up the alkalis and prevent popouts from occurring by providing sufficient distributed small nondestructive reaction sites in the concrete. Although the popout density was significantly reduced for the slab containing flyash, plus 2.31 percent shale and 1.5 percent alkali, it was not reduced for the slab containing flyash, plus

Figure 14. Experimental concrete slabs

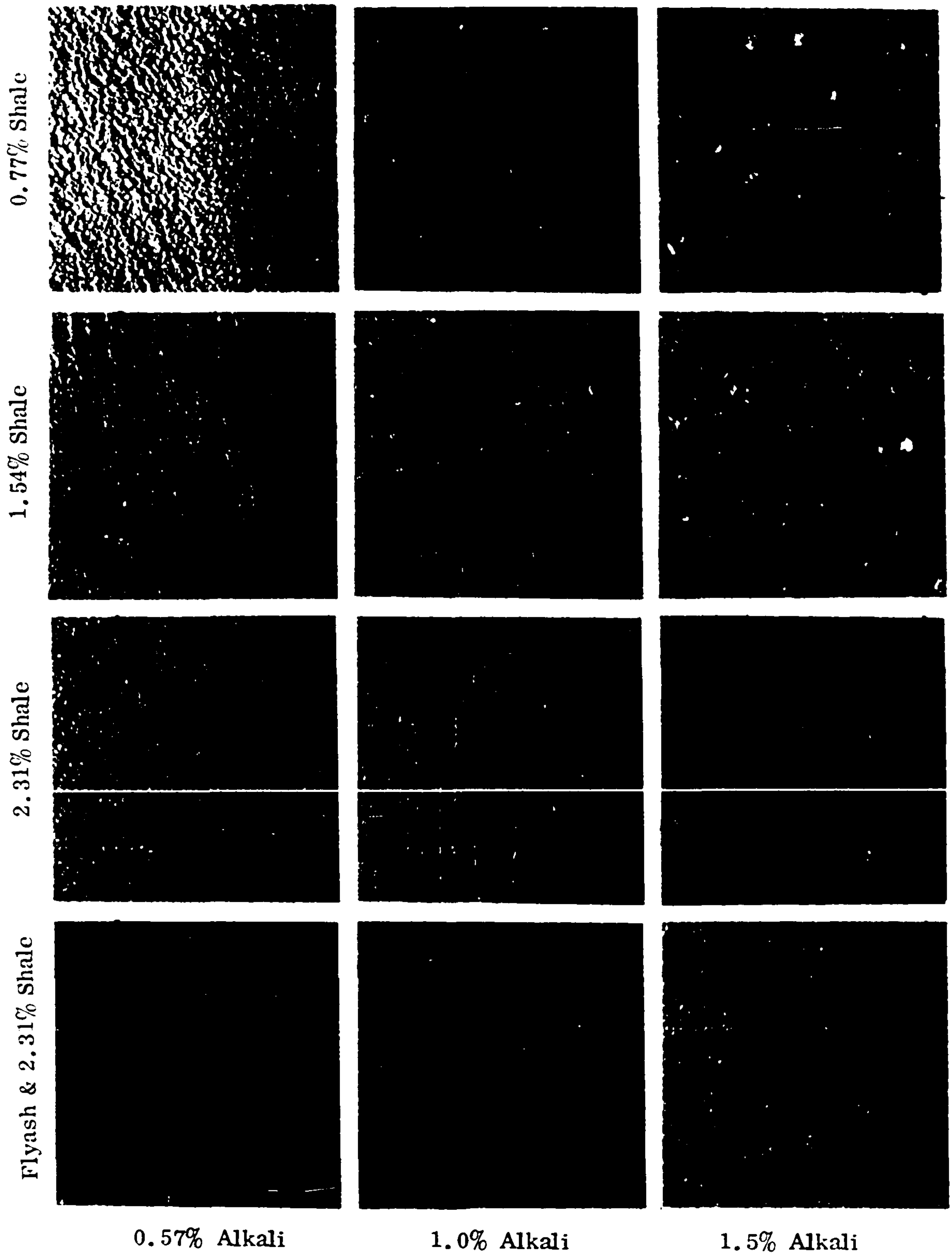
0.77% Shale
1.54% Shale
2.31% Shale
Flyash & 2.31% Shale
0.57% Alkali
1.0% Alkali
1.5% Alkali

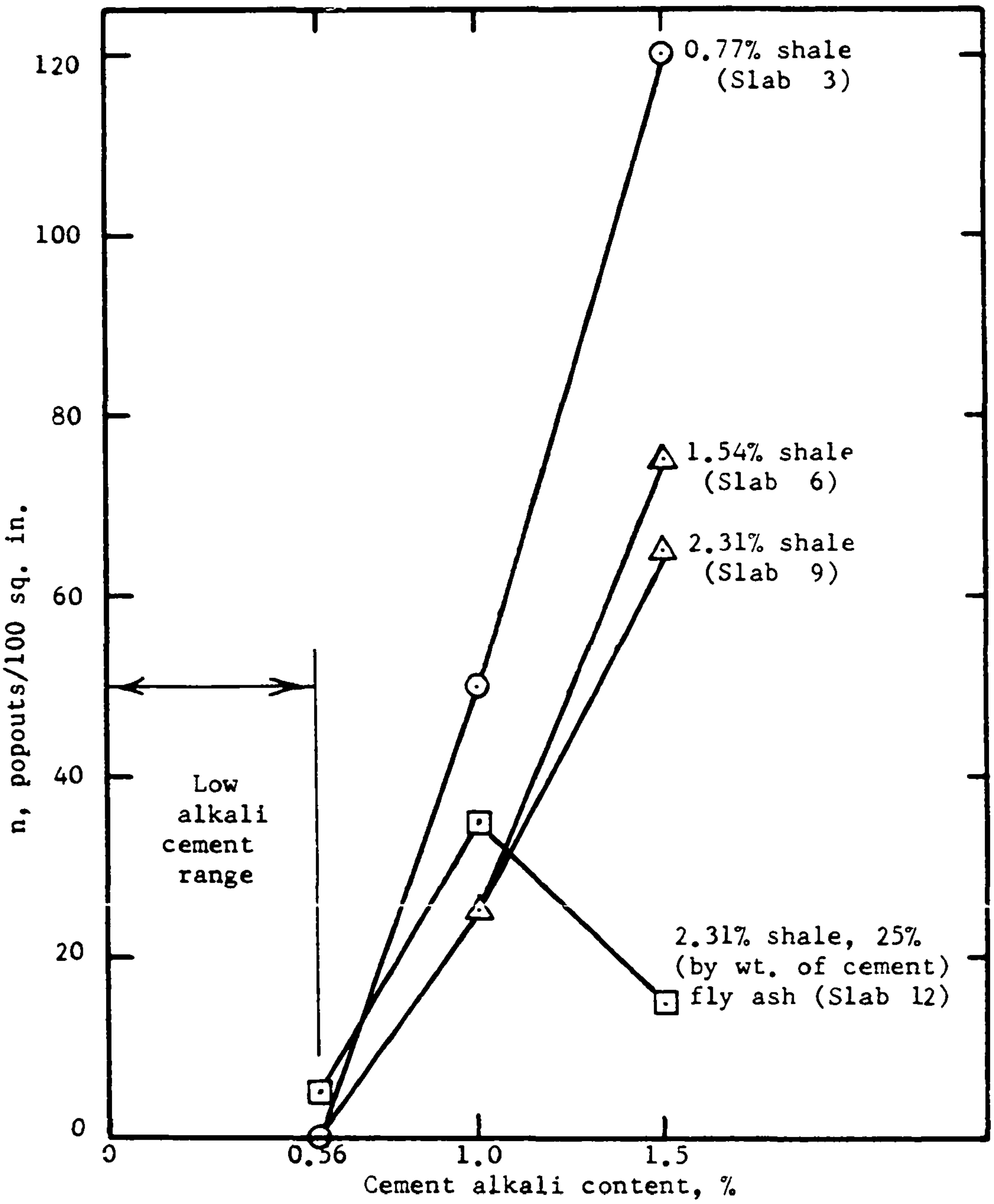

Figure 15. Popout density for various shale and alkali contents

2.31 percent shale and 1.0 percent alkali. The high porosity of the shale coupled with the high reactivity of opal in the shale could result in the alkali reaction with the shale being more rapid than the reaction with the fly ash.

The high relative humidity kept some of the reaction products fluid enough to allow them to penetrate the matrix surrounding a reacting shale particle without causing a popout to occur. These reaction products can be seen as dark spots in the photographs of Figure 14. Many of these dark reaction products are visible at the surface for all slabs containing 1.0 and 1.5 percent alkali even though a popout was not associated with the reaction. The occurrence density of the dark reaction products increases as the alkali content and the shale content increases.

The flood curing of Series 2 slabs 12 to 24 hours after casting prevented popouts from occurring in any of the slabs. Everything connected with Series 2 slabs was identical to Series 1 slabs except for the 7 days flood curing of Series 2 slabs prior to placing them in the constant temperature and humidity room.

The Na_2O and K_2O concentrations in the curing water are given in Table 13 and Figure 16 for the 7 day curing period.

Table 13. Concentration of alkalis in curing water

Sampling time	Alkali concentration, ppm	
	K_2O	Na_2O
0 hr (tap water)	40	0
2 hr	156	56
2 days	264	120
4 days	283	118
5 days	274	124
6 days	299	129
7 days	290	139

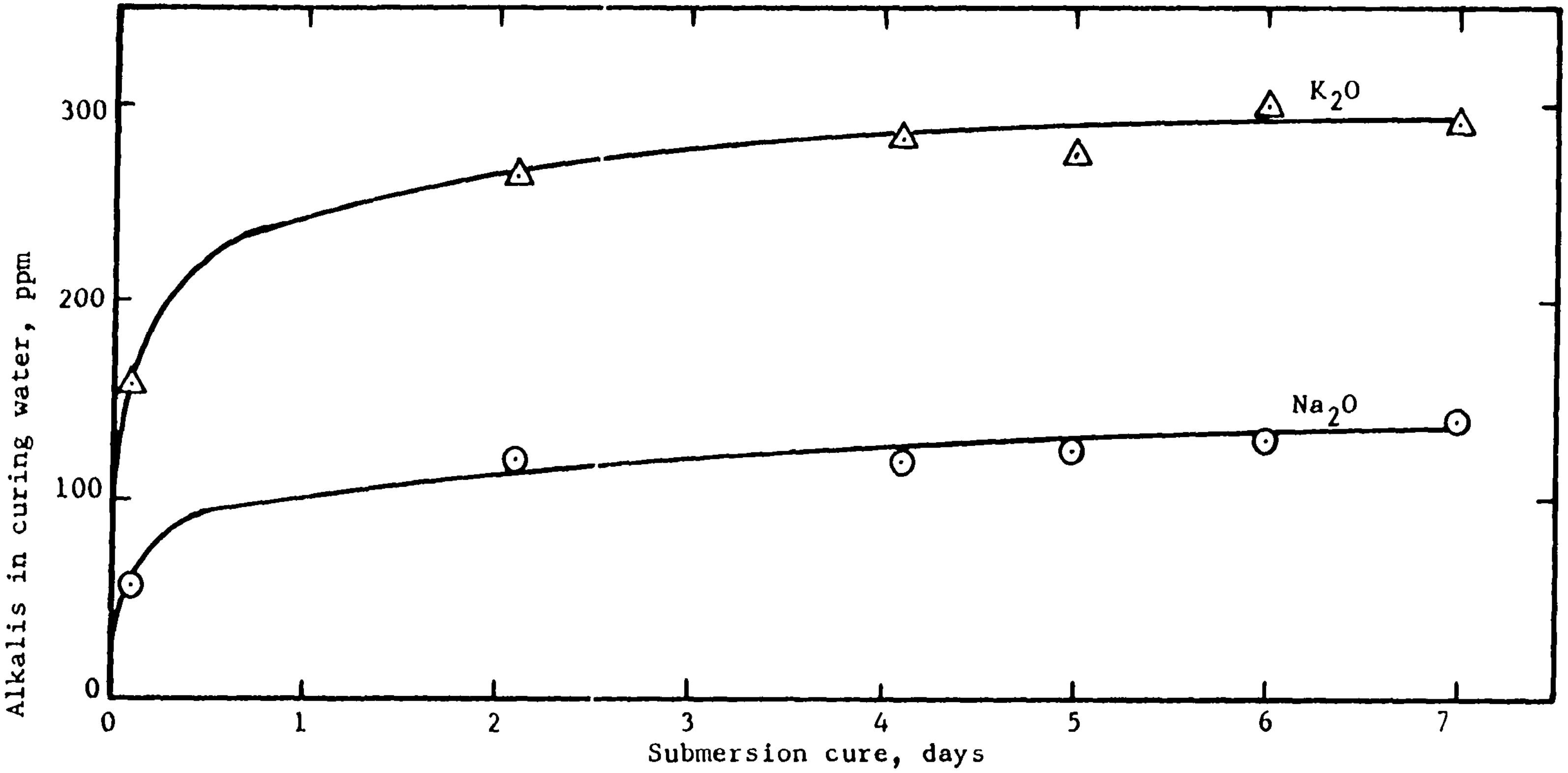

Figure 16. Alkalis leached into submersion curing water

The alkalis leached into the curing water became constant at about 2 days curing time as shown in Figure 16. Therefore it is probably not necessary to flood cure for periods in excess of 2 days. The flood water should be flushed off the concrete to prevent the redeposition of alkalis on the concrete surface during evaporation of the curing water. As can be seen in Figure 16 the flood water removed alkalis as they came to the surface of the concrete. This leaching was sufficient to reduce the concentration of alkalis remaining in the concrete slabs to a level low enough that any alkali aggregate reaction that did occur was not enough to produce popouts.

The popout density of Series 3 slabs is given in Table 12. The broomed finish given to slabs 2 and 3 prevented popouts from occurring, the broomed finish apparently leaving the surface sufficiently open that any reaction products developing just under the surface can escape without causing disruption.

Slabs 4 and 5 had about the same density of popouts as the corresponding slab 1 of Series 3 and slab 5 of Series 1 even though a colored topping was placed over the concrete. However, the popouts in the colored slabs were much larger than those in the uncolored slabs, the larger popouts being due to the reactive shale particles having a deeper embedment in the colored topping slabs than in the uncolored slabs because of the method of color application.

When 15 percent fly ash by weight of colored topping was added to the topping, the popout density was decreased. When 15 percent shale dust passing the number 20 sieve was added to the topping material, the popouts were eliminated. In both cases the alkalis react with the fly ash or powdered shale dust in preference to the larger popout-inducing shale particles.

Initially it was postulated that entrained air voids would provide pressure relief reservoirs for the expanding alkali silica gel and thereby decrease the number of popouts. However, the air entrainment added to slabs 10, 11 and 12 did not decrease the popouts compared to slabs 4, 5 and 6 of Series 1. In fact there was an increase in popout density in the air-entrained slabs. One possibility is that air-entrainment tends to make the surface easier to finish, resulting in a surface that is sealed to a greater extent than non-air-entrained concrete. The smoother and more completely sealed the surface, the more likely popouts will occur, since reaction products can't be released through surface voids and irregularities.

CONCLUSIONS

Alkali in cement reacts with opal and cristobalite in Iowa shale to produce a swelling alkali-silica gel. The expanding gel causes an inverted cone-shaped fracture known as a concrete popout. The case histories studied indicate that popouts occur most frequently on smooth-finished concrete slabs in contact with the ground.

The shale in Iowa river sand was just held in suspension by a tetrabromoethane-carbon tetrachloride solution with a specific gravity of 2.33. The shale content can not, therefore, be determined in The Method of Test for Lightweight Pieces in Aggregate (ASTM Designation: C123-64) since the heavy liquid used has a specific gravity of 2.00. When checked on a 2.4 specific gravity heavy liquid, three of the five sand sources examined had shale, coal and lignite in excess of the 1.0 percent allowed by ASTM Designation: C123-64.

Several of the Type I cements tested had alkali contents in excess of the 0.60 percent allowed by ASTM Designation: C33-64 when deleteriously reactive materials are present in fine aggregate.

For the first three days the alkali-silica reaction is first-order with the rate constant, K, dependent upon the temperature and relative humidity.

An increase in alkali content of cement increases the occurrence of popouts in concrete containing the reactive shale.

Sand containing 0.77 percent shale caused a higher popout density than sand with higher shale contents.

Concrete popout occurrence may be minimized by:

1. Flood curing within 12 to 24 hours after placement and continued for at least 2 days. Attempts to flood at later ages will cause popouts rather than prevent them.

2. Using low-alkali cement.

3. Eliminating the reactive shale from the aggregate by use of heavy medium separation or by using shale-free aggregate.

4. Placing a broomed finish on the concrete.

5. Adding fly-ash or shale dust in the amount of 25 percent by weight of cement to the fresh concrete.

Concrete popouts may be postponed by:

1. Keeping the temperature below 75°F and the relative humidity below 75 percent.

2. Avoiding the use of moisture barriers such as paint, curing compounds or tile where on-grade concrete has a popout potential.

Flood curing was very effective in reducing concrete popouts and would probably be the most economical procedure, applicable to on-grade concrete where the popout problem is most severe. Postponement of popouts is not a cure, since the chemical reaction can remain latent for years.

PART II. REACTION MECHANICS

INTRODUCTION

Popout pressures are predicted by analyzing the nature of the stresses on several assumed failure surfaces. Dimensional analysis was used to reduce the number of variables required for the experimental portion of the program. The theory of elasticity was used to obtain an idea about the stress magnitudes in the vicinity of a reactive aggregate particle. The problem of a shale aggregate just below the concrete surface reacting with alkali in cement is analogous to a pressurized spherical cavity in a half-space. The elastic stresses in the vicinity of such a cavity have been solved by Mitchell and Weese (19). Even though the stresses surrounding a reactive aggregate are not in the elastic range at the time of fracture, the elastic equations do provide an insight into the magnitude of the stresses prior to fracture.

Prevention of concrete popouts would seem to be much more important than prediction of the pressures required to cause a popout to occur. Popout pressure equations could, however, have application in circumstances far removed from the field of concrete, for example, to determine the force a seedling must exert on overlying soil in order to emerge, or the allowable force on an anchor bolt in concrete, rock or other material could be determined by an appropriate pressure prediction equation.

Theoretical popout pressure prediction equations are developed for three different models. The theoretical equations are checked by measuring the pressure required to mechanically induce popouts in hardened portland cement and plaster of Paris.

LITERATURE REVIEW AND THEORY

A search of the literature failed to provide information regarding the mechanics involved in concrete popouts. Some information was, however, found on the breakout resistance of objects embedded in soils. This information is perhaps germane to the study of concrete popouts.

Balla (20) conducted pull-out tests on a model mushroom foundation embedded in sand. He determined the failure surface to be the one generated when the arc of a circle is rotated around a vertical axis through the center of the foundation. The circle meets the edge of the foundation at 90° from the horizontal and meets the soil surface at $45 - \phi/2$ from the horizontal where the angle ϕ is the friction angle for the sand.

Vesic (21) applied to objects embedded in the ocean bottom a pull-out equation derived by assuming the soil to be a rigid-plastic solid. The agreement between theoretical and experimental break-out factors did not generally agree, and for dense sands and stiff clays differed by as much as a factor of 2.

The work done on anchor pull-out studies in soils is not directly related to the concrete popout problem because the pressure involved at the soil-anchor interface is uniaxial whereas the pressures developed at the swelling aggregate-mortar interface are triaxial. Also concrete often fails by brittle tensile fracture whereas soil usually fails by shear.

The problem of the stresses induced into an elastic media by a pressurized spherical cavity in a half-space has been solved by Mitchell and Weese (19). They found that the tangential tensile stress at the top of the cavity-matrix interface was about 1.14 times the compressive stress in the cavity.

Timoshenko and Goodier (22) present Lame's solution to the stresses in an elastic spherical thick-walled pressure vessel. If the outside radius goes to infinity the case of a pressurized spherical cavity in an elastic full space is obtained and the tensile stress tangent to the inclusion-matrix interface will be ½ of the pressure in the spherical cavity. In a spherical pressure vessel with a finite outside diameter the tangential tensile stress at the inner surface would always be greater than ½ of the internal pressure.

Malhotra and Zoldners (23) indicate that the tensile strength for portland cement concrete is usually in the range of 1/7 to 1/13 of the compressive strength. Since the tangential tensile stress at the cavity-matrix interface in a half space is about equal to the cavity pressure, and since the lowest possible value the tangential tensile stress can have at a cavity-matrix interface in full space is ½ of the cavity pressure, it seems logical to assume that the concrete matrix next to an expansive aggregate would fail in tension rather than shear. Since the theory for anchor pull-out tests in soils is dependent upon mobilizing the shearing strength along a certain failure surface, the theory is not directly related to the concrete popout problem.

DIMENSIONAL ANALYSIS OF POPOUT EXPANSIVE PRESSURE

Figure 17 is a free body diagram of a typical concrete popout. The force P required to cause a popout to occur is a function of the following variables:

$$P = f(T, N, \theta, h, d) \tag{7}$$

where

T is the shearing force on the popout cone surface

N is the normal force on the popout cone surface

θ is the angle between the failure plane and the horizontal

h is the height of the popout

d is the diameter of the base of the popout.

Written in terms of stresses rather than forces the above equation becomes:

$$\sigma_p = f(\tau, \sigma_n, \theta, h, d) \tag{8}$$

where

σ_p is the activating compressive stress acting on the base of the concrete popout

τ is the resisting shearing stress acting on the failure plane

σ_n is the normal stress acting on the failure plane

θ, h, and d are as defined in equation 7.

By Mohr-Coulomb theory it will be shown that when the maximum principal stress is zero τ and σ_n can be calculated if the tensile strength of the concrete σ_t and the failure plane θ, which is a function of the internal friction angle ϕ of the concrete, are known. Therefore

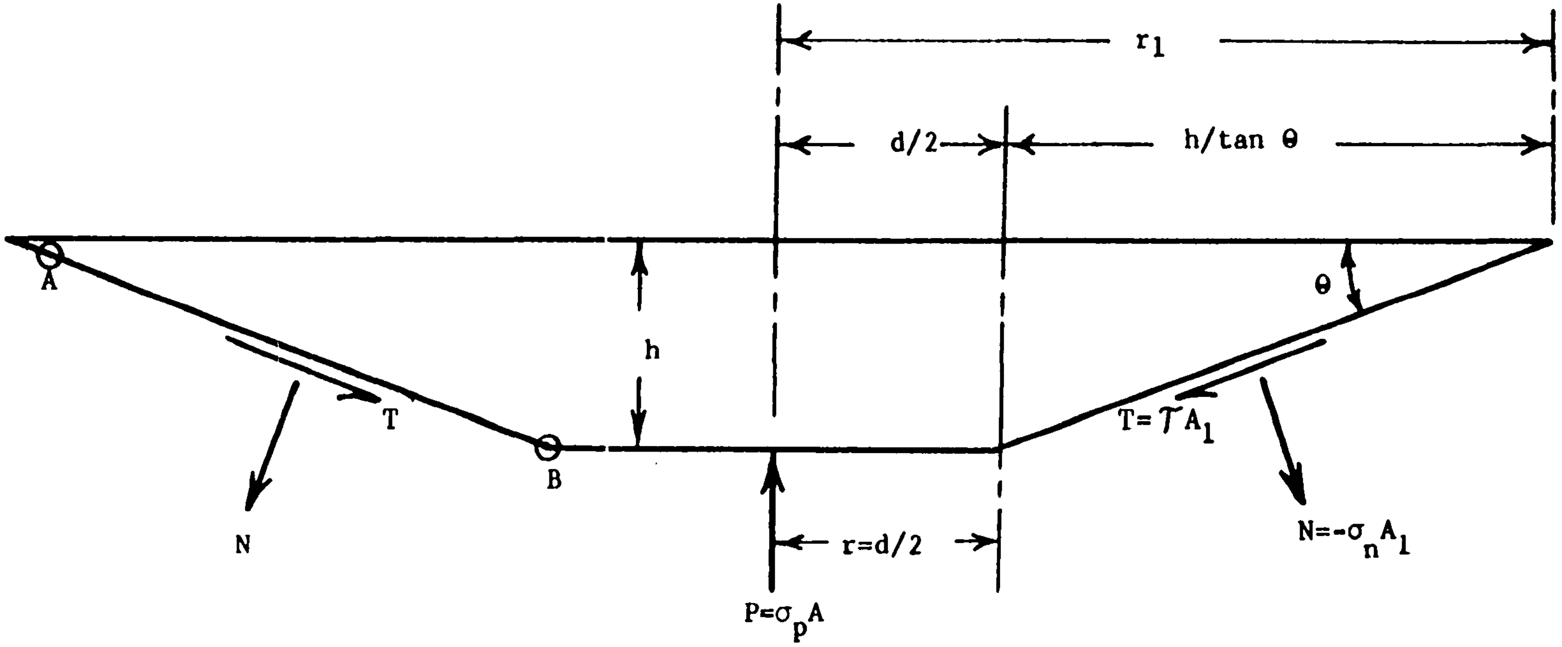

Figure 17. Concrete popout dimensions

equation 8 can be written as:

$$\sigma_p = f(\sigma_t, \phi, h, d) \tag{9}$$

where

σ_p is the activating compressive stress acting on the base of the concrete popout

σ_t is the tensile strength of the concrete

ϕ is the internal friction angle of the concrete

h is the height of the popout

d is the diameter of the base of the popout.

Dimensional analysis can be used to reduce the number of variables in the functional relationship shown in equation 9. The Buckingham pi theorem (24) is:

$$s = n - b \tag{10}$$

where

s is the number of π terms

n is the number of quantities involved

b is the number of basic dimensions involved.

Since in equation 9 there are 5 quantities and the two basic dimensions, force, F and length, L, the equation can be expressed in 5 - 2 = 3 dimensionless π terms. One such dimensionless relationship would be:

$$\frac{\sigma_p}{\sigma_t} = F\left(\frac{h}{d}, \phi\right) \tag{11}$$

The nature of this functional relationship will be hypothesized based upon the three following popout models.

POPOUT MODELS

Model I. Simple Punch Out

The shape of popout particle for this model is shown in Figure 18 and the free-body diagram is shown in Figure 19. The stresses on element A on the failure plane in Figure 19 are shown in Figure 20 and the corresponding Mohr's circle is shown in Figure 21. Since the magnitudes of the stresses on element A are not known and cannot be determined from equations of equilibrium an assumption must be made. The assumption is that the normal stress on the failure plane is zero. The Mohr's circle for this assumption is shown in Figure 22. The shearing stress on the failure plane is equal to the cohesion. The cohesion, c, is a function of the tensile strength, σ_t and the internal friction angle ϕ. From Figure 23

$$\tan \phi = \frac{c}{\sigma_t + x} \quad \text{or} \quad x = \frac{c}{\tan \phi} - \sigma_t \tag{12}$$

Also from Figure 23

$$\sin \phi = \frac{\frac{\sigma_t}{2}}{\frac{\sigma_t}{2} + x} \quad \text{or} \quad x = \frac{\sigma_t}{2 \sin \phi} - \frac{\sigma_t}{2} \tag{13}$$

Equating equations 12 and 13

$$\frac{c}{\tan \phi} = \sigma_t(1 - \tfrac{1}{2} + \frac{1}{2 \sin \phi})$$

or

$$\frac{c}{\sigma_t} = \tan \phi(\tfrac{1}{2} + \frac{1}{2 \sin \phi}) \tag{14}$$

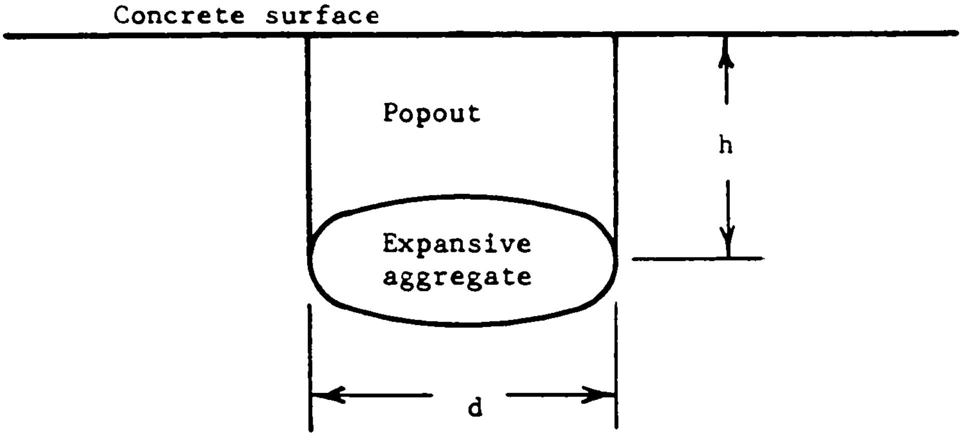

Figure 18. Model I--Simple punch out

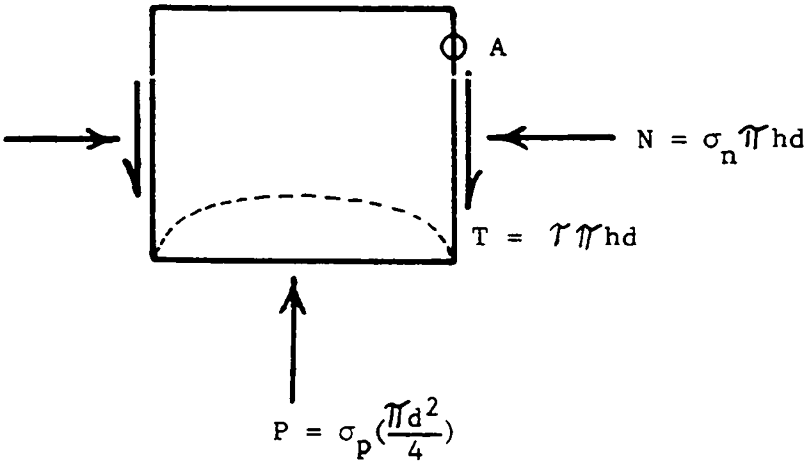

Figure 19. Free-body diagram for Model I--Simple punch out

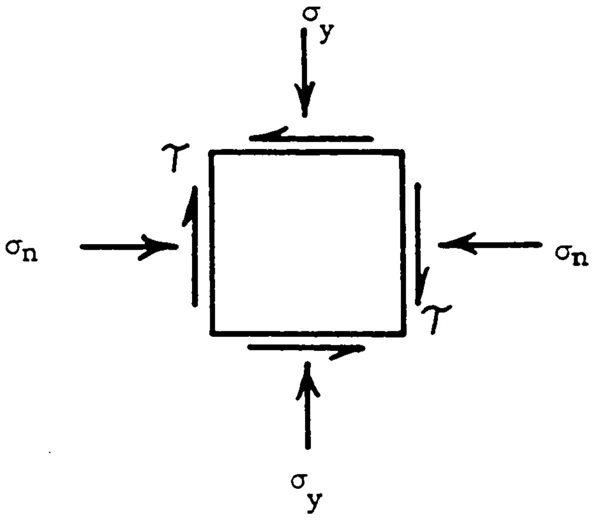

Figure 20. Stresses on failure plane for punch out model

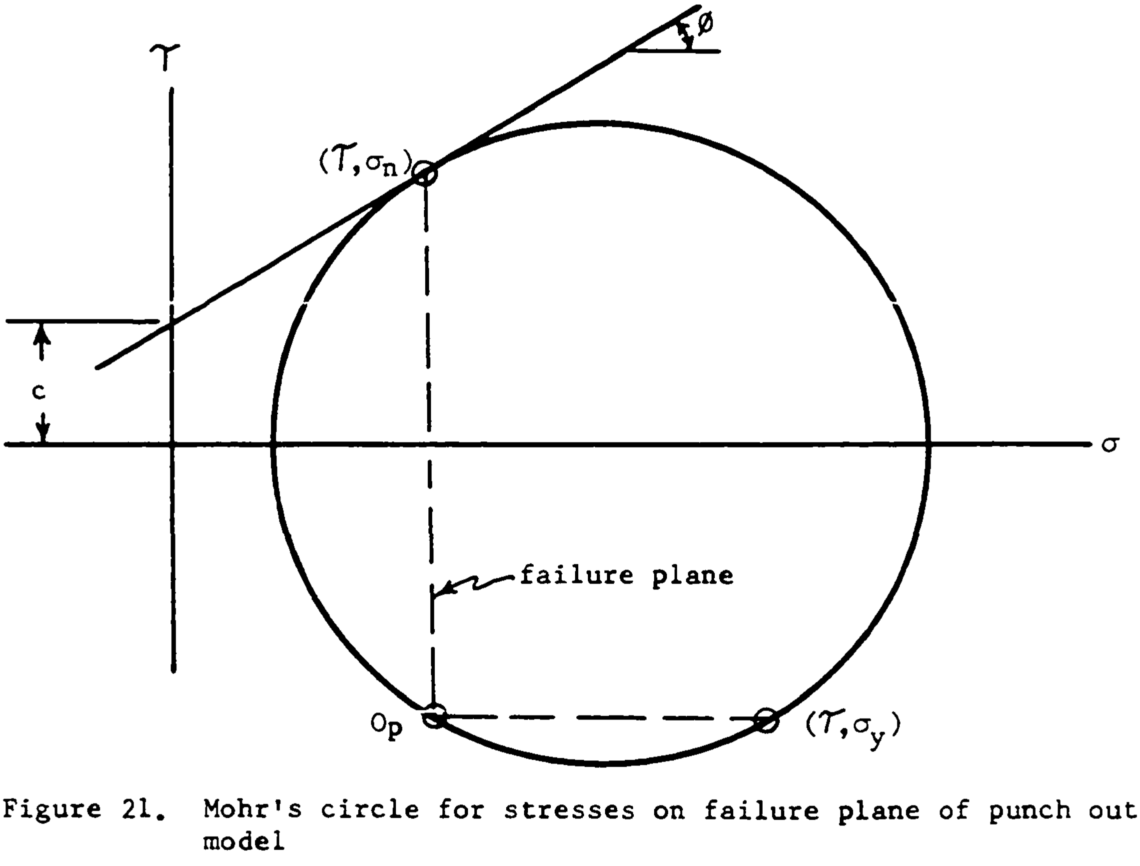

Figure 21. Mohr's circle for stresses on failure plane of punch out model

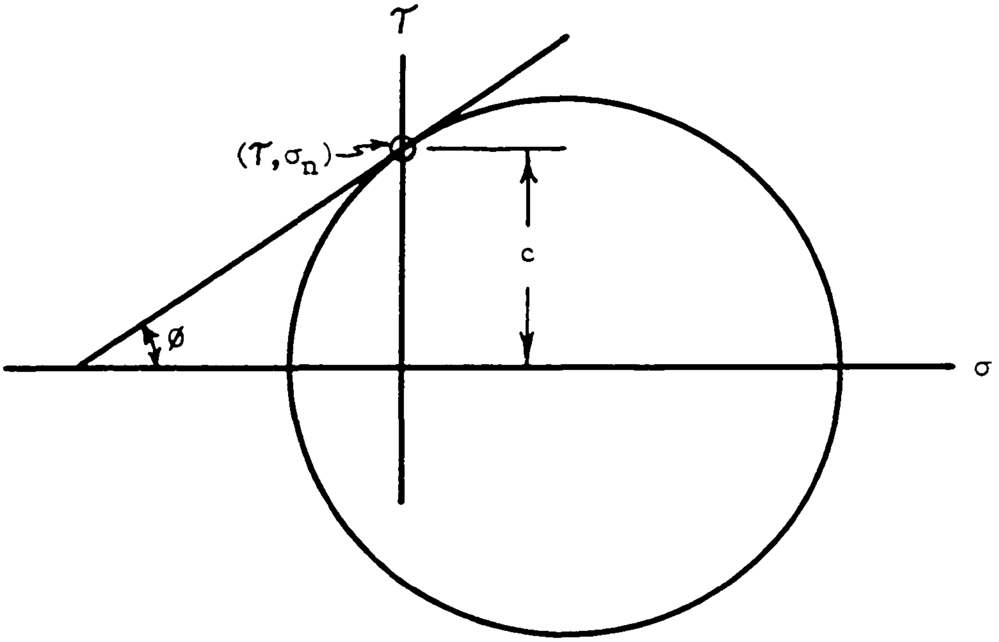

Figure 22. Assumed failure plane stresses for punch out model

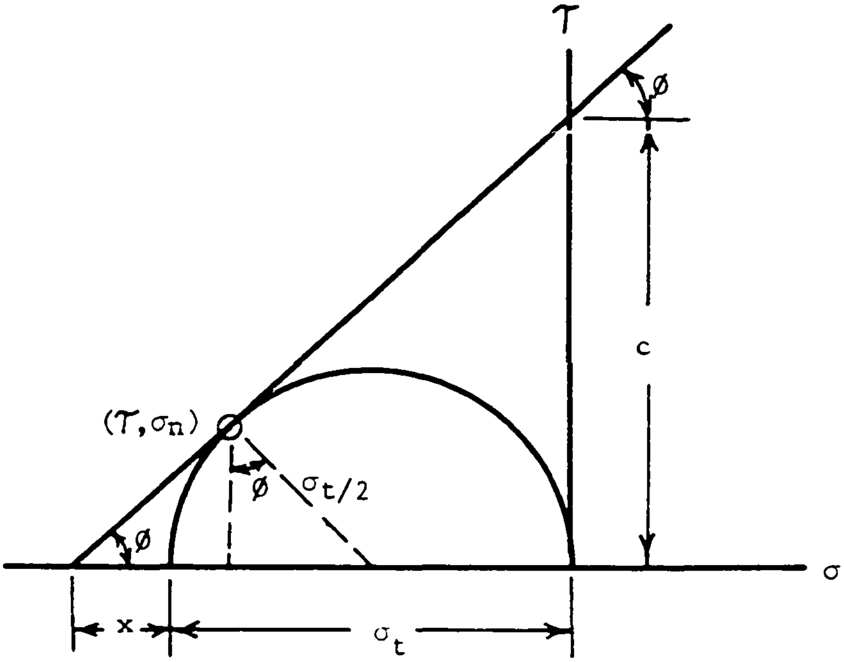

Figure 23. Mohr's circle relating tensile strength, cohesion, and internal friction

Summing the vertical forces shown in Figure 19 gives

$$\sigma_p\left(\frac{\pi d^2}{4}\right) = (\pi hd) \tag{15}$$

By the assumption that $\tau = c$, equation 14 can be substituted into equation 15 to obtain a relationship between the popout stress ratio σ_p/σ_t, ϕ and h/d

$$\sigma_p = 4\ c\ \frac{h}{d}$$

or

$$\sigma_p = 4\ \sigma_t\ \frac{h}{d}\ (\tan \phi)\ \left(\tfrac{1}{2} + \frac{1}{2 \sin \phi}\right)$$

or

$$\sigma_p/\sigma_t = 4 \tan \phi \left(\tfrac{1}{2} + \frac{1}{2 \sin \phi}\right) \frac{h}{d} \tag{16}$$

For popout Model I, equation 16 is the theoretically derived relationship between the dimensionless π terms shown in equation 11, the ratio of activating compressive stress to resisting tensile stress being a function of only h/d and ϕ. Equation 16 is the equation of a straight line passing through the origin with a slope of 4 tan $\phi(\tfrac{1}{2} + \frac{1}{2 \sin \phi})$ and is shown for several values of ϕ in Figure 24.

Model II. Mohr-Coulomb Failure Theory

The variables d, h, and θ shown in Figure 17 can be measured for a given popout. The three variables P, T, and N are unknown and cannot be determined by equations of equilibrium alone since only two such equations can be written for the forces shown in Figure 17. An assumption must, therefore, be made about the relationship between the shearing

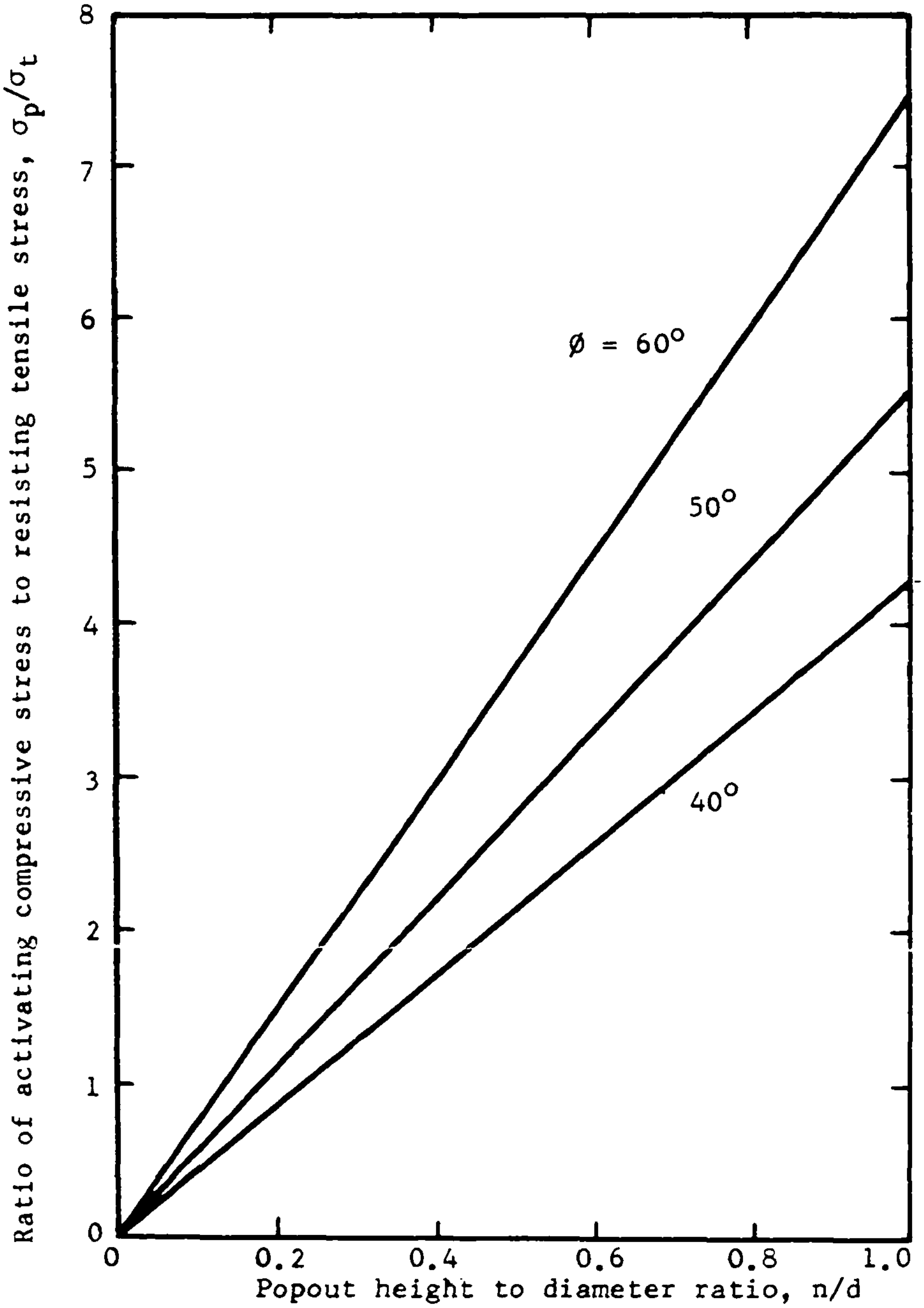

Figure 24. Dimensionless stress equation for concrete popouts, Model I--punching shear

and normal stresses and the principal stresses at points along the failure plane in order to estimate the force P required to cause a popout to occur. The assumption is probably best visualized by considering an element of concrete at point A on Figure 17. Such an element will have stresses acting on it as shown in Figure 25. The shearing stress on the surface is zero. The shearing stress on a vertical plane is also zero and the element fractures on a plane θ degrees from the horizontal due to the normal tensile stress σ_t. The assumption is that the failure envelope is linear and that the principal stresses are tensile on horizontal planes and compressive on vertical planes. The magnitude of the shearing stress, and the normal stress σ_n on the failure plane can be obtained from a Mohr's circle analysis as shown in Figure 26.

By summing forces shown in Figure 17 in the vertical direction the following equilibrium equation is obtained:

$$P = N \cos \theta + T \sin \theta \qquad (17)$$

or since force = stress times area over which the stress acts:

$$\sigma_p A = A_1(-\sigma_n \cos \theta + \tau \sin \theta) \qquad (18)$$

where σ_p is the activating compressive stress and

$$A = \frac{\pi d^2}{4} \quad , \qquad (19)$$

the area of the truncated end of the popout cone and the area over which the alkali-shale reaction products act, and

$$A_1 = \pi (r + r_1) \sqrt{h^2 + (r_1 - r)^2} \ , \qquad (20)$$

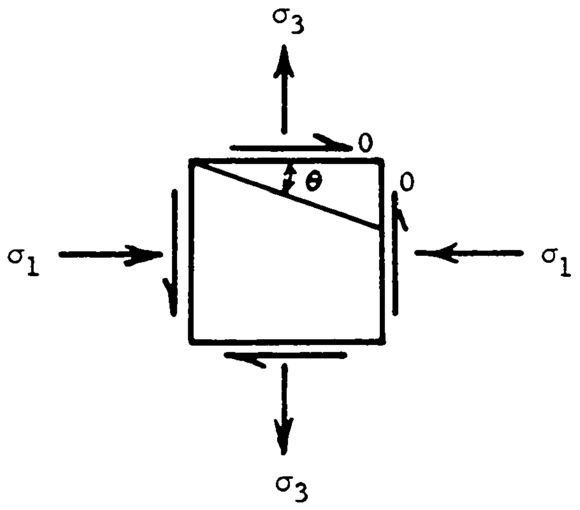

Figure 25. Principal stresses at point A in Figure 17

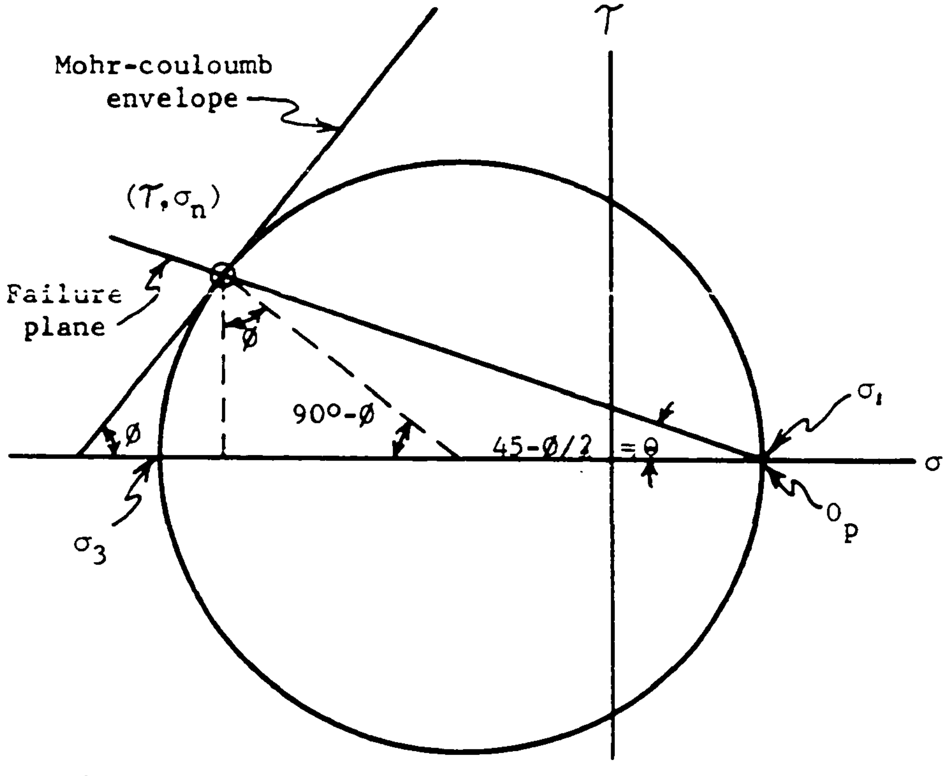

Figure 26. Mohr's circle analysis for concrete popout failure stresses

the surface area of the frustrum of a right cone and the area over which both the shearing stress, τ and the normal stress σ_n act.

The relationship between τ and σ_n is obtained from Mohr-Coulomb theory:

$$\tau = \sigma_n \tan \phi + c \tag{21}$$

Substituting equation 21 into equation 18

$$\sigma_p \frac{A}{A_1} = (\sigma_n \tan \phi + c) \sin \theta - \sigma_n \cos \theta \tag{22}$$

Dividing by the tensile strength σ_t equation 22 becomes

$$\frac{\sigma_p}{\sigma_t} \left(\frac{A}{A_1} \right) = \left(\frac{\sigma_n}{\sigma_t} \tan \phi + \frac{c}{\sigma_t} \right) \sin \theta - \frac{\sigma_n}{\sigma_t} \cos \theta \tag{23}$$

or

$$\frac{\sigma_p}{\sigma_t} \left(\frac{A}{A_1} \right) = \frac{\sigma_n}{\sigma_t} (\tan \phi \sin \theta - \cos \theta) + \frac{c}{\sigma_t} \sin \theta \tag{24}$$

This is the equation of a straight line with the slope and intercept dependent upon the material properties c, ϕ, and σ_t which can be determined from laboratory tests. The area ratio can be determined from the popout dimensions. The normal stress σ_n on the failure plane is not known and the solution of the popout problem is statically indeterminant to the first degree.

The indeterminancy would be removed if σ_n were known or if a reasonable value could be assumed. If σ_n is tensile then the lower limit can be determined from Figure 23:

$$\sigma_n = \frac{\sigma_t}{2} + \frac{\sigma_t}{2} \sin \phi$$

or

$$\frac{\sigma_n}{\sigma_t} = \tfrac{1}{2}(1 + \sin \phi) \tag{25}$$

As will be shown later, σ_1 is probably not more than $-2\sigma_3$. If $\sigma_1 = -2\sigma_3$ then the upper limit on σ_n/σ_t can be derived from Figure 26 and the Mohr-Coulomb relationship:

$$\tau = \frac{\sigma_1 - \sigma_3}{2} \cos \phi = \sigma_n \tan \phi + c \ . \tag{26}$$

$$\text{Since } \sigma_1 = -2\sigma_3 \tag{27}$$

$$\text{then } \frac{-3}{2} \sigma_3 \cos \phi = \sigma_n \tan \phi + c \tag{28}$$

$$\text{or } \sigma_3 = -\frac{2}{3}\left(\frac{\sigma_n \tan \phi + c}{\cos \phi}\right) . \tag{29}$$

Also from Figure 26

$$\sigma_n = \frac{\sigma_1 + \sigma_3}{2} - \frac{\sigma_1 - \sigma_3}{2} \sin \phi \tag{30}$$

Substituting equation 27 into equation 30,

$$\sigma_n = \frac{-\sigma_3}{2} + \frac{3}{2} \sigma_3 \sin \phi \ . \tag{31}$$

Substituting equation 29 into equation 31

$$\sigma_n = \frac{\sigma_n \tan \phi + c}{3 \cos \phi} - (\sigma_n \tan \phi + c) \tan \phi \tag{32}$$

$$\begin{aligned} \text{or} \quad 0 &= -\sigma_n + \frac{\sigma_n \tan \phi}{3 \cos \phi} + \frac{c}{3 \cos \phi} - \sigma_n \tan^2 \phi - c \tan \phi \\ \text{or} \quad 0 &= \sigma_n \left(-1 + \frac{\tan \phi}{3 \cos \phi} - \tan^2 \phi\right) + c\left(\frac{1}{3 \cos \phi} - \tan \phi\right) . \end{aligned} \tag{33}$$

Dividing both terms by σ_t and rearranging

$$\frac{\sigma_n}{\sigma_t} = \frac{\frac{c}{\sigma_t}\left(\frac{1}{3 \cos \phi} - \tan \phi\right)}{1 + \tan^2 \phi - \frac{\tan \phi}{3 \cos \phi}} \ . \tag{34}$$

The $\frac{\sigma_n}{\sigma_t}$ stress ratio must be in the range given by equations 25 and 34

$$\tfrac{1}{2}(1 + \sin \phi) \geq \frac{\sigma_n}{\sigma_t} \geq \frac{\frac{c}{\sigma_t}\left(\frac{1}{3 \cos \phi} - \tan \phi\right)}{1 + \tan^2\phi - \frac{\tan \phi}{3 \cos \phi}} \tag{35}$$

Graphs of equation 24 for various values of ϕ and the corresponding c/σ_t values computed by equation 14 are shown in Figure 27. The range in possible σ_n/σ_t values as given by equation 35 is also shown on Figure 27. As the value of ϕ increases, the error in predicting σ_p/σ_t decreases. For a ϕ of 50° if one assumed $\sigma_1 = 0$ and $\sigma_3 = \sigma_t$ the corresponding value of $\sigma_p/-\sigma_t$ (A/A_1) would be 0.74. If one assumed $\sigma_1 = -2\sigma_3$ then $\sigma_c/-\sigma_t$ (A/A_1) would be 0.94 or about 1.27 times larger.

In order to derive the relationship between popout pressure and popout height-diameter ratio it will be assumed that $\sigma_1 = 0$ and $\sigma_3 = \sigma_t$. If this assumption is incorrect it will predict popout pressures lower than would otherwise be predicted.

If $\sigma_1 = 0$ and $\sigma_3 = \sigma_t$, the magnitude of the stresses on the failure plane can be obtained from a Mohr's circle analysis as shown in Figure 23. The relationship between the stresses (τ, σ_n) on the failure plane and the principal stress, σ_t, and also the relationship between the failure plane angle, θ and the friction angle for the concrete, ϕ can be obtained from the Mohr's circle and are as follows:

$$\sigma_n = \frac{\sigma_t}{2} + \frac{\sigma_t}{2} \sin \phi = \frac{\sigma_t}{2} (1 + \sin \phi) \tag{36}$$

$$\tau = \frac{\sigma_t}{2} \cos \phi \tag{37}$$

$$\theta = 45^\circ - \frac{\phi}{2} \tag{38}$$

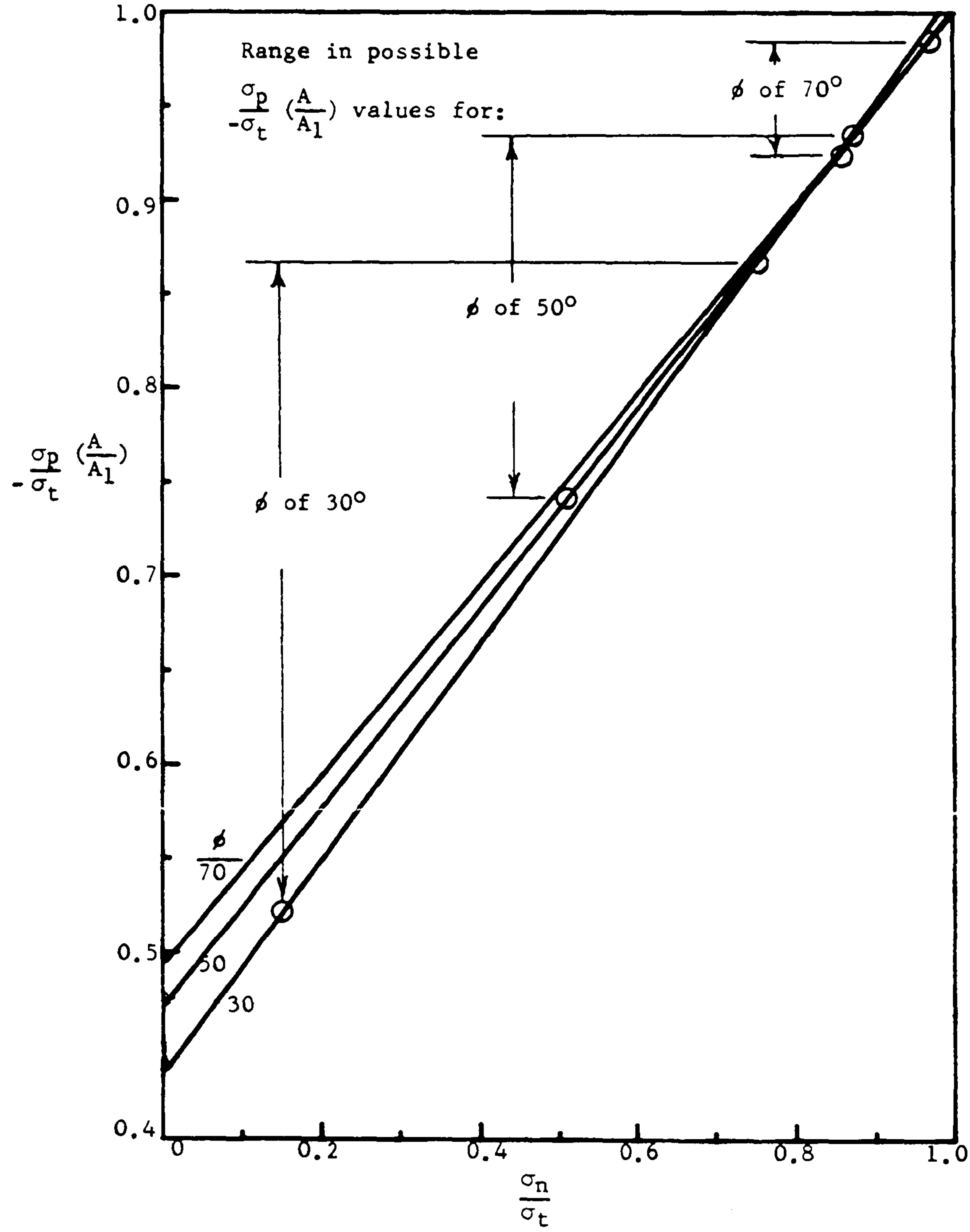

Figure 27. Popout pressure as a function of stress on the failure plane

The value of r_1 in equation 20 is obtained from Figure 17 as

$$r_1 = r + h/\tan\Theta \qquad (39)$$

Substituting equation 39 into equation 20 results in:

$$A_1 = \pi(r + h/\tan\Theta + r)\sqrt{h^2 + h^2/\tan^2\Theta}$$

or $$A_1 = \pi h(d + h/\tan\Theta)\sqrt{1 + 1/\tan^2\Theta}$$

or $$A_1 = \pi h^2(d/h + 1/\tan\Theta)\sqrt{1 + 1/\tan^2\Theta}\,. \qquad (40)$$

When equation 38 is substituted into equation 40 the surface area of the frustrum of a right cone becomes:

$$A_1 = \pi h^2\left[\frac{d}{n} + \frac{1}{\tan(45-\frac{\phi}{2})}\right]\left[1 + \frac{1}{\tan^2(45-\frac{\phi}{2})}\right]^{\frac{1}{2}}$$

or

$$A_1 = \pi h^2\left[\frac{d}{n} + \frac{1}{\tan(45-\frac{\phi}{2})}\right]\left[\frac{1}{\tan(45-\frac{\phi}{2})}\right]\left[1 + \tan^2(45-\frac{\phi}{2})\right]^{\frac{1}{2}}. \qquad (41)$$

When the relationships between failure stresses and principal stresses, equations 36 and 37 are substituted into equation 18 the ratio of the activating compressive stress to the resisting tensile stress of the concrete becomes:

$$\frac{\sigma_p}{\sigma_t} = \frac{A_1}{2A}(\cos\Theta + \sin\phi\cos\Theta + \cos\phi\sin\Theta) \qquad (42)$$

Since $\sin\phi\cos\Theta + \cos\phi\sin\Theta = \sin(\phi + \Theta)$ equation 42 becomes:

$$\frac{\sigma_p}{\sigma_t} = \frac{A_1}{2A}[\cos\Theta + \sin(\phi + \Theta)] \qquad (43)$$

Substitution of equation 38 into equation 43 gives:

$$\frac{\sigma_p}{\sigma_t} = \frac{A1}{2A}\left[\cos\left(45^{\circ} - \frac{\phi}{2}\right) + \sin\left(45^{\circ} + \frac{\phi}{2}\right)\right] \qquad (44)$$

Substitution of equations 19 and 41 into equation 44 the popout stress ratio becomes:

$$\frac{\sigma_p}{\sigma_t} = \frac{\pi h^2}{2\pi \frac{d^2}{4}}\left[\left(\frac{d}{n}\right)\frac{1}{\tan(45^{\circ}-\frac{\phi}{2})} + \frac{1}{\tan^2(45^{\circ}-\frac{\phi}{2})}\right]\left[1 + \tan^2\left(45^{\circ}- \frac{\phi}{2}\right)\right]^{\frac{1}{2}}$$

$$\left[\cos\left(45^{\circ} - \frac{\phi}{2}\right) + \sin\left(45^{\circ} - \frac{\phi}{2}\right)\right] \qquad (45)$$

Since $\sin(45^{\circ} + \frac{\phi}{2}) = \cos(45^{\circ} - \frac{\phi}{2})$ and $\frac{1}{\cos(45^{\circ}-\frac{\phi}{2})} =$ $[1 + \tan^2(45^{\circ} - \frac{\phi}{2})]^{\frac{1}{2}}$ equation 45 reduces to:

$$\frac{\sigma_p}{\sigma_t} = 4\left(\frac{h}{d}\right)^2\left[\left(\frac{h}{d}\right)\frac{1}{\tan(45^{\circ}-\frac{\phi}{2})} + \frac{1}{\tan^2(45^{\circ}-\frac{\phi}{2})}\right]$$

or

$$\frac{\sigma_p}{\sigma_t} = \frac{4}{\tan^2(45^{\circ}-\frac{\phi}{2})}\left(\frac{h}{d}\right)^2 + \frac{4}{\tan(45^{\circ}-\frac{\phi}{2})}\left(\frac{h}{d}\right) \qquad (46)$$

For popout Model II equation 46 is the theoretically derived relationship between the dimensionless π terms shown in equation 11. The ratio of activating compressive stress to resisting tensile stress is a function of only h/d and ϕ. Equation 46 can be simplified by defining the following constants which will be called influence coefficients. They are only a function of the internal friction angle of the concrete.

$$K_1 = 4/\tan^2(45^{\circ} - \phi/2) \qquad (47)$$

$$K_2 = 4/\tan(45^{\circ} - \phi/2) \qquad (48)$$

Substitution of equation 47 and 48 into equation 46 yields:

$$\frac{\sigma_p}{\sigma_t} = K_1(h/d)^2 + K_2(h/d) \qquad (49)$$

This is the equation of a parabola and is plotted for several values of ϕ in Figure 28. The vertex of each parabola has the coordinates $(-K_3, -K_4)$ where:

$$-K_3 = K_2/2K_1 = \tfrac{1}{2}[\tan(45-\phi/2)] \qquad (50)$$

$$-K_4 = K_2^2/4K_1 = 1 \qquad (51)$$

Values of the influence coefficients and the parabola vertex coordinate are given in Table 14 and Figure 29. Equations 47, 48 and 50 were programmed for a computer and Figure 29 was plotted by the computer plotter using 1/10 inch straight line increments.

Table 14. Influence coefficients and parabola vertex constants for concrete popout equation, $\sigma_c/\sigma_t = K_1(h/d)^2 + K_2(h/d)$

Friction angle ϕ	Failure plane $\theta = 45 - \frac{\phi}{2}$	$K_1 = 4/\tan^2(45-\frac{\phi}{2})$	$K_2 = 4/\tan(45-\frac{\phi}{2})$	$-K_3 = \frac{1}{2}\tan(45-\frac{\phi}{2})$
24	33	9.48	6.16	0.3247
26	32	10.24	6.40	0.3124
28	31	11.08	6.66	0.3004
30	30	12.00	6.93	0.2887
32	29	13.02	7.22	0.2772
34	28	14.15	7.52	0.2659
36	27	15.41	7.85	0.2548
38	26	16.82	8.20	0.2439
40	25	18.40	8.58	0.2332
42	24	20.18	8.98	0.2226
44	23	22.20	9.42	0.2122
46	22	24.50	9.90	0.2020
48	21	27.15	10.42	0.1919
50	20	30.19	10.99	0.1820

Table 14. (Continued)

Friction angle ϕ	Failure plane $\theta = 45 - \frac{\phi}{2}$	$K_1 = 4/\tan^2(45 - \frac{\phi}{2})$	$K_2 = 4/\tan(45 - \frac{\phi}{2})$	$-K_3 = \frac{1}{2}\tan(45 - \frac{\phi}{2})$
52	19	33.74	11.62	0.1722
54	18	37.89	12.31	0.1625
56	17	42.79	13.08	0.1529
58	16	48.65	13.95	0.1434
60	15	55.71	14.93	0.1340
62	14	64.35	16.04	0.1247
64	13	75.05	17.33	0.1154
66	12	88.53	18.82	0.1063
68	11	105.87	20.58	0.0972
70	10	128.65	22.69	0.0882

Model III. Simple Tension Theory

Although the stresses on a horizontal plane through point A of Figure 17 are undoubtedly tensile as assumed in Model II the stresses on a horizontal plane through point B of Figure 17 are compressive. There must, then, be a transition of stresses on the horizontal plane from compressive near the swelling inclusion to tensile near the surface of the concrete.

The principal stresses at the concrete-aggregate interface represented by point B in Figure 30 would be normal and tangential to the surface of the inclusion. For a swelling inclusion the principal stress normal to the inclusion would be compressive and the principal stress tangential to the inclusion would be tensile as shown in Figure 31.

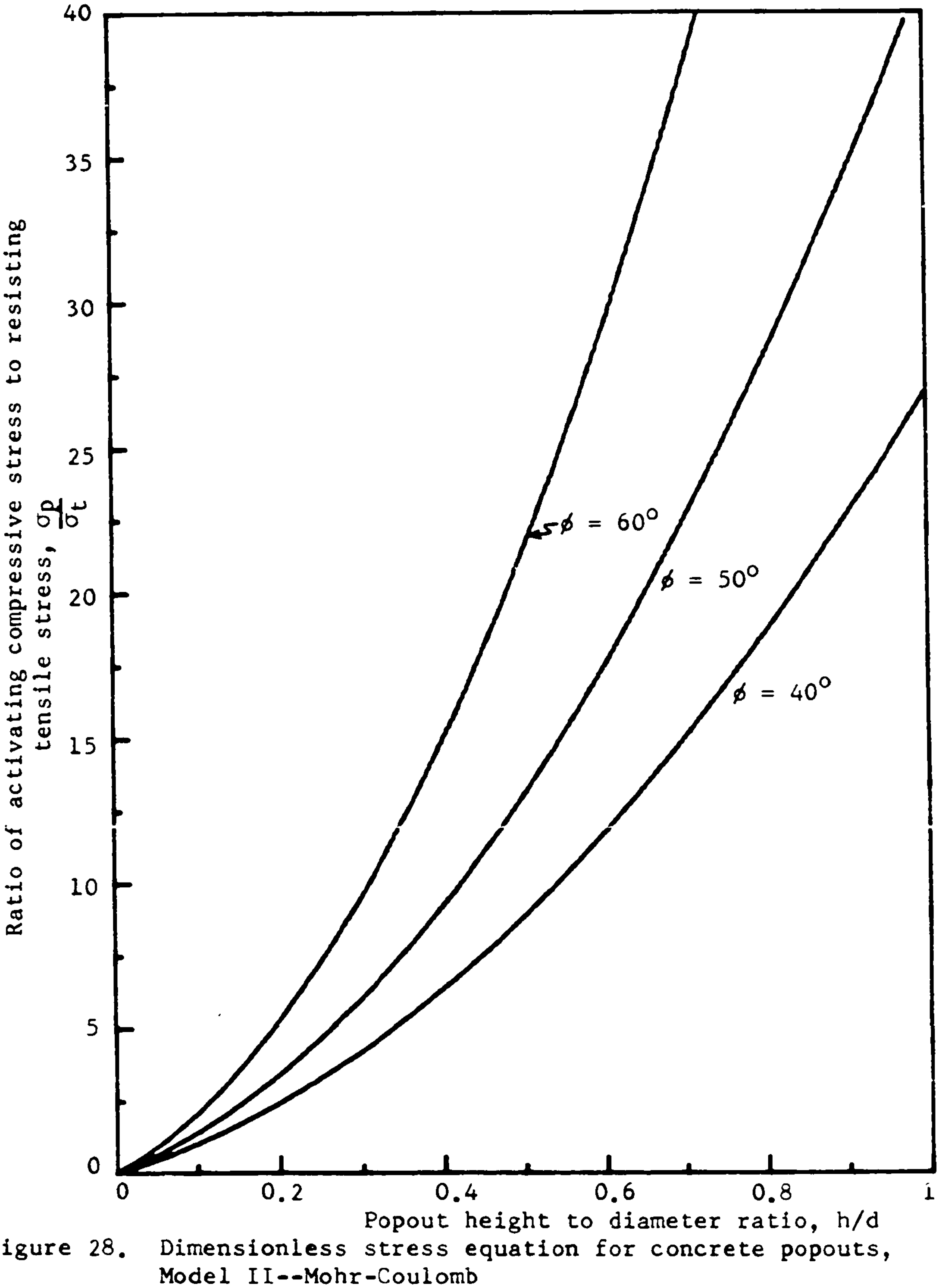

Figure 28. Dimensionless stress equation for concrete popouts, Model II--Mohr-Coulomb

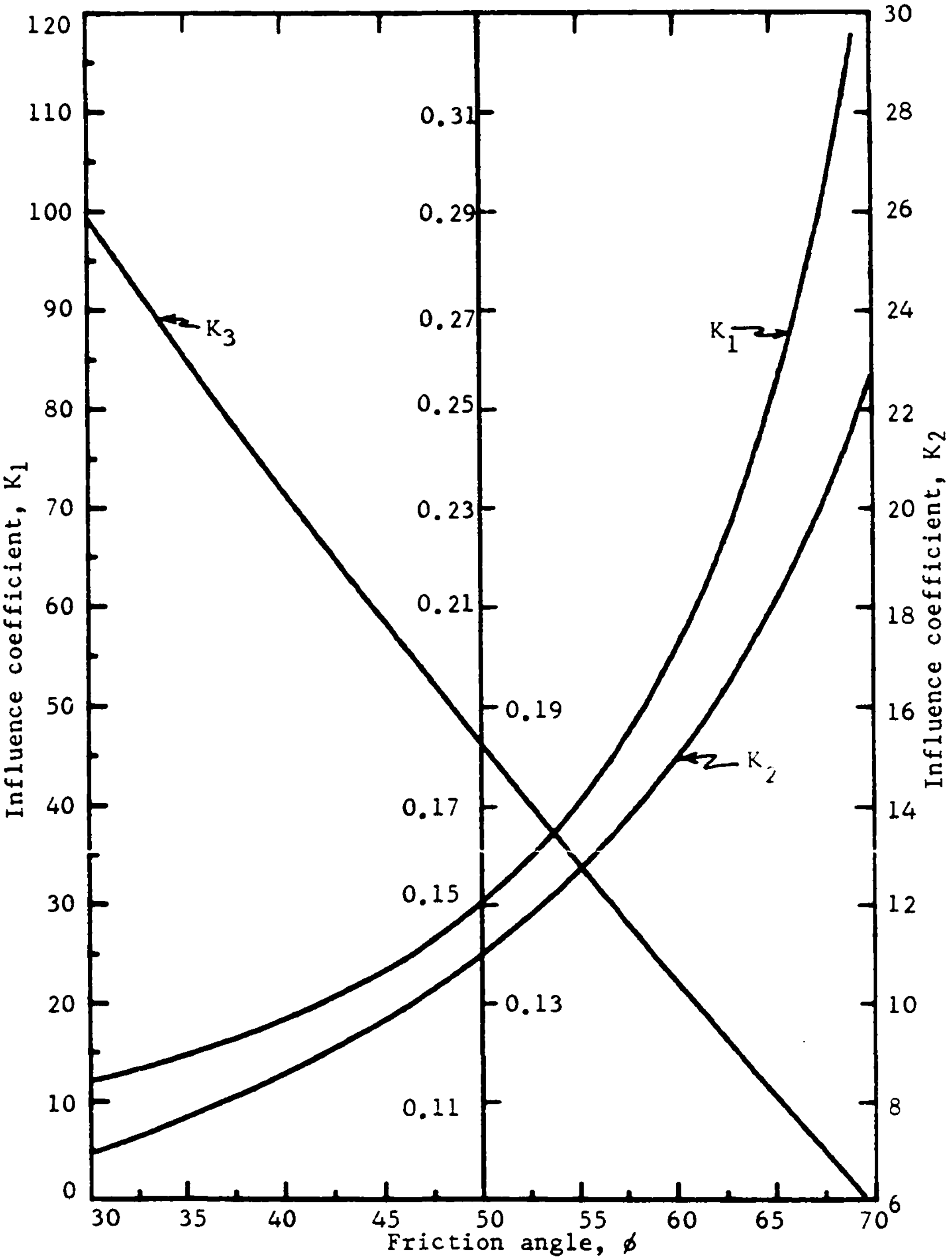

Figure 29. Influence coefficients for concrete popout stress equation

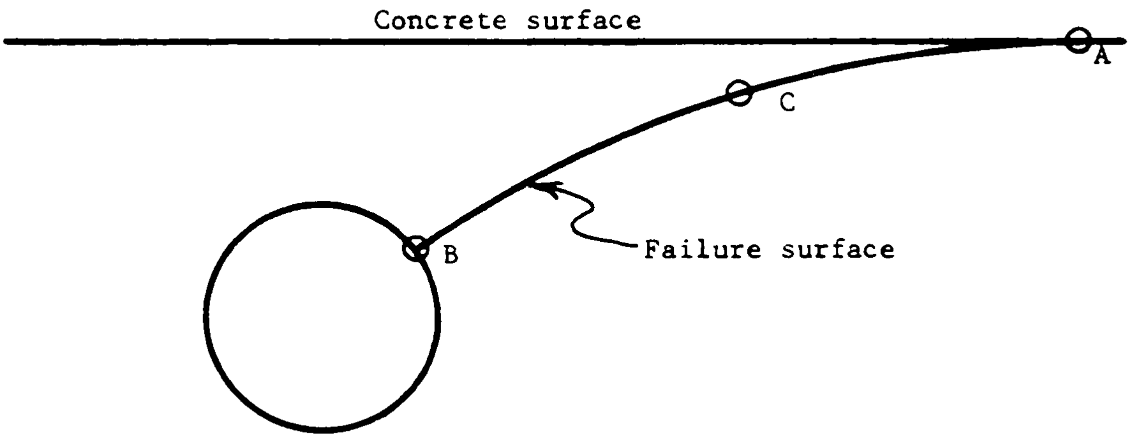

Figure 30. Circular popout failure surface

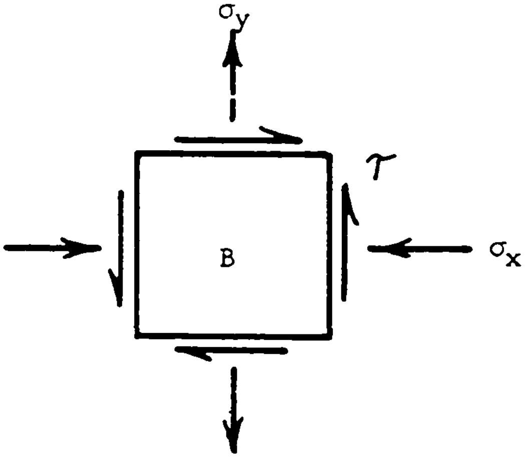

Figure 31. Stress element at aggregate-concrete interface

Applying equations given by Timoshenko and Goodier (22) the relationship between inclusion pressure, P, and tangential tensile stress, T, with a concentric inclusion in an elastic media is:

$$T = \frac{P}{2} \left[\frac{2 \left(\frac{D}{2} \right)^3 + H^3}{H^3 - \left(\frac{D}{2} \right)^3} \right] \tag{52}$$

or

$$\frac{P}{T} = \frac{2\,H^3 - 2\left(\frac{D}{2} \right)^3}{2\left(\frac{D}{2} \right)^3 + H^3} \tag{53}$$

Dividing equation 53 by D^3

$$\frac{P}{T} = \frac{2\left(\frac{H}{D}\right)^3 - \frac{1}{4}}{\frac{1}{4} + \left(\frac{H}{D}\right)^3} = \frac{2 - \frac{1}{4(H/D)^3}}{\frac{1}{4\left(\frac{H}{D}\right)^3} + 1} \tag{54}$$

From equation 54 it is evident that as:

$$\frac{H}{D} \dashrightarrow 0.5 \qquad \frac{P}{T} \dashrightarrow 0 \tag{55}$$

and as:

$$\frac{H}{D} \dashrightarrow \infty \qquad \frac{P}{T} \dashrightarrow 2\ . \tag{56}$$

A plot of equation 54 is shown in Figure 32. The compressive pressure exerted by the inclusion will never be greater than twice the tensile stress tangent to the inclusion. For H/D values less than 0.8 the radial compressive stress will be equal to or less than the tangential tensile stress.

The stress element at point B of Figure 30 is shown in Figure 31. The corresponding Mohr's circle is shown in Figure 33. The assumed

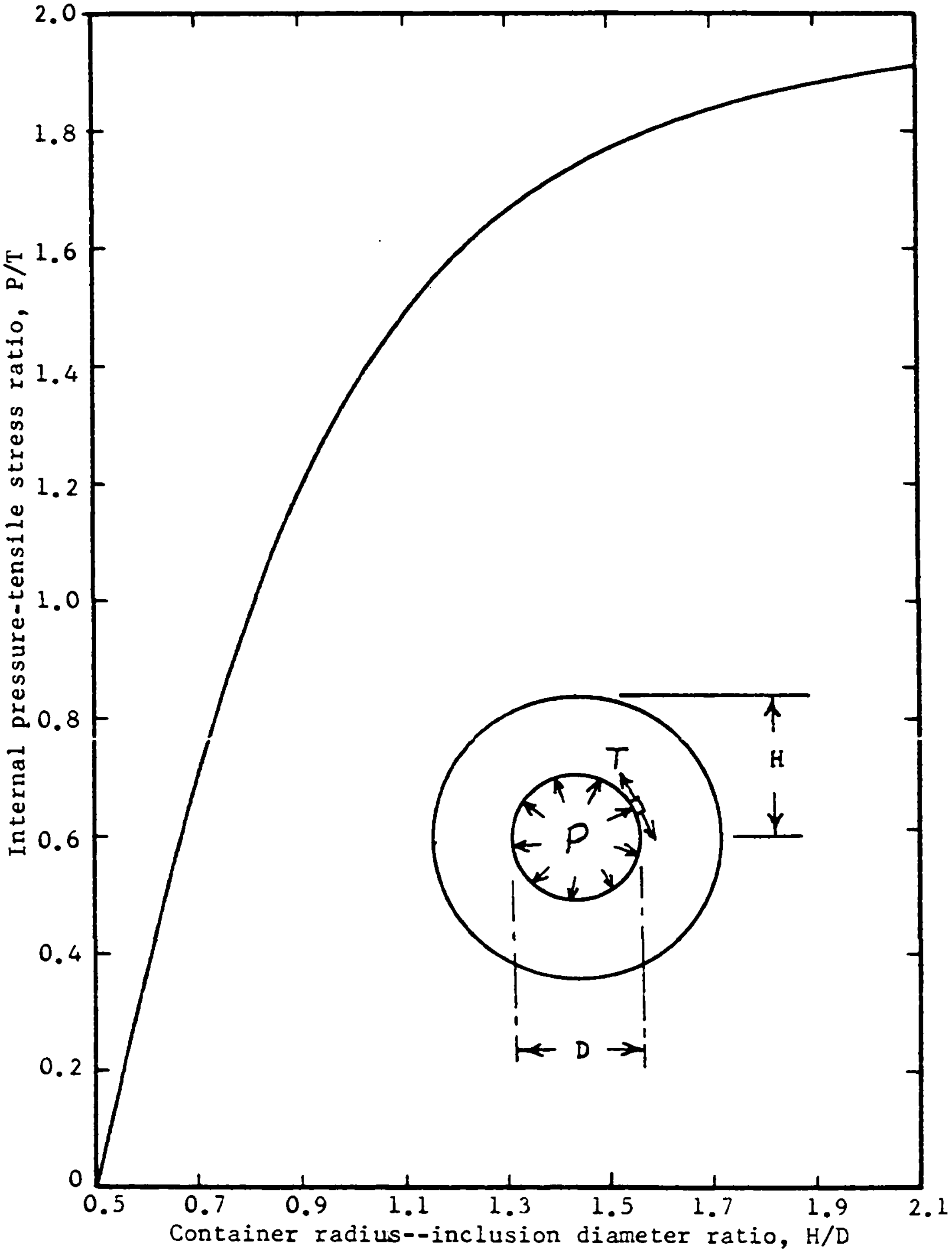

Figure 32. Tensile stress at inner face of spherical container

failure plane in Figure 30 is normal to the inclusion and follows a circular arc that becomes tangent to the surface. The stress on the failure plane at point B is a principal stress and is tensile since the stress is tangent to the inclusion. The failure stresses at point B are represented by (o, σ_3) in Figure 33. The failure stress (o, σ_3) in Figure 33 is below the Mohr-Coulomb failure envelope which would indicate no failure. The question arises as to the shape of the failure envelope in the vicinity of tensile normal stresses. If σ_t is the unconfined tensile strength, then a triaxial tensile test will not result in a stress state represented by a circle tangent to point b in Figure 33.

Tinoco (25) stated that for brittle materials the failure envelope must be perpendicular to the σ axis at the point of intersection. He assumed a parabolic failure envelope in the (τ, $-\sigma$) quadrant and a straight line failure envelope in the (τ, σ) quadrant with the point of tangency being at (τ, o) and the parabola vertex being at σ_t. Several soil mechanics texts show that the failure envelope in the (τ, σ) quadrant for soils is curved rather than straight. Equations for a parabolic failure envelope tangent to a straight line will be derived below. The cohesion c is related to σ_c and ϕ as shown in Figure 34 for a straight-line envelope:

$$\sin \phi = \frac{\sigma_c/2}{a + \sigma_c/2} \quad \text{or} \quad a(\sin \phi) = \sigma_c/2 - (\sigma_c/2)\sin \phi$$

or

$$a = \frac{\sigma_c/2\ (1 - \sin \phi)}{\sin \phi} \tag{57}$$

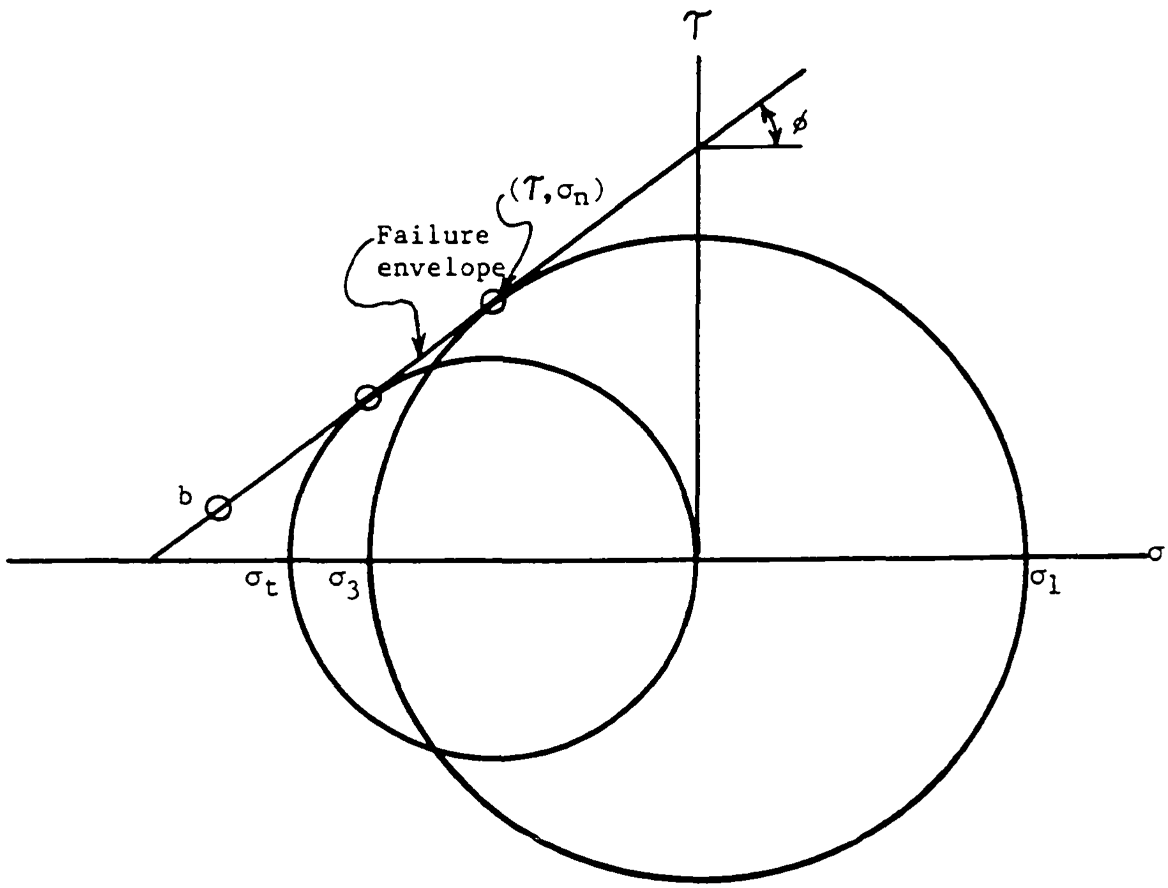

Figure 33. Mohr's circle for stresses at the aggregate-concrete interface--straight line failure envelope

$$\tan \phi = c/a \qquad (58)$$

Substituting equation 57 into equation 58

$$c = \frac{\sigma_{c/2}\ (1-\sin \phi) \tan \phi}{\sin \phi} \ . \qquad (59)$$

The equation of the line is $\tau = \sigma \tan \phi + c$ (60)

The slope of the line is $\tau' = \tan \phi$ (61)

Examination of equation (57) indicates that if $\phi = 30^\circ$ the intrinsic strength a is $\sigma c/2$. For concrete the tensile strength is usually near $\sigma c/10$. Therefore the straight-line failure envelope must not hold for tensile stresses. As stated above for brittle materials failing in simple tension the failure envelope must intersect the σ axis at right angles.

Figure 35 shows a parabolic failure envelope tangent to a Mohr-Coulomb straight line envelope. The equation of a parabola is

$$\sigma = -a_1 \tau^2 + \sigma_t \ . \qquad (62)$$

The first derivative of equation 62 is

$$\sigma' = -2\ a_1 \tau .$$

Hence

$$\tau' = \frac{1}{\sigma'} = \frac{1}{-2\ a_1 \tau} \ . \qquad (63)$$

Equating equation 63 and 61

$$\tan \phi = \frac{1}{-2\ a_1 \tau} \quad \text{or} \ -2a_1 \tau \tan \phi = 1 \ . \qquad (64)$$

From equation 62 $$a_1 = \frac{\sigma_t - \sigma}{\tau^2} \ . \qquad (65)$$

From equation 60 $$\sigma = \frac{\tau - c}{\tan \phi} \ . \qquad (66)$$

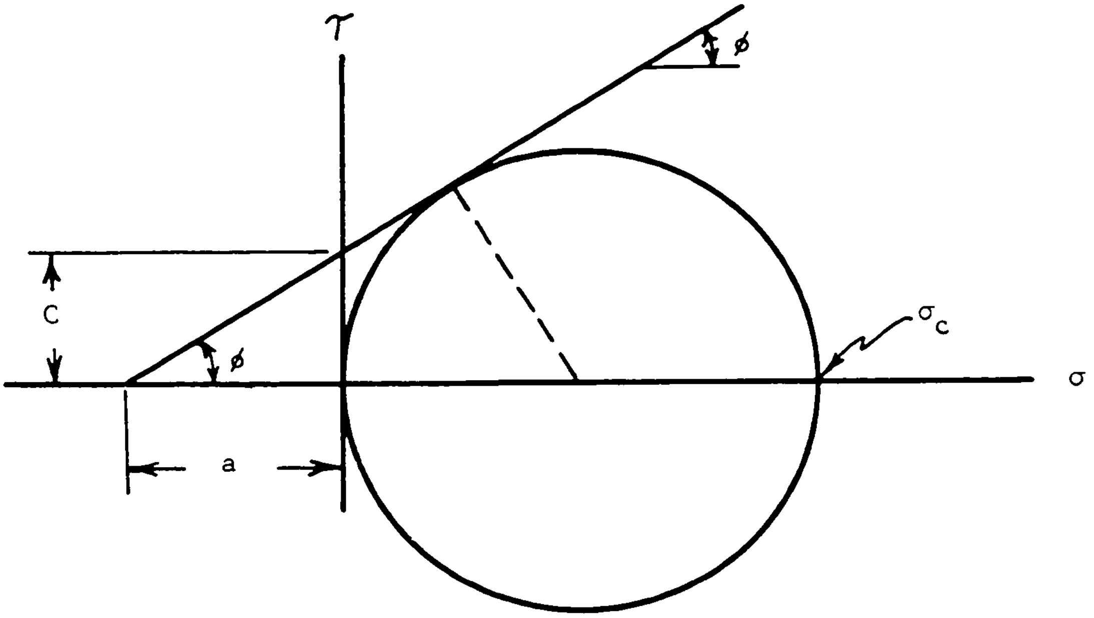

Figure 34. Cohesion C as related to σ_c and ϕ

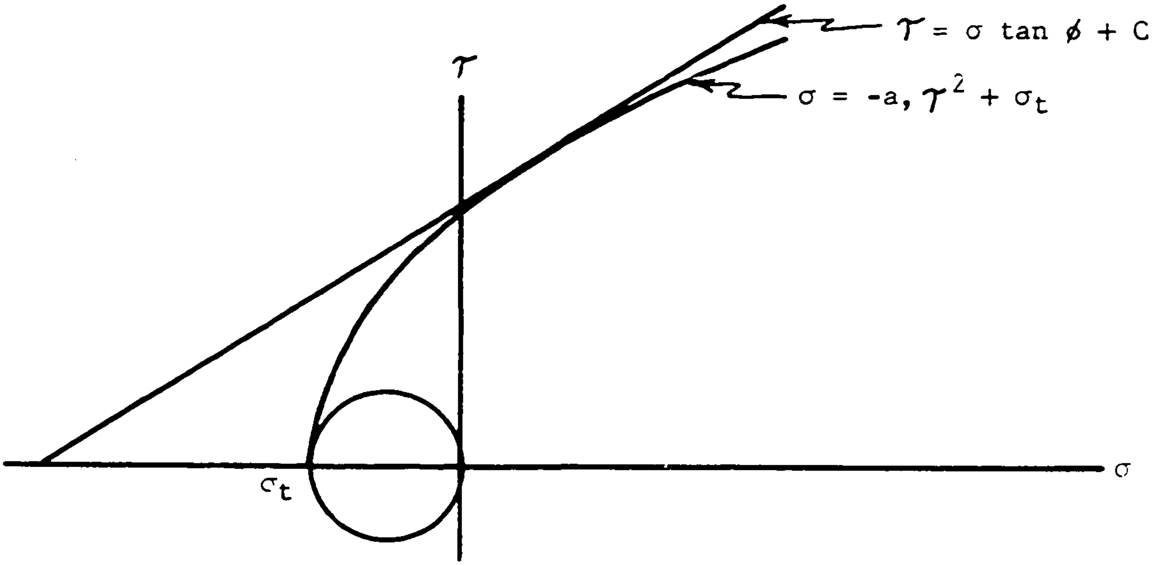

Figure 35. Parabolic envelope tangent to straight line envelope

Substituting equation 66 in equation 65

$$a_1 = \frac{\sigma_t - (\tau - c)/\tan \phi}{\tau^2} \quad . \tag{67}$$

Substituting equation 67 in equation 64 the value of τ gives the point where the parabolic envelope becomes tangent to the straight line envelope.

$$-2\tau \tan \phi \left[\frac{\sigma_t - (\tau - c)/\tan \phi}{\tau^2} \right] = 1$$

or

$$\tau = 2\tau - 2c - 2\sigma_t \tan \phi$$

or $$\tau = 2(c + \sigma_t \tan \phi) \quad . \tag{68}$$

Substituting equation 68 into equation 67 the constant a_1 can be determined in terms of c, ϕ, and σ_t.

$$a_1 = \frac{\sigma_t \tan \phi - 2(c + \sigma_t \tan \phi) + c}{\tan \phi [2(c+\sigma_t \tan \phi)]^2}$$

where c is obtained from equation 59. Substituting equation 68 into equation 60 the value of σ gives the point where the parabolic envelope becomes tangent to the straight line envelope.

$$2c + 2\sigma_t \tan \phi = \sigma \tan \phi + c$$

or

$$\sigma = \frac{c}{\tan \phi} + 2\sigma_t \tag{70}$$

Therefore the failure envelope is represented by the parabola equation

$$\tau = \left[\frac{\sigma - \sigma_t}{a_1} \right]^{\frac{1}{2}} \text{ in the range } \sigma_t < \sigma < \left[\frac{c}{\tan \phi} + 2\sigma_t\right] \tag{71}$$

or by the straight line equation

$$\tau = \sigma \tan \phi + c \text{ in the range } [\frac{c}{\tan \phi} + 2\sigma_t] < \sigma < ? \qquad (72)$$

The value of the constants a_1 and c are obtained from equations 69 and 59. The effect of changing σ_c/σ_t on the failure envelope is shown in Figure 36. The effect of changing ϕ on the failure envelope is shown in Figure 37. Tinoco (25) used the Calderon method to determine cohesion and internal friction angle for cement-treated soils. The cohesion is obtained as the failure stress in a pure shear test. The σ_c/σ_t range for Tinoco's cement-treated soils was between 5 and 9. If a Mohr's circle for a pure shear test where $\sigma_1 = \sigma_t$ were drawn on Figure 36 it would become obvious that the shear failure stress would underpredict the cohesion and that the sample would fail by simple tension rather than by shear. Tinoco (25) observed that the failure mode in the pure shear test on cement treated soil was tensile.

Figure 38 is Figure 33 redrawn with a parabolic envelope fitting the typical values of $\phi = 40^o$, $\sigma_c/\sigma_t = 10$ conditions for concrete. It now becomes obvious that the only way a Mohr's circle with diameter $\sigma_1 - \sigma_3$ and $\sigma_1 = -\sigma_3$ can become tangent to the parabolic failure envelope is for σ_3 to equal σ_t. Therefore the point of tangency is at (o, σ_3) which is identical to (o, σ_t).

The normal stress on the failure plane at point B in Figure 30 is σ_t and the shearing stress must be zero since the Mohr's circle is tangent to the failure envelope at (o, σ_t). The mode of failure is

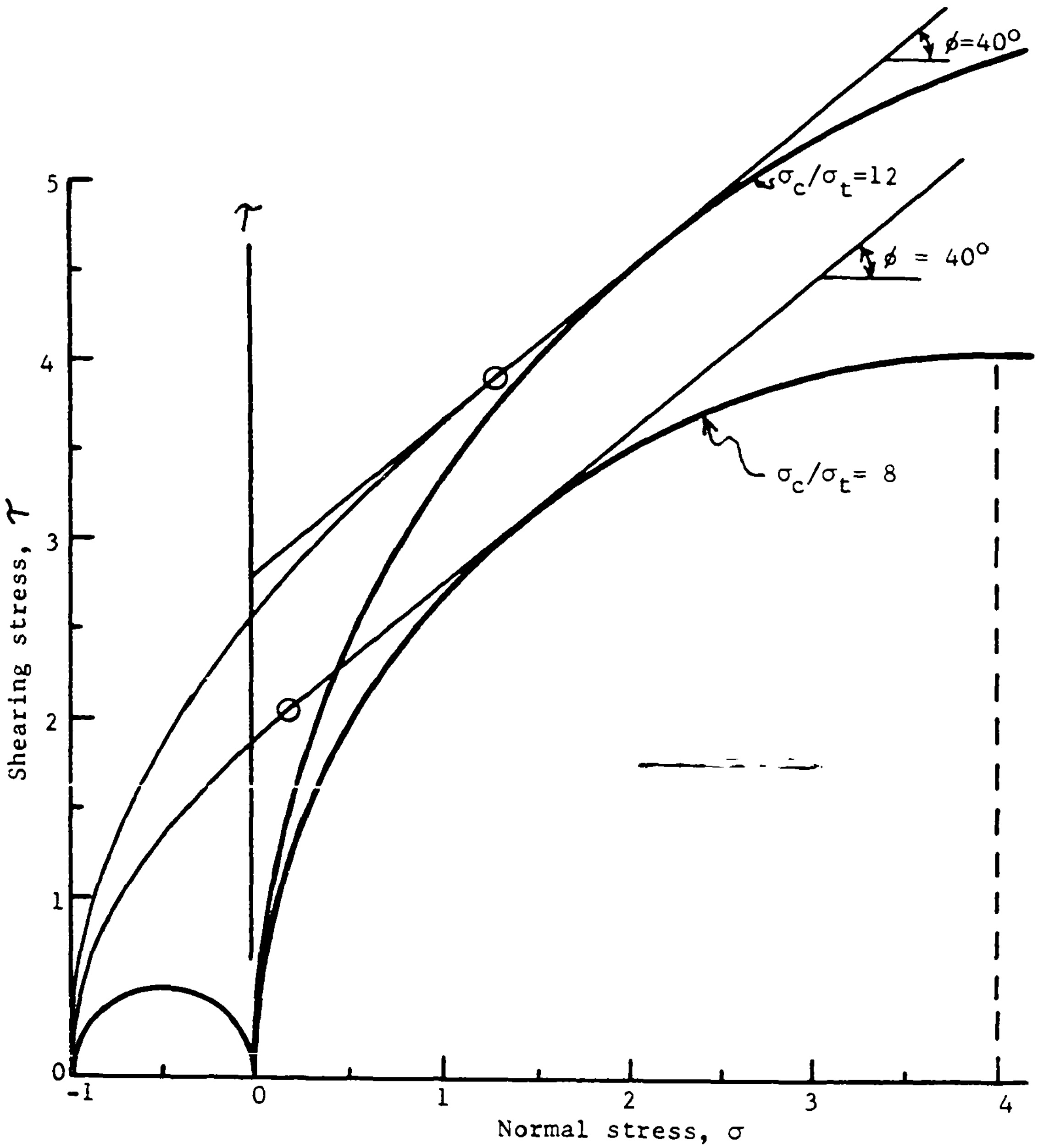

Figure 36. Failure envelopes with changing stress ratio, σ_c/σ_t, ϕ constant

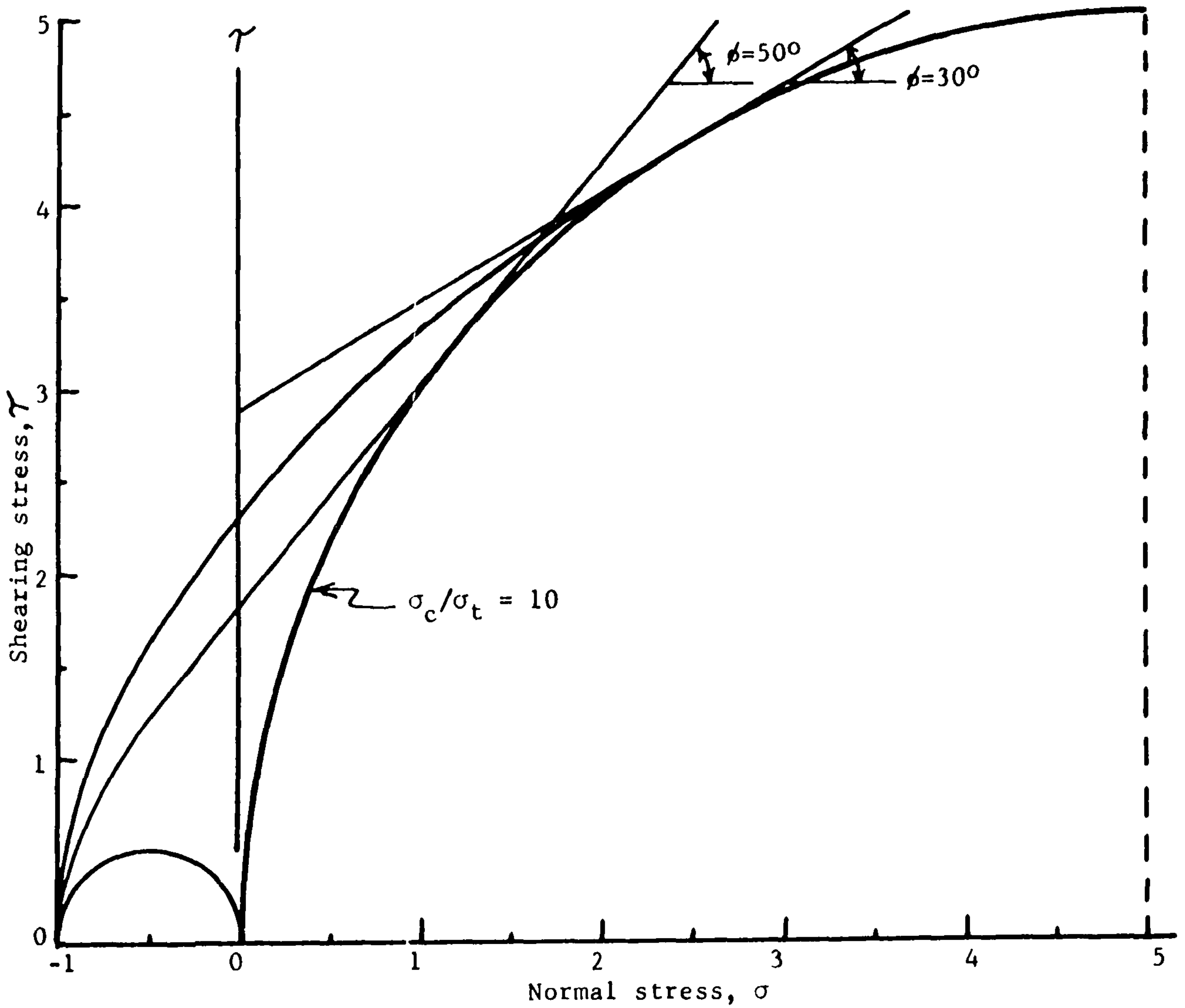

Figure 37. Failure envelopes with changing friction angle, ϕ, σ_c/σ_t constant

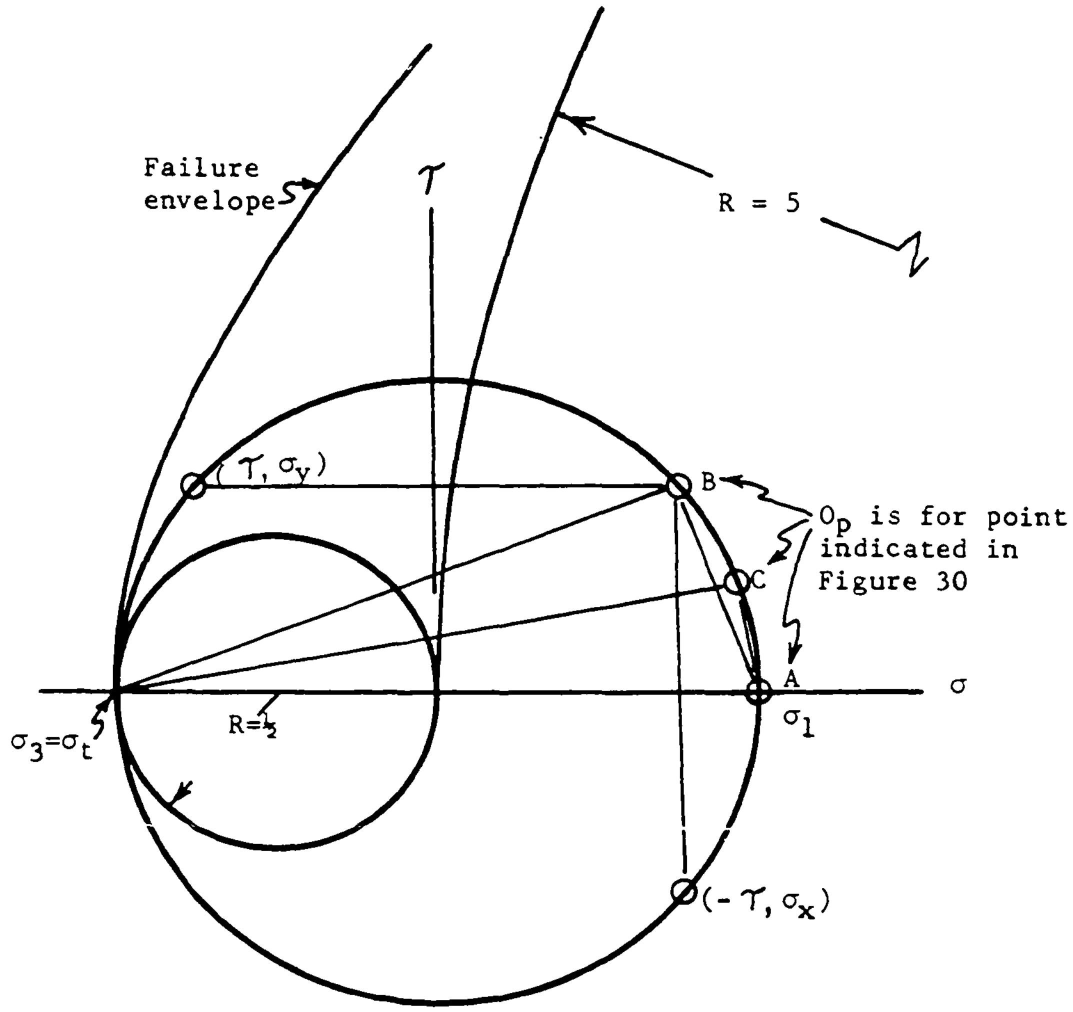

Figure 38. Mohr's circle for stresses at the aggregate-concrete interface--parabolic failure envelope

simple tension. The origin of planes, O_p is located by constructing through (o, σ_t) a line parallel to the failure plane at point B and through (o, σ_1) a line perpendicular to the failure plane at point B of Figure 30. The origin of planes is shown in Figure 38. From the origin of planes the magnitudes of τ, σ_y and σ_x could be determined, if σ_1 were known, by constructing lines on Figure 38 parallel to the planes of the stress element shown in Figure 31.

Actually it is not necessary to know σ_1, σ_y or σ_x since the stresses on the failure plane are uniquely known to be (o, σ_t) as long as $\sigma_1 \leq -\sigma_t$.

At point C in Figure 30 the stresses on the failure plane are still (o, σ_t) but the origin of planes has shifted to point C in Figure 38. At point A the stresses on the failure plane are still (o, σ_t) with the origin of planes shifted to point A in Figure 38. It is also likely that σ_1 decreases as distance from the aggregate-concrete interface increases. Since the stresses on the failure plane are independent of σ_1 as explained above, it is not necessary to know the magnitude of σ_1 to complete the analysis.

The popout pressure required to cause failure will now be derived for the simple tension case -- Model III. Since σ_t is the only stress acting on the failure plane the resisting vertical differential force can be obtained from Figure 39 as

$$d\,F_v = \sigma_t \, dA \cos\beta \tag{73}$$

where

$$dA = 2\,\pi x \frac{d_x}{\cos\beta} \quad . \tag{74}$$

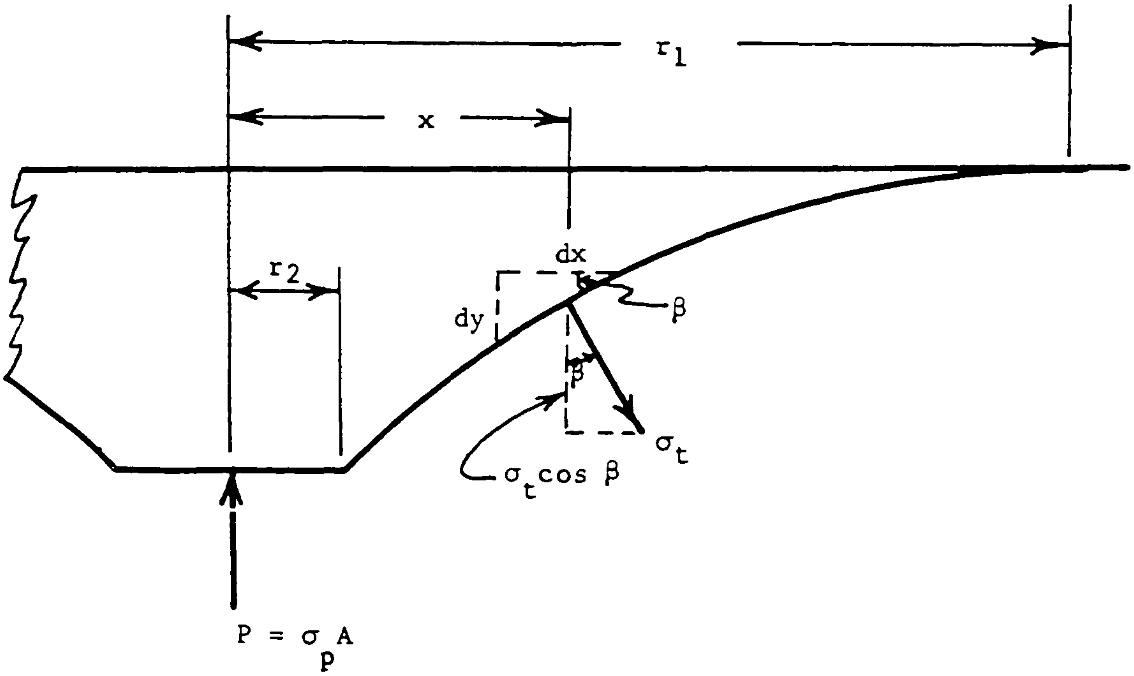

Figure 39. Stress on failure plane, Model III--Simple tension

Substituting equation 74 into equation 73

$$d\,F_v = \sigma_r[2\pi x\,d\,x] \tag{75}$$

or

$$F_v = 2\,\pi\,\sigma_t \int_{r_2}^{r_1} x\,d\,x = 2\,\pi\,\sigma_t\,\left[\,\frac{x^2}{2}\,\right]_{r2}^{r1}$$

or

$$F_v = \pi\,\sigma_t(r_1^2 - r_2^2)\;. \tag{76}$$

The activating force P is

$$P = \sigma_p A = \sigma_p\,\pi\,r_2^2\;. \tag{77}$$

A summation of forces in the vertical direction results in

$$P = F_v$$

or

$$\sigma_p\,\pi\,r_2^2 = \pi\sigma_t(r_1^2 - r_2^2) \tag{78}$$

The popout stress ratio σ_p/σ_t is

$$\frac{\sigma_p}{\sigma_t} = \frac{(r_1^2 - r_2^2)}{r_2^2} \tag{79}$$

or

$$\frac{\sigma_p}{\sigma_t} = \frac{A_e}{A_2} \tag{80}$$

where the effective resisting area, A_e is the total popout area projected on a horizontal plane minus the area of activating pressure, A_2.

Comparison of Model II and Model III

It is of interest to see how equation 79 or 80 for the simple tensile failure-Model III compares to equation 46 for Mohr-Coulomb-Model II. For the popout shown in Figure 17 equation 79 gives

$$\frac{\sigma_p}{\sigma_t} = \frac{(r_1^2 - r_2^2)}{r_2^2} = \frac{(\frac{d}{2} + \frac{H}{\tan\theta})^2 - (\frac{d}{2})^2}{(\frac{d}{2})^2}$$

or

$$\frac{\sigma_p}{\sigma_t} = \frac{(\frac{d}{2})^2 + \frac{dh}{\tan\theta} + \frac{h^2}{\tan^2\theta} - (\frac{d}{2})^2}{\frac{d^2}{4}}$$

or

$$\frac{\sigma_p}{\sigma_t} = \frac{4(\frac{h}{d})}{\tan\theta} + \frac{4(\frac{h}{d})^2}{\tan^2\theta} \quad . \tag{81}$$

Substituting equation 38 into equation 81 gives

$$\frac{\sigma_p}{\sigma_t} = \frac{4}{\tan^2(45 - \frac{\phi}{2})}(\frac{h}{d})^2 + \frac{4}{\tan(45 - \frac{\phi}{2})}(\frac{h}{d}) \tag{46}$$

which is identical to equation 46. Therefore, if in the simple tension Model III the circular failure arc emerges at the surface at the same location as the Mohr-Coulomb failure plane in Model II the popout stress ratio σ_p/σ_t predicted by both Models is identical. In simple tension-Model III the stress ratio equation is independent of the failure path as long as the path emerges on the surface at r_1.

Figures 40 and 41 illustrate the reason for prediction equations being identical for Models II and III. In Model II it was assumed that

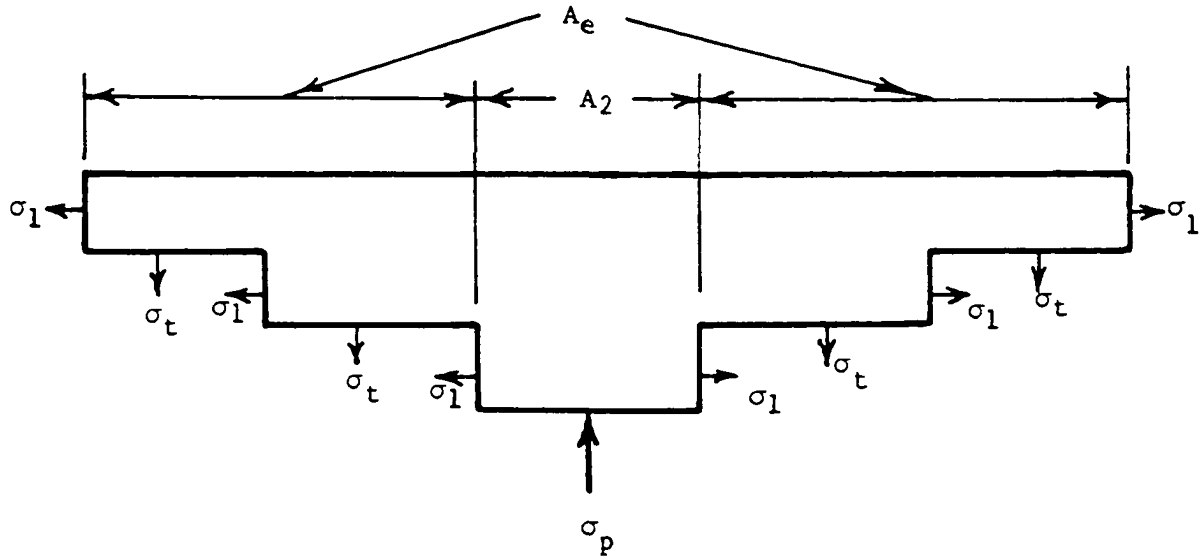

Figure 40. Step type failure plane illustrating Model II assumptions

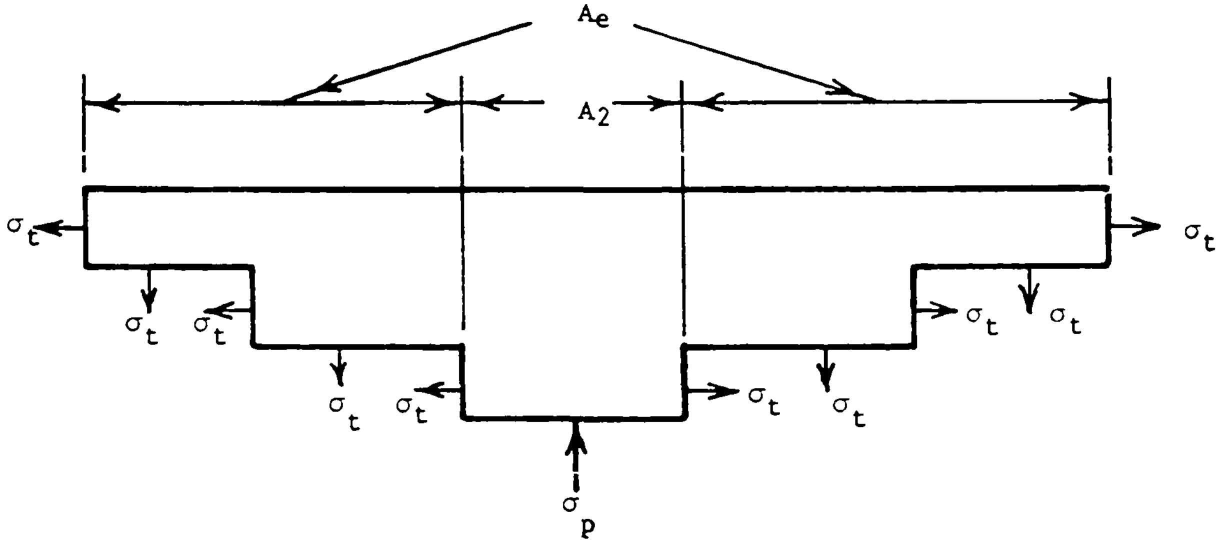

Figure 41. Step type failure plane illustrating Model III assumptions

stresses on horizontal and vertical planes were principal and that the stress on the horizontal plane was σ_t. In Model III it was assumed that stresses on the failure plane were principal and that the tensile stress was equal to σ_t. Summation of vertical forces in both cases shown in Figures 40 and 41 yields the identical results

$$\sigma_p A_2 = \sigma_t A_e$$

or

$$\frac{\sigma_p}{\sigma_t} = \frac{A_e}{A_2} \qquad (80)$$

which is identical to equation 80.

POPOUT AND SHALE DIMENSIONAL RELATIONSHIP

The shale particles causing concrete popouts have a rather large deviation from spherical shape. To determine the approximate shape of the shale, 77 particles of various sizes were examined. The results are shown in Table 15. D_1 and D_2 are the maximum and intermediate shale dimensions and T is the minimum shale dimension. D is the average of D_1 and D_2. The ratio of the average diameter to the average thickness D/T is also shown. The relationship between the shale particle diameter D, and the diameter to thickness ratio D/T is shown in Figure 42. The correlation coefficient is only 0.303 which indicates that the D/T ratio is not very dependent upon the average particle diameter, D. However Figure 42 does show that all shale particles measured deviate from a sphere with D/T ratios between about 2 and 5 with the average D/T of about 3 for the smaller particles. This would suggest that the shale particles are more nearly elliptical in shape than they are spherical. Examination of popouts indicated that the long axis of the shale particle was parallel to the surface of the concrete. Therefore a vertical section of an idealized shale particle is shown in Figure 43.

The ratio of activating compressive stress to the resisting tensile stress given by equation 49 is a function of the ratio of the popout height to the popout diameter h/d. It is of interest to see how this h/d relates to the depth of embedment H and diameter D of the shale particle causing the concrete popout.

Table 15. Shale particle dimensions[a]

D_1	D_2	Av. D	T	D/T
0.21	0.15	0.180	0.038	4.74
0.22	0.18	0.200	0.038	5.26
0.16	0.10	0.130	0.075	1.73
0.25	0.08	0.165	0.068	2.43
0.19	0.12	0.155	0.064	2.42
0.21	0.11	0.160	0.073	2.19
0.17	0.12	0.155	0.051	3.04
0.17	0.07	0.120	0.040	3.00
0.165	0.137	0.151	0.048	3.15
0.20	0.155	0.177	0.049	3.61
0.155	0.117	0.136	0.028	4.86
0.163	0.149	0.156	0.040	3.90
0.146	0.115	0.130	0.044	2.95
0.137	0.103	0.120	0.065	1.85
0.115	0.095	0.105	0.039	2.69
0.086	0.080	0.083	0.019	4.37
0.20	0.18	0.190	0.041	4.63
0.30	0.20	0.250	0.067	3.73
0.22	0.17	0.195	0.083	2.35
0.22	0.17	0.195	0.108	1.81
0.28	0.25	0.265	0.082	3.23
0.45	0.25	0.350	0.122	2.87
0.18	0.17	0.175	0.070	2.50
0.32	0.17	0.245	0.075	3.27
0.22	0.16	0.190	0.040	4.75
0.21	0.15	0.180	0.056	3.21
0.30	0.20	0.250	0.092	2.72
0.22	0.13	0.175	0.095	1.84
0.22	0.18	0.200	0.059	3.39
0.23	0.20	0.215	0.055	3.91
0.17	0.14	0.155	0.050	3.10
0.20	0.14	0.170	0.073	2.33
0.22	0.10	0.160	0.082	1.95
0.21	0.16	0.185	0.074	2.50
0.452	0.294	0.373	0.165	2.26
0.679	0.436	0.557	0.179	3.11
0.624	0.428	0.526	0.242	2.17
0.571	0.430	0.500	0.237	2.11

[a] See Figure 43.

Table 15. (Continued)

D_1	D_2	Av. D	T	D/T
0.485	0.459	0.472	0.202	2.34
0.576	0.455	0.515	0.198	2.60
0.455	0.403	0.429	0.234	1.83
0.521	0.401	0.461	0.200	2.31
0.625	0.343	0.484	0.266	1.82
0.833	0.409	0.621	0.335	1.85
0.497	0.417	0.457	0.214	2.14
0.487	0.417	0.452	0.301	1.50
0.553	0.445	0.499	0.136	3.67
0.637	0.443	0.540	0.092	5.87
0.781	0.607	0.694	0.265	2.62
0.624	0.475	0.549	0.203	2.71
0.933	0.586	0.760	0.324	2.34
1.125	0.625	0.875	0.178	4.92
0.577	0.484	0.530	0.210	2.53
0.813	0.640	0.726	0.330	2.20
0.740	0.658	0.699	0.230	3.04
0.655	0.502	0.578	0.177	3.27
0.757	0.556	0.656	0.227	2.89
0.870	0.454	0.662	0.277	2.39
0.534	0.485	0.514	0.351	1.46
0.556	0.428	0.492	0.339	1.45
1.015	0.753	0.884	0.478	1.85
1.030	0.789	0.909	0.312	2.92
0.771	0.665	0.718	0.413	1.74
1.020	0.714	0.867	0.386	2.25
0.904	0.646	0.775	0.285	2.72
1.000	0.564	0.782	0.368	2.13
0.718	0.645	0.682	0.389	1.75
0.734	0.645	0.690	0.375	1.84
0.687	0.645	0.666	0.288	2.31
1.437	0.728	1.082	0.559	1.94
1.30	1.13	1.215	0.50	2.43
1.30	0.80	1.050	0.51	2.06
1.25	0.73	0.990	0.45	2.20
1.15	0.66	0.905	0.53	1.71
1.40	1.00	1.200	0.57	2.11
1.45	0.75	1.100	0.36	3.05
1.20	0.73	0.965	0.53	1.82

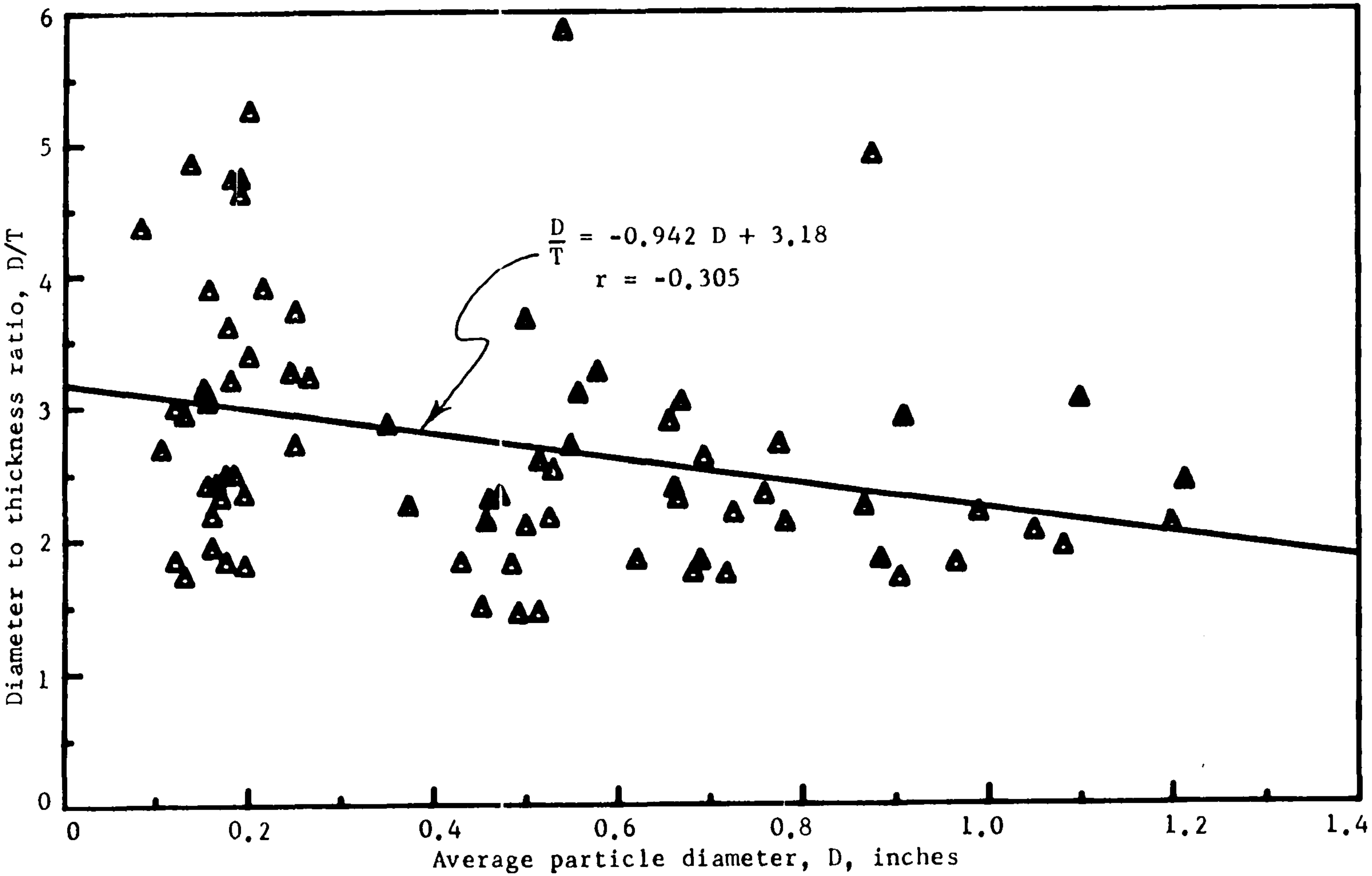

Figure 42. Relationship between shale particle thickness, T, and particle diameter, D

A first assumption was that the h/d for the popout particle would be the same as the H/D for the shale particle. This assumption requires the base of the popout particle to be coincident with the center of the shale particle.

A second assumption was that there is a plane above the center of the shale particle where the h/d is less than the H/D for the shale particle. Examination of several popout particles indicated that there was always less shale in the popout itself than there was in the underlying concrete. Examination of equations 46 and 49 shows that for a given concrete tensile strength σ_t and friction angle ϕ the compressive stress required to cause a popout will decrease as the h/d decreases. Therefore, the plane with the lowest h/d will be the critical plane and the one on which fracture occurs. The validity of this second assumption can be shown by determining if the ratio h/d has a minimum in the interval C to H as shown in Figure 43.

The equation of an ellipse with major axis a and minor axis b is:

$$x^2/a^2 + y^2/b^2 = 1 \ . \tag{82}$$

In the terminology shown in Figure 43 this becomes:

$$\tfrac{1}{2}\ d^2/\tfrac{1}{2}\ D^2 + y^2/\tfrac{1}{2}\ T^2 = 1 \ . \tag{83}$$

Rearranging:

$$y^2 = T^2/4\ (1 - d^2/D^2) \ . \tag{84}$$

From Figure 43:

$$h = H - y = H - \tfrac{1}{2}T(1 - d^2/D^2)^{\frac{1}{2}}$$

or

$$h = H - T/2D\ (D^2 - d^2)^{\frac{1}{2}} \ . \tag{85}$$

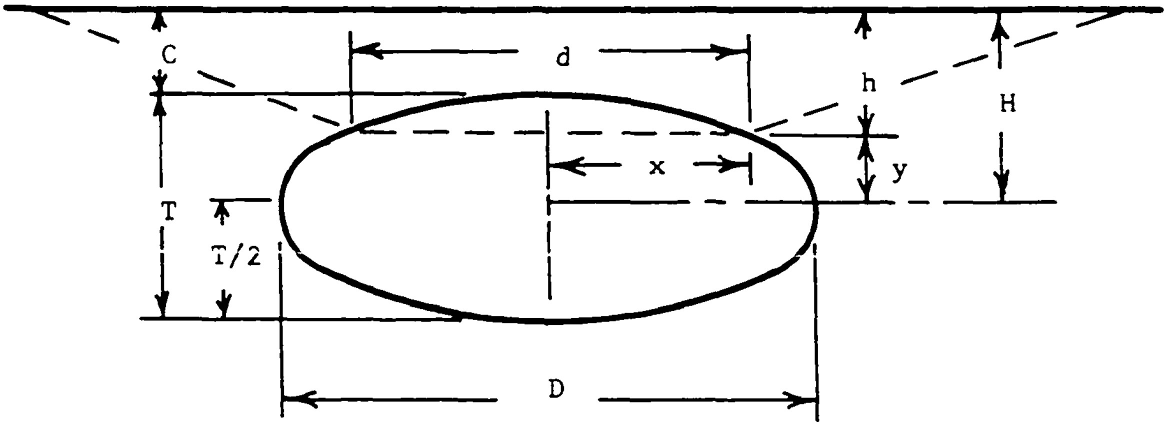

Figure 43. Idealized vertical section of a shale particle

Dividing by d:

$$\frac{h}{d} = d^{-1}[H - \frac{T}{2D}(D^2 - d^2)^{\frac{1}{2}}]$$

$$f(d) = d^{-1}[H - \frac{T}{2D}(D^2 - d^2)^{\frac{1}{2}}] \ . \qquad (86)$$

Taking the first derivative:

$$f'(d) = -d^{-2}[H - \frac{T}{2D}(D^2 - d)^{\frac{1}{2}}] + d^{-1}[(\frac{-T}{4D})(\frac{-2d}{(D^2-d^2)^{\frac{1}{2}}})] \ . \qquad (87)$$

Rearranging:

$$f'(d) = \frac{1}{d^2}[-H + \frac{T}{2D}(D^2-d^2)^{\frac{1}{2}} + \frac{d^2T}{2D(D^2-d^2)^{\frac{1}{2}}}] \ . \qquad (88)$$

For $H > T/2$ as $d \rightarrow 0$ then $f'(d) \rightarrow -\infty$

and as $d \rightarrow D$ then $f'(d) \rightarrow +\infty$.

Therefore $f'(d) = 0$ for $d \neq 0$ or D will be determined to obtain the minimum (or maximum) value for h/d:

$$0 = -H + \frac{T}{2D}(D^2-d^2)^{\frac{1}{2}} + \frac{d^2T}{2D(D^2-d^2)^{\frac{1}{2}}}$$

or

$$0 = -H(D^2-d^2)^{\frac{1}{2}} + \frac{T}{2D}(D^2-d^2) + \frac{d^2T}{2D}$$

or

$$H(D^2-d^2)^{\frac{1}{2}} = \frac{T}{2D}(D^2-d^2) + \frac{d^2T}{2D} \ . \qquad (89)$$

Squaring both sides:

$$H^2(D^2-d^2) = \frac{T^2}{4D^2}(D^2-d^2)^2 + \frac{2\ d^2T^2}{4\ D^2}(D^2-d^2) + \frac{d^4T^2}{4D^2}$$

or

$$H^2(D^2-d^2) = \frac{T^2D^4}{4D^2} - \frac{2T^2d^2D^2}{4D^2} + \frac{T^2d^4}{4D^2} + \frac{2d^2T^2D^2}{4D^2} - \frac{2T^2d^4}{4D^2} + \frac{d^4T^2}{4D^2} \qquad (90)$$

Collecting terms:

$$H^2(D^2-d^2) = \frac{T^2D^2}{4} \quad . \tag{91}$$

Rearranging:

$$d^2H^2 = H^2D^2 - \frac{T^2D^2}{4}$$

or

$$d^2 = D^2 - \frac{T^2D^2}{4H^2}$$

or

$$d^2 = \frac{D^2}{4H^2}(4H^2-T^2) \quad . \tag{92}$$

Taking the square root of both sides of equation 92:

$$d = \frac{D}{2H}(4H^2 - T^2)^{\frac{1}{2}} \quad . \tag{93}$$

Equation 93 is the value for d where h/d is either a minimum or a maximum.

$$\text{As } d \rightarrow 0 \quad f(d) = h/d \rightarrow \infty$$

$$\text{and} \quad \text{as } d \rightarrow D \quad f(d) = h/d \rightarrow H/D \ .$$

Substituting equations 92 and 93 into equation 86:

$$\frac{h}{d} = \frac{H}{\frac{D}{2H}(4H^2-T^2)^{\frac{1}{2}}}\left[H - \frac{T}{2D}\left(D^2-D^2+\frac{D^2T^2}{4H^2}\right)^{\frac{1}{2}}\right]$$

$$\frac{h}{d} = \frac{H}{\frac{D}{2}(4H^2-T^2)^{\frac{1}{2}}}\left[H - \frac{T}{2D}\left(\frac{DT}{2H}\right)\right]$$

$$\frac{h}{d} = \frac{(4H^2-T^2)^{\frac{1}{2}}}{2D} \quad . \tag{94}$$

Since $T > 0$ then $(4H^2 - T^2)^{\frac{1}{2}} < 2H$ and $h/d < H/D$.

Therefore h/d is a minimum at the d given by equation 93. This minimum h/d would be associated with the failure plane since the least compressive stress required to cause a popout occurs at the lowest h/d value.

Equation 94 can be written in terms of dimensionless ratios by dividing the numerator and denominator by $(4D^2)^{\frac{1}{2}}$.

$$\frac{h}{d} = \left(\frac{4H^2}{4D^2} - \frac{T^2}{4D^2}\right)^{\frac{1}{2}}$$

or

$$\frac{h}{d} = \left[\left(\frac{H}{D}\right)^2 - \frac{1}{4\left(\frac{D}{T}\right)^2}\right]^{\frac{1}{2}} . \qquad (95)$$

The relationship between the popout h/d and the shale H/D for various shale shapes D/T as given by equation 95 is plotted in Figure 44. The line with a slope of 1.0 would represent a shale particle of zero thickness or infinite D/T ratio. In this limiting case the popout h/d would equal the shale H/D. The other limiting case would be a sphere with a D/T of 1. In this case there is a rather significant difference between the popout h/d and the shale H/D. A spherical shale particle embedded such that the H/D was 0.5 would have a minimum h/d of zero since the upper tangent to the shale particle would be coincident with the concrete surface.

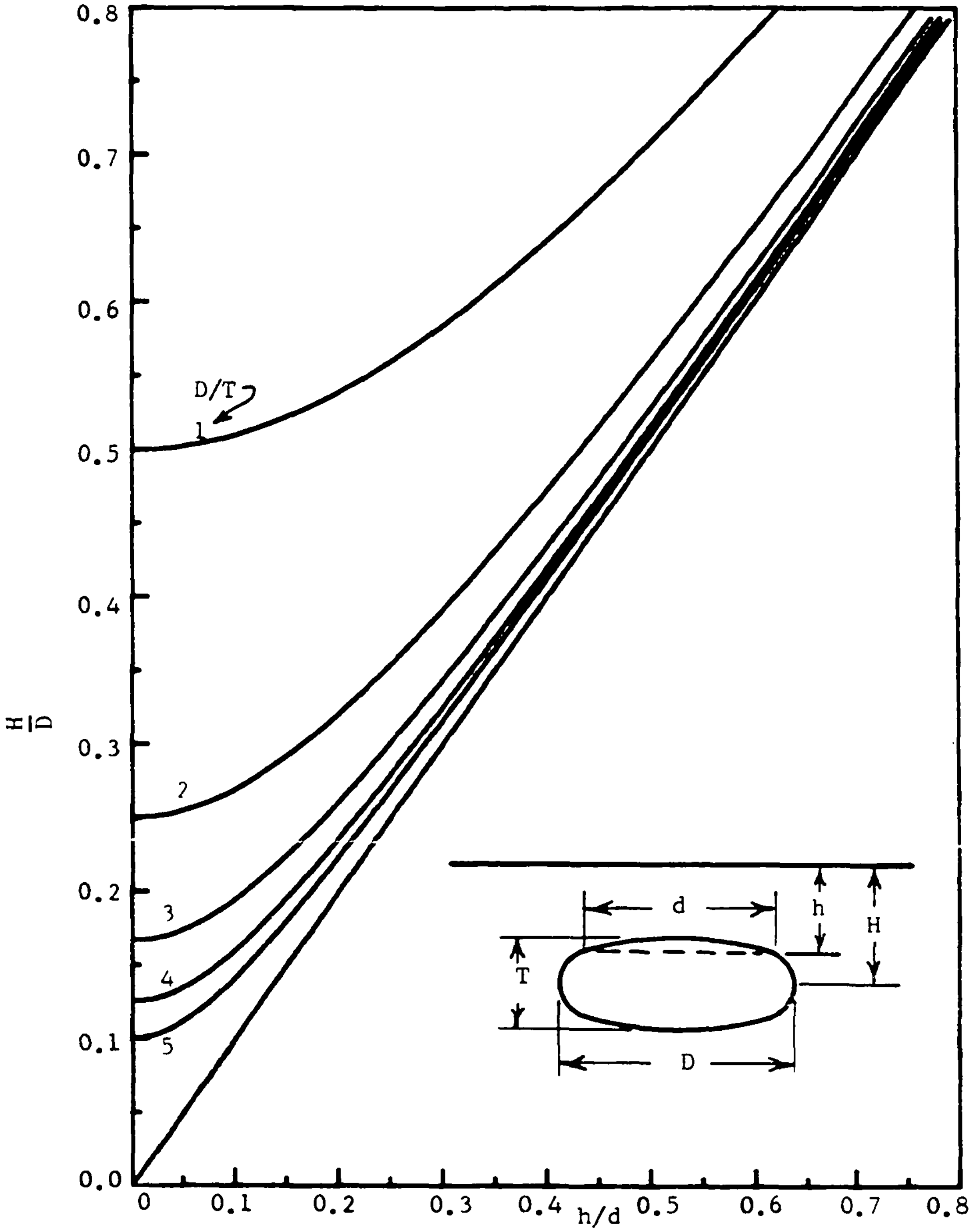

Figure 44. Relationship between shale center depth-diameter ratio H/D to popout depth-diameter ratio h/d for various values of shale diameter-thickness ratios D/T

EXPERIMENTAL MODELS

Materials

Mechanically induced popouts were created in hydrated plaster of Paris and portland cement. These materials were selected in preference to concrete since the presence of aggregate located in a potential popout failure surface would most certainly alter that surface.

Specimen Preparation

Specimens for popouts were prepared in 2-in. by 2-in. cube molds with a 1/8" rod extending vertically through the specimen to within a set distance from the bottom of the specimen. These distances were 0.025 in. for a height to diameter ratio, h/d of 0.2; 0.062 in. for a height to diameter ratio, h/d of 0.5; and 0.096 in. for a height to diameter ratio of 0.77. The rod had an elliptical end to simulate the shape of shale particles. Four different water-cement, W/C ratios were used for each h/d ratio. These W/C ratios were: 0.27, 0.35, 0.43, and 0.50.

For each popout specimen three compressive strength specimens and three tensile strength specimens were cast from the same batch. The compressive strength specimens were cylinders 2-in. in diameter and 5 in. high. The tensile strength specimens were cast in briquette type molds described in ASTM C190 Tensile Strength of Hydraulic-Cement Mortars.

The plaster of Paris specimens were cured in air at 23 ± 3°C and tested at age 5 days. The portland cement specimens were cured one day in the mold and 14 days in lime-saturated water at 19 ± 2°C and tested at age 15 days. Care was taken such that all portland cement specimens remained saturated until time of test to minimize shrinkage cracks. In all cases the surface was still wet at the time of test. All compression specimens were cast on a machined plate such that it was only necessary to cap the top of the specimen with a sand-sulphur mixture.

Test Procedures

Popouts were artificially induced in the following manner: The 1/8-in. rod was extracted from the hardened specimen, a small piece of plastic modelling clay was placed on the elliptical end of the rod and it was re-inserted into the specimen. The clay was used to simulate the hydrostatic pressures exerted by an expanding alkali-silica gel. The 2-in. by 2-in. cubic specimen was supported at the four corners by a tube of brass, and assembly was placed in a motorized press. The loading rate was 0.10 inches per minute, and the force on the 1/8-inch rod required to cause a popout was measured by a proving ring.

The compression specimens were tested in a 60,000 lb universal testing machine at a loading rate of 35 psi/sec.

The tensile specimens were tested in a machine specifically designed to test briquettes cast in accordance with ASTM C190.

Testing Program

The variables tested were:

Materials:	Portland Cement, Plaster of Paris			
h/d:	0.20	0.50	0.77	
W/C:	0.27	0.35	0.43	0.50

The total number of specimens cast and tested was 72, consisting of 24 each for popout specimens, compression specimens and tensile specimens. This provided only one popout specimen for each combination of the above variables. However, three compression and three tension specimens were obtained at each water-cement ratio.

RESULTS AND ANALYSIS

Popout Tensile and Compressive Stresses

The results of the testing program are shown in Table 16. Compressive and tensile strength tests were made to obtain a value for the friction angle ϕ assuming a linear failure envelope. The failure envelope tangent to the Mohr's circles representing stress conditions of unconfined compressive strength, σ_c and tensile strength, σ_t is shown in Figure 45. The friction angle, ϕ is obtained in terms of σ_c and σ_t as follows:

$$\sin \phi = \frac{\frac{\sigma_t}{2}}{\frac{\sigma_t}{2} + x} = \frac{\frac{\sigma_c}{2}}{\frac{\sigma_c}{2} + \sigma_t + x} \quad . \qquad (96)$$

Rearranging equation 96 gives

$$\frac{\sigma_t \sigma_c}{2} + \sigma_t^2 + \sigma_t x = \frac{\sigma_c \sigma_t}{2} + \sigma_c\, x$$

or

$$x(\sigma_c - \sigma_t) = \sigma_t^2$$

or

$$x = \frac{\sigma_t^2}{\sigma_t(\frac{\sigma_c}{\sigma_t} - 1)}$$

or

$$x = \frac{\sigma_t}{(\frac{\sigma_c}{\sigma_t} - 1)} \quad . \qquad (97)$$

Substituting equation 97 into equation 96

Table 16. Popout, tensile, and compressive stresses[a]

Specimen	$\frac{W}{C}$	$\frac{h}{d}$	σ_p (psi)	σ_t[b] (psi)	σ_c[b] (psi)	$\frac{\sigma_p}{\sigma_t}$	A_e (in^2)	$\frac{A_e}{A_2}$
				Portland Cement				
C27-1	0.27	0.20	1930			2.34	0.0762	6.2
C27-2	0.27	0.50	2660	823	8773	3.23	0.395	32.2
C27-3	0.27	0.77	4020			4.88	0.613	50.3
C35-1	0.35	0.20	810			1.15	0.0407	3.3
C35-2	0.35	0.50	1670	708	7875	2.36	0.200	16.3
C35-3	0.35	0.77	1610			2.28	0.281	23.0
C43-1	0.43	0.20	915			1.47	0.0566	4.62
C43-2	0.43	0.50	1250	624	6720	2.00	0.1187	9.7
C43-3	0.43	0.77	1830			2.93	0.202	16.5
C50-1	0.50	0.20					0.0616	5.0
C50-2	0.50	0.50	940	493	5780	1.91	0.1177	9.6
C50-3	0.50	0.77	1300			2.64	0.1917	15.6
				Plaster of Paris				
P27-1	0.27	0.20	1440			1.79	0.0423	3.45
P27-2	0.27	0.50	3000	803	5610	3.73	0.163	13.3
P27-3	0.27	0.77	5610			6.99	0.326	21.4
P35-1	0.35	0.20	1175			1.54	0.1147	9.35
P35-2	0.35	0.50	1880	764	4580	2.46	0.280	22.8
P35-3	0.35	0.77	2880			3.77	0.550	45.0
P43-1	0.43	0.20	1045			1.70	0.1067	8.7
P43-2	0.43	0.50	1570	614	3940	2.56	0.258	21.0
P43-3	0.43	0.77	2480			4.04	0.406	33.1
P50-1	0.50	0.20	915			2.04	0.1097	8.95
P50-2	0.50	0.50	1520	448	2430	3.40	0.1487	12.1
P50-3	0.50	0.77	2220			4.91	0.306	25.0

[a] Legend: $\frac{W}{C}$ = water-cement ratio; $\frac{h}{d}$ = popout height to diameter ratio; σ_p = popout pressure (determined experimentally); σ_t = tensile strength; σ_c = compressive strength; A_e = popout effective resisting area = total popout area projected on a horizontal plane minus the area of activating pressure, A_2; A_2 = area of activating pressure = area of 1/8 in. shaft used to induce popouts.

[b] Average of three tests.

$$\sin \phi = \frac{\frac{\sigma_t}{2}}{\frac{\sigma_t}{2} + \frac{\sigma_t}{(\frac{\sigma_c}{\sigma_t} - 1)}} = \frac{1}{1 + \frac{2}{(\frac{\sigma_c}{\sigma_t} - 1)}} = \frac{\frac{\sigma_c}{\sigma_t} - 1}{\frac{\sigma_c}{\sigma_t} - 1 + 2}$$

or

$$\sin \phi = \frac{\frac{\sigma_c}{\sigma_t} - 1}{\frac{\sigma_c}{\sigma_t} + 1} . \tag{98}$$

Malhotra and Zoldners (23) indicated that the ratio for concrete compressive-tensile strength ranges from about 7 to 13. The ϕ and θ for various values of $\frac{\sigma_c}{\sigma_t}$ as determined by equations 98 and 38 are shown in Table 17. The failure angle, θ, is for Model II--Mohr-Coulomb failure theory.

Table 17. Relationship of friction angle, ϕ, to compressive-tensile strength ratio, σ_c/σ_t, and Model II failure angle, θ

$\frac{\sigma_c}{\sigma_t}$	ϕ	θ
7	48.59	20.70
8	51.06	19.47
9	53.13	18.43
10	54.90	17.55
11	56.44	16.78
12	57.80	16.10
13	59.00	15.50

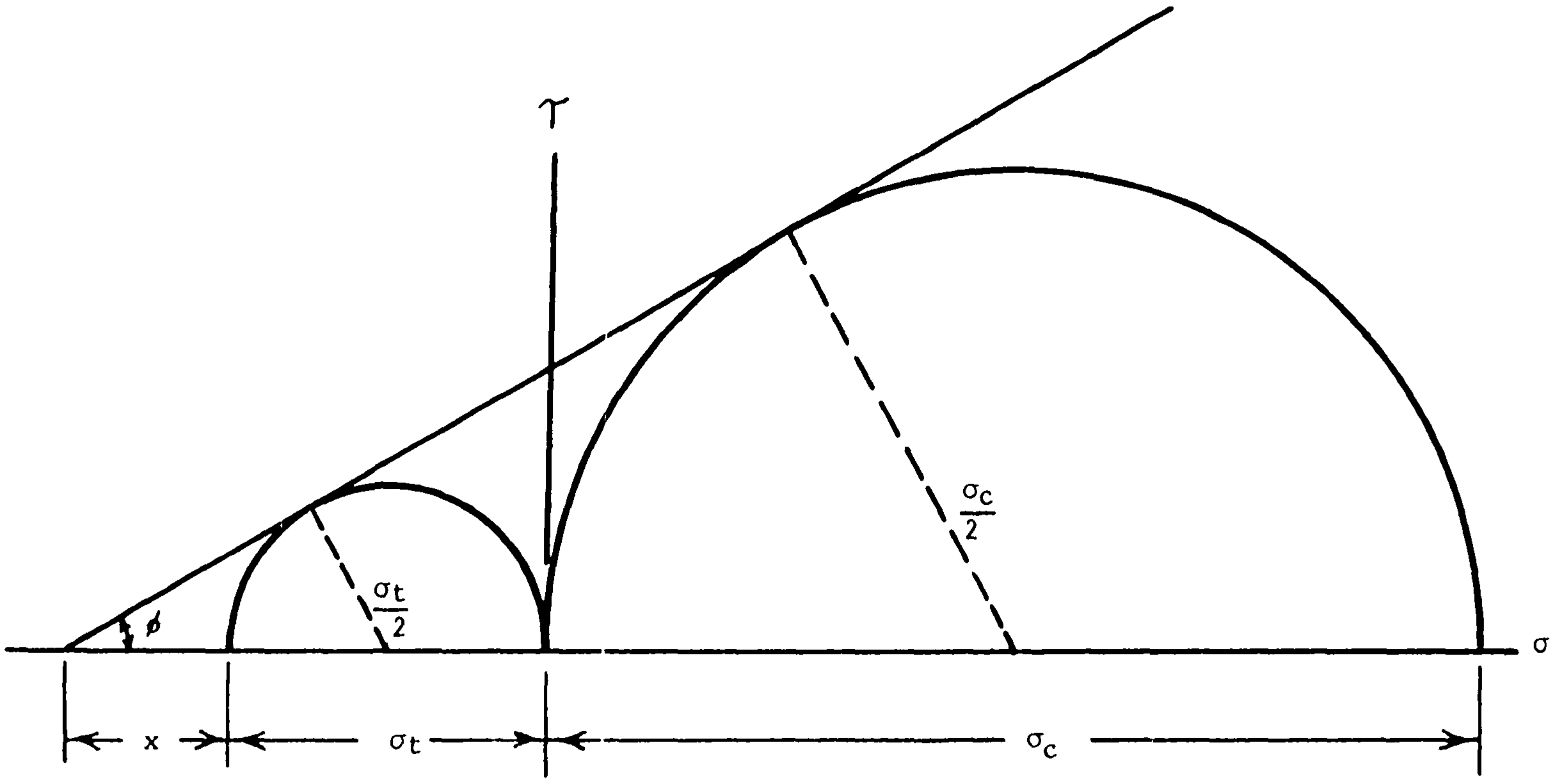

Figure 45. Friction angle based on unconfined compression and tension tests

The ratio of compressive to tensile strength calculated from Table 16 is shown in Table 18 with the accompanying ϕ and θ values.

Table 18. Experimental compressive-tensile strength ratios, $\frac{\sigma_c}{\sigma_t}$

Specimen		$\frac{\sigma_c}{\sigma_t}$	ϕ	θ
C27		10.66	55.9	17.0
C35		11.12	56.6	16.7
C43		10.77	56.1	17.0
C50		11.72	57.4	16.3
	Av.	11.04	56.6	16.7
P27		6.99	48.6	20.7
P35		5.99	45.6	22.2
P43		6.42	46.9	21.5
P50		5.42	43.5	23.2
	Av.	6.20	46.2	21.9

The compressive-tensile strength ratio shown in Table 18 is quite constant and independent of the water-cement ratio.

Graphs relating compressive strength to water-cement ratio are shown for portland cement in Figure 46 and for plaster of Paris in Figure 47. The relationship is linear in the range of water-cement ratios investigated with correlation coefficients of 0.94 for both materials.

Graphs relating tensile strength to water-cement ratio are shown for portland cement in Figure 48 and for plaster of Paris in Figure 49. The

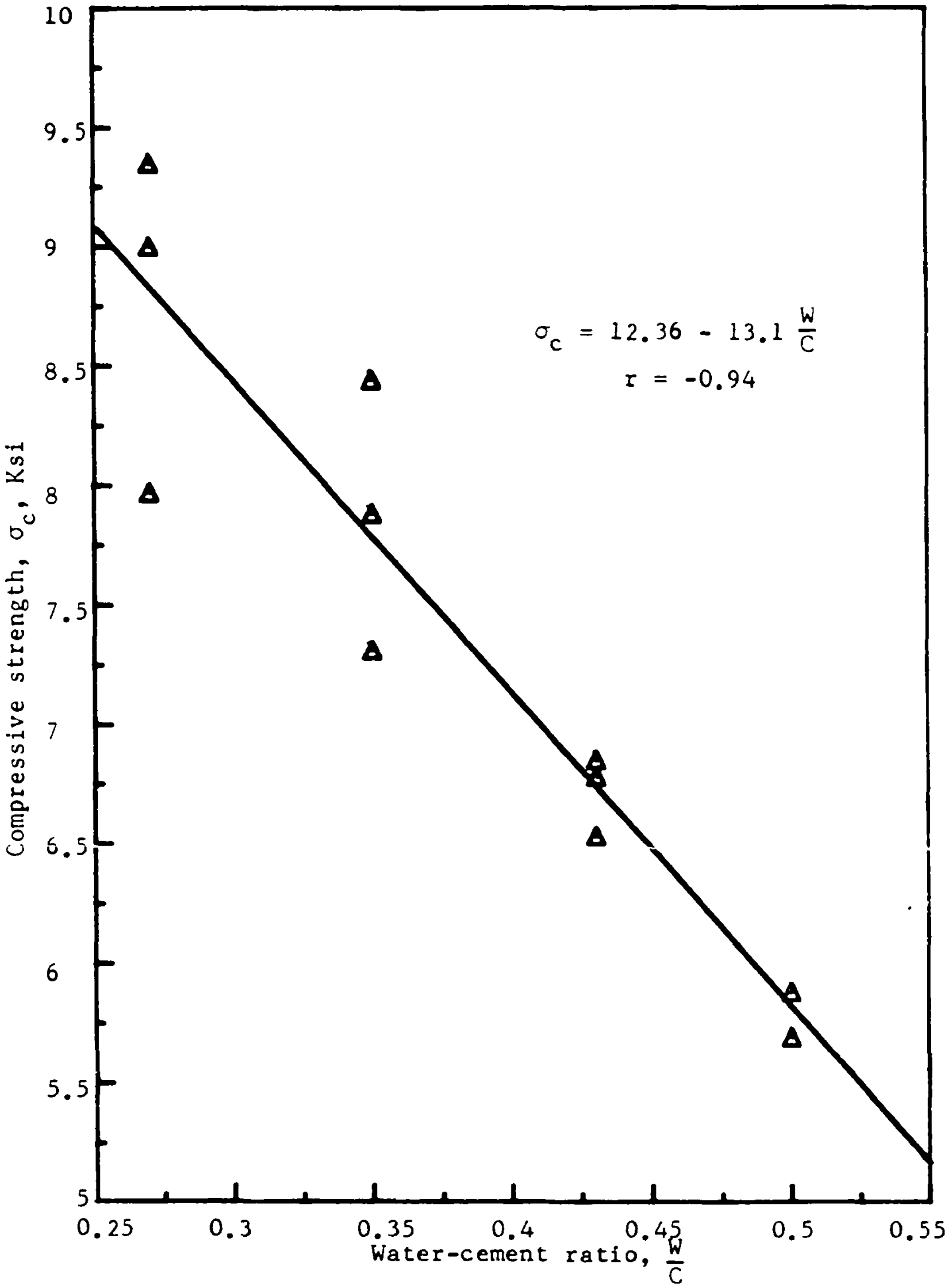

Figure 46. Compressive strength of portland cement

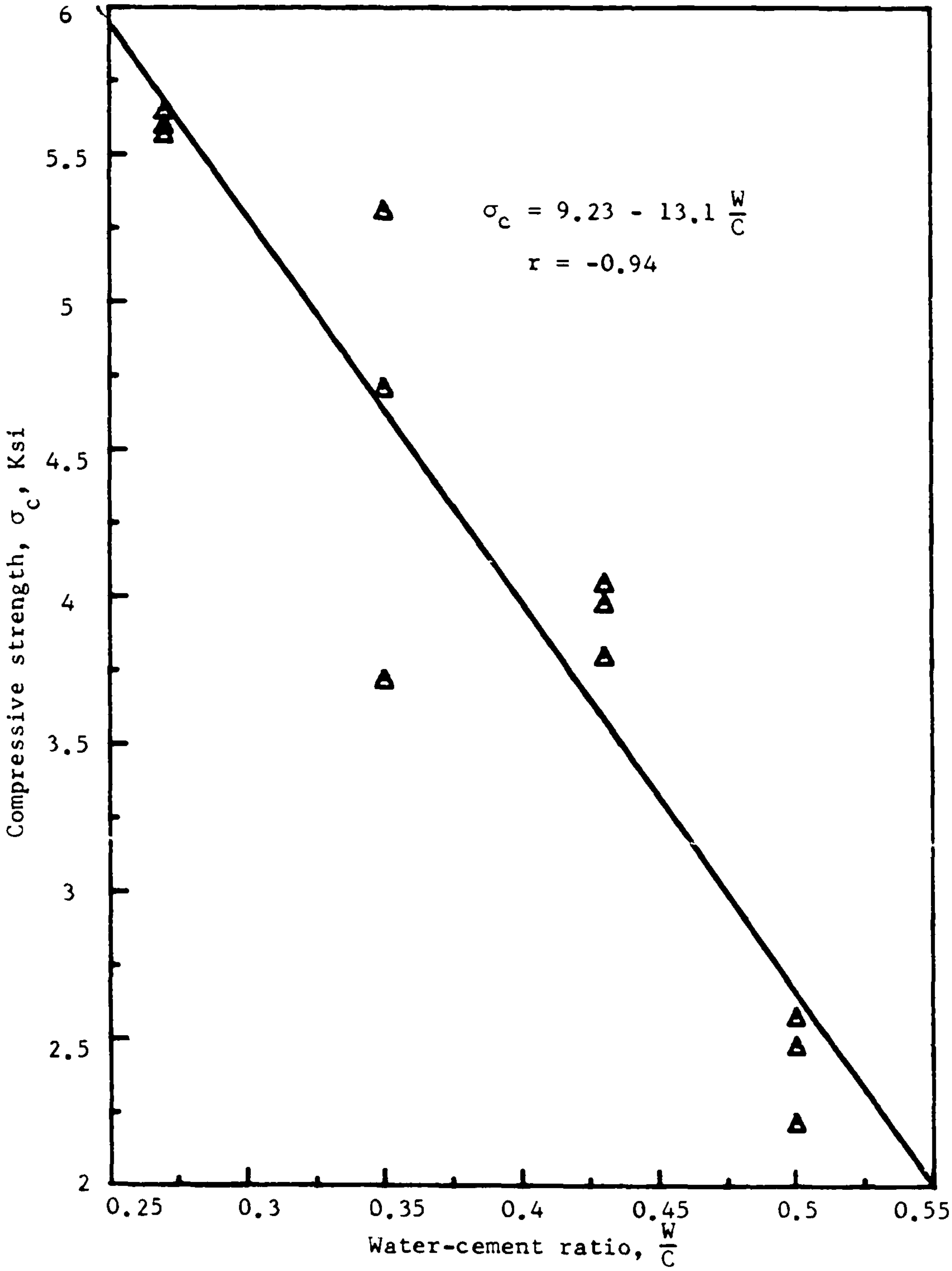

Figure 47. Compressive strength of plaster of Paris

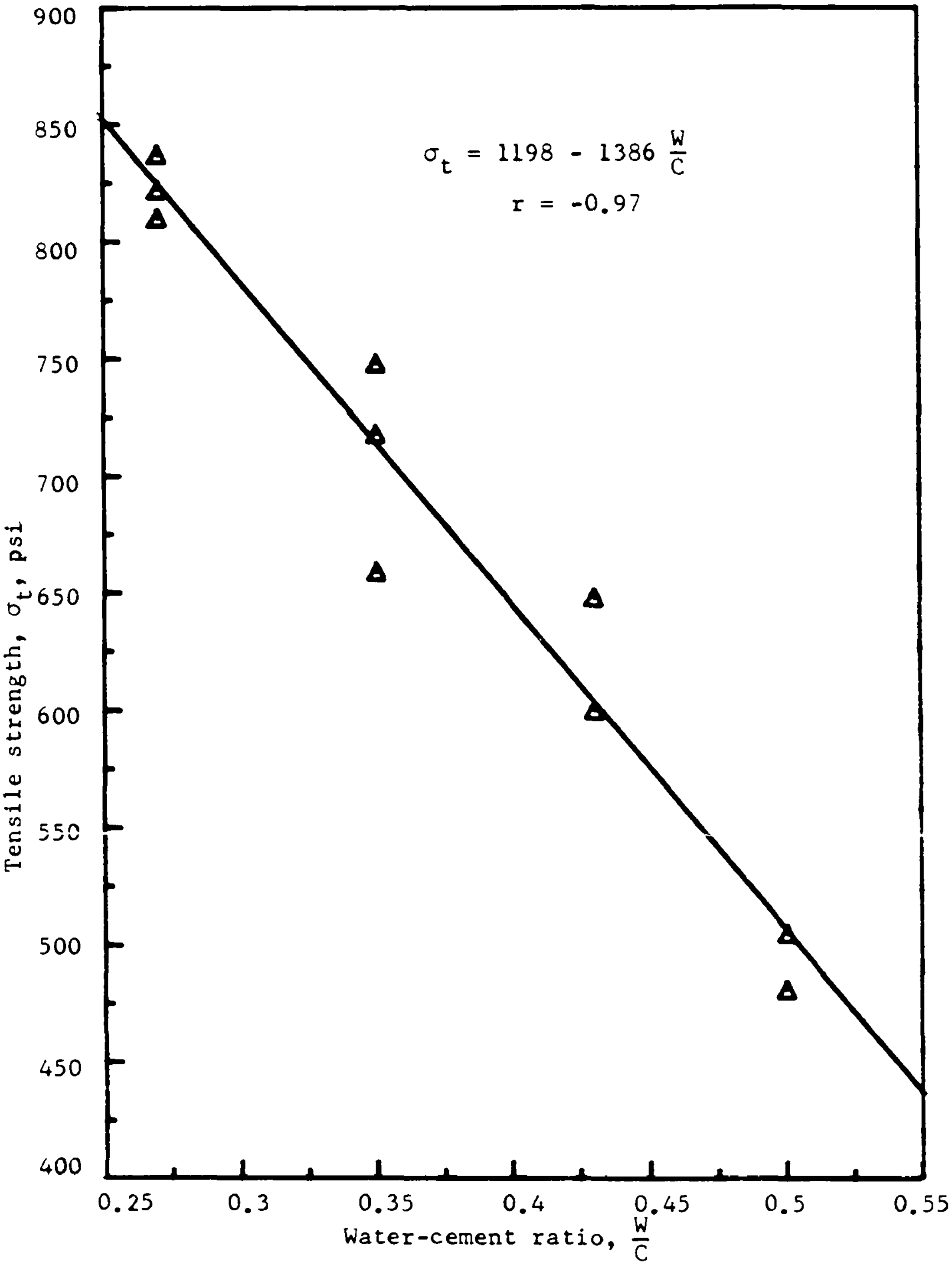

Figure 48. Tensile strength of portland cement

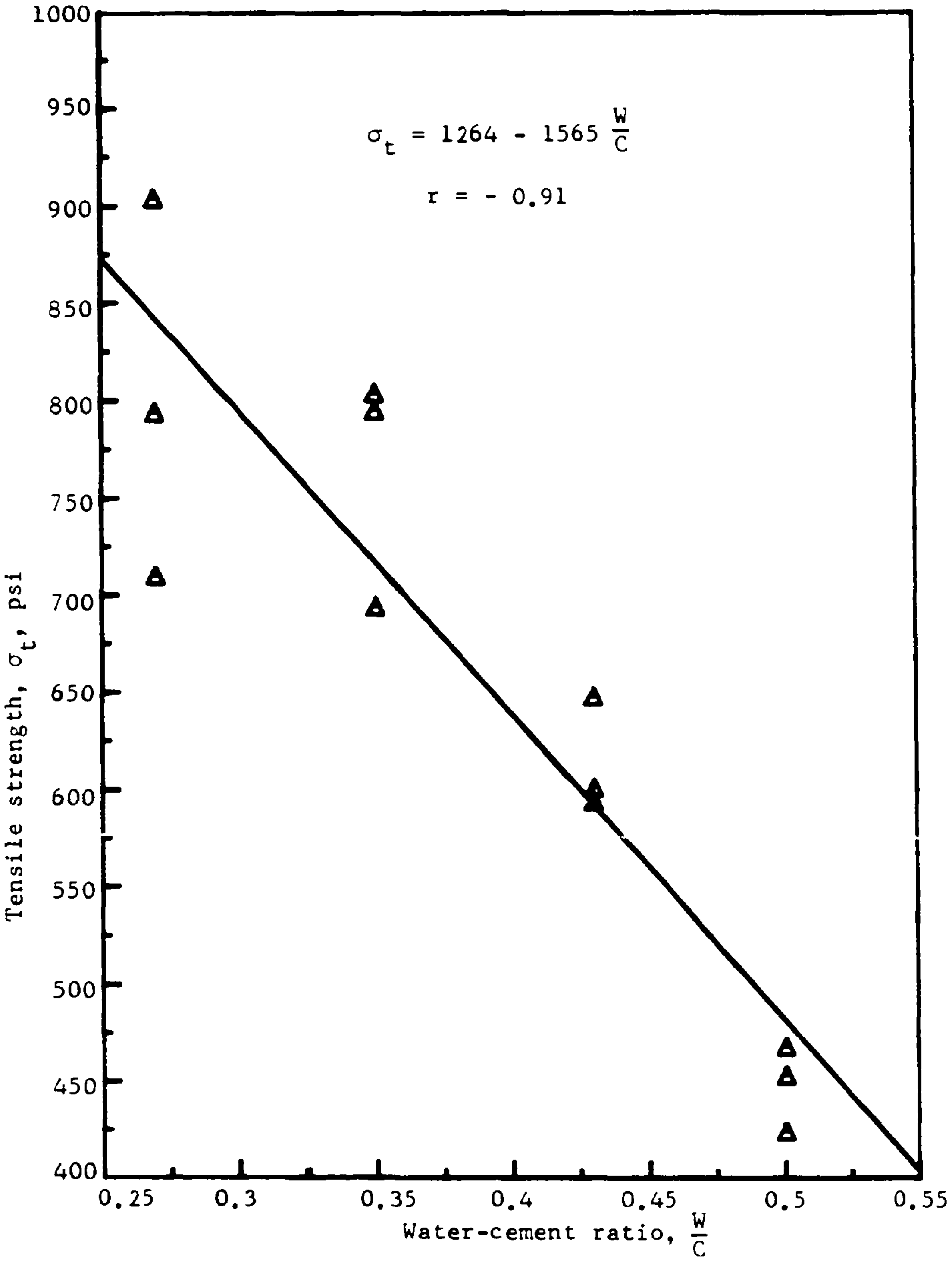

Figure 49. Tensile strength of plaster of Paris

relationship is again linear with a correlation coefficient of 0.97 for portland cement and 0.91 for plaster of Paris.

Popout Area

Two in. x 2 in. lantern slides of the popout areas were made by photographing each specimen surface after the popout was removed. Sketches of these popout areas were made and are shown in Figure 50 for portland cement and Figure 51 for plaster of Paris. The height-diameter ratio, h/d as defined in Figure 17 is the thickness of the popout divided by the diameter of the activating pressure cell. Generally, as the water-cement, W/C ratio decreased the popout area increased for a given height-diameter, h/d ratio. Also, as the height-diameter ratio, h/d increased the popout area increased for a given water-cement ratio, W/C.

The 2 in. x 2 in. slides were projected to a known enlargement scale, the periphery of each popout was traced, and its area determined by use of a planimeter. The effective area, A_e, was determined by subtracting from the total area the area of the 1/8 inch rod, A_2 used to induce the popout. The magnitude of the effective area, A_e, and the area ratio, A_e/A_2, are shown in Table 16.

The effective popout areas for portland cement are plotted in Figure 52 and for plaster of Paris in Figure 53. The linear regression lines are shown in the Figures. The correlation coefficients were 0.99 for all relationships shown in Figures 52 and 53 except for the 0.50 water-cement ratio curve in Figure 53, which had a correlation coefficient of 0.93.

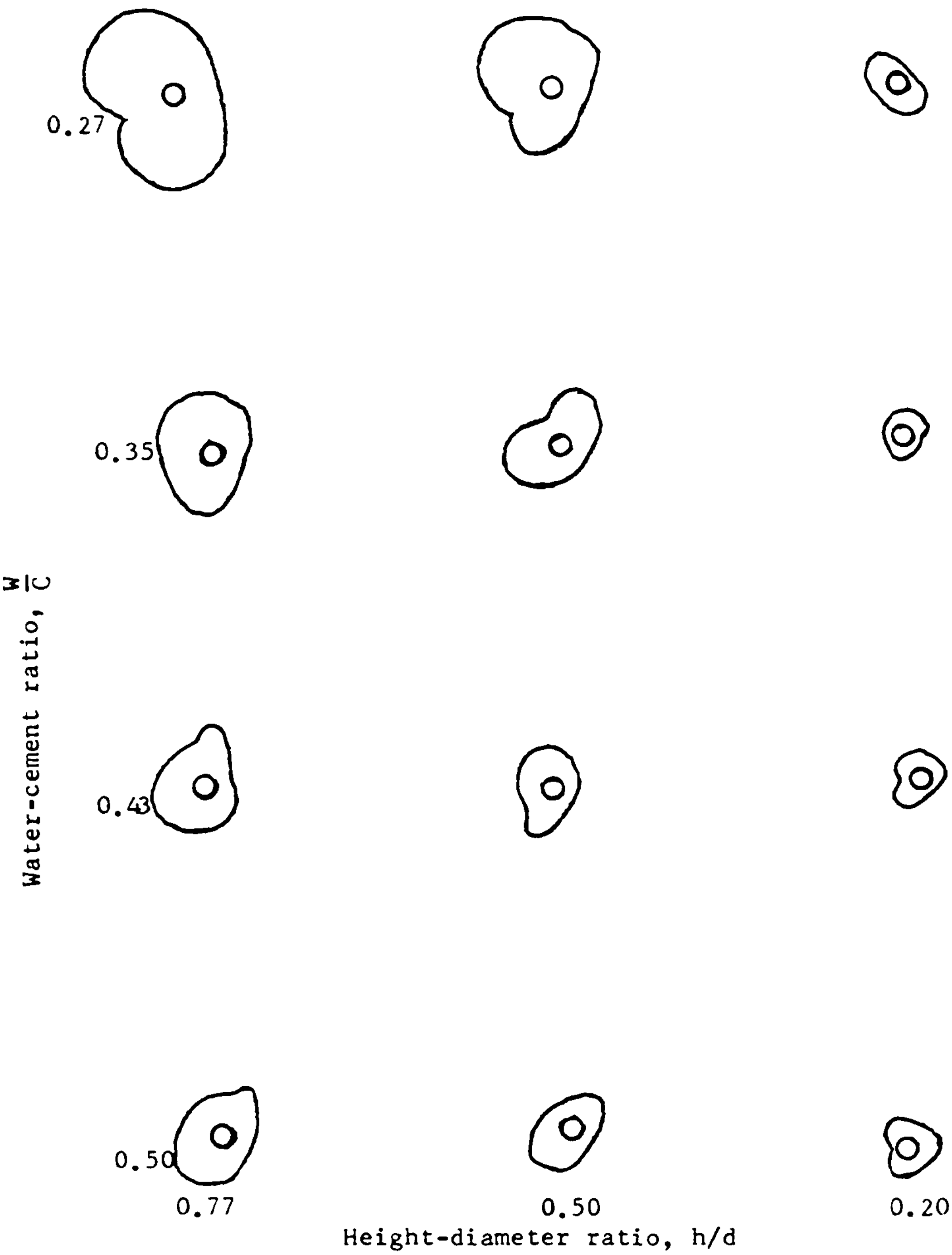

Figure 50. Portland cement popout area as related to water-cement ratio and height-diameter ratio

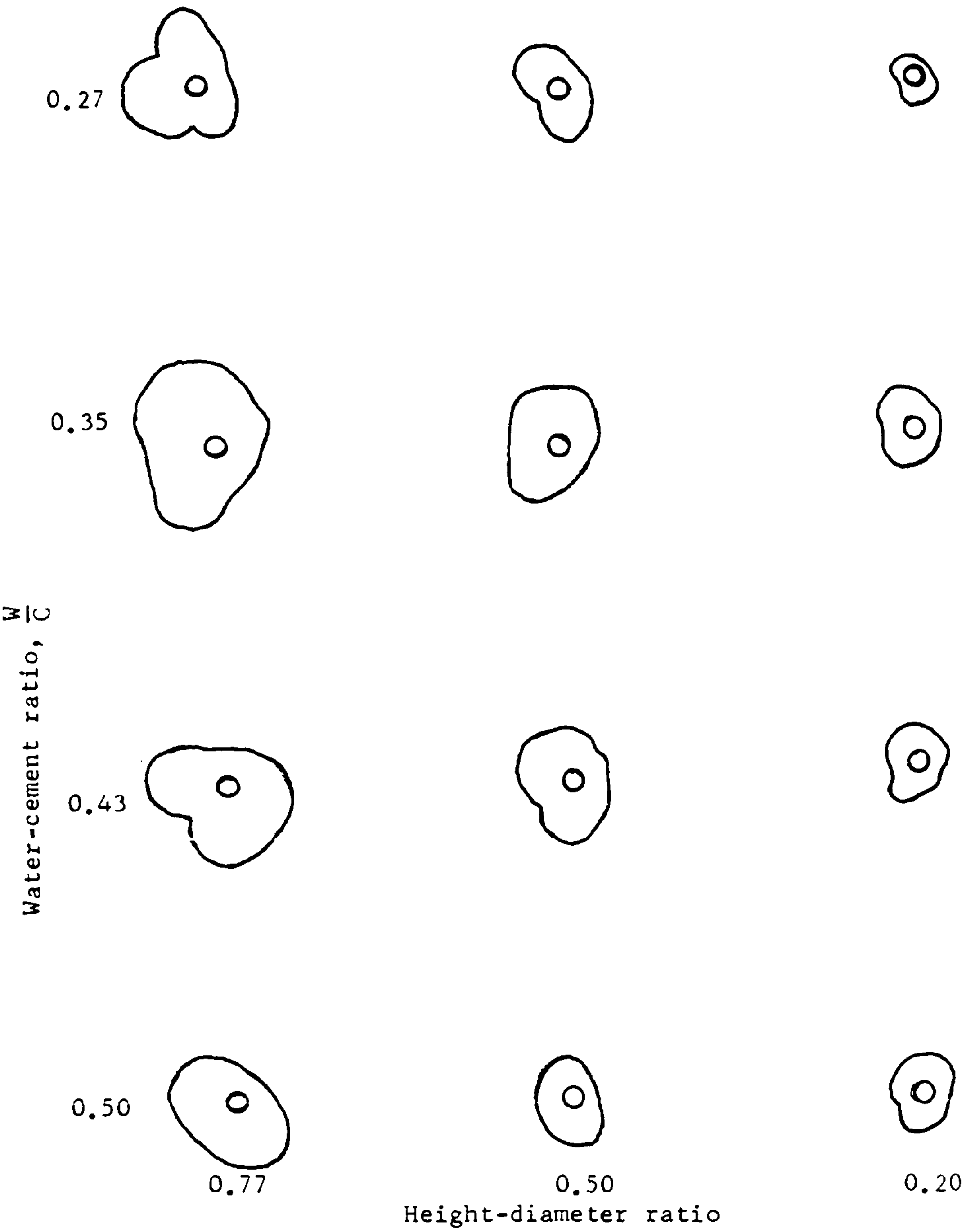

Figure 51. Plaster of Paris popout area as related to water-cement ratio and height-diameter ratio

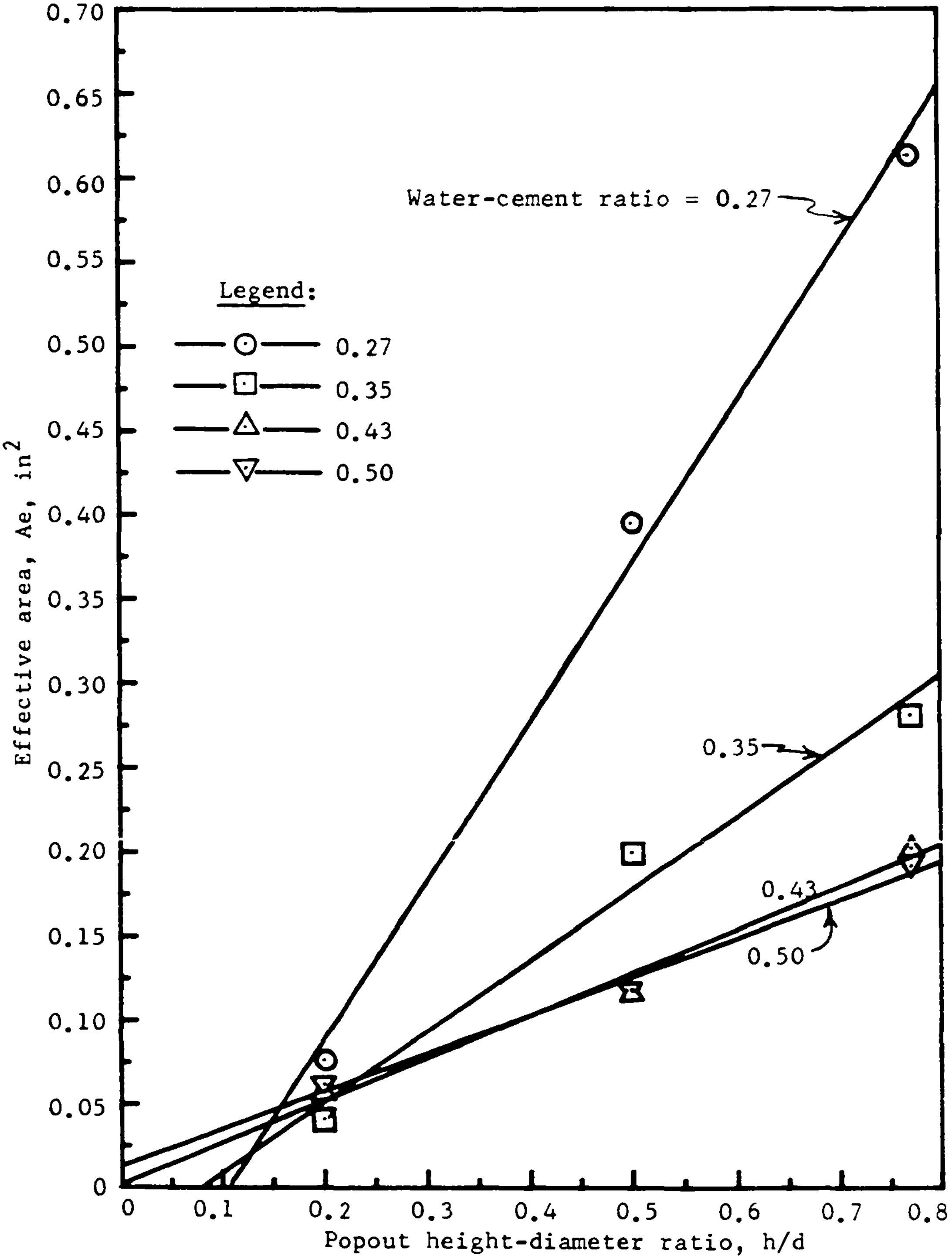

Figure 52. Effective popout area for portland cement

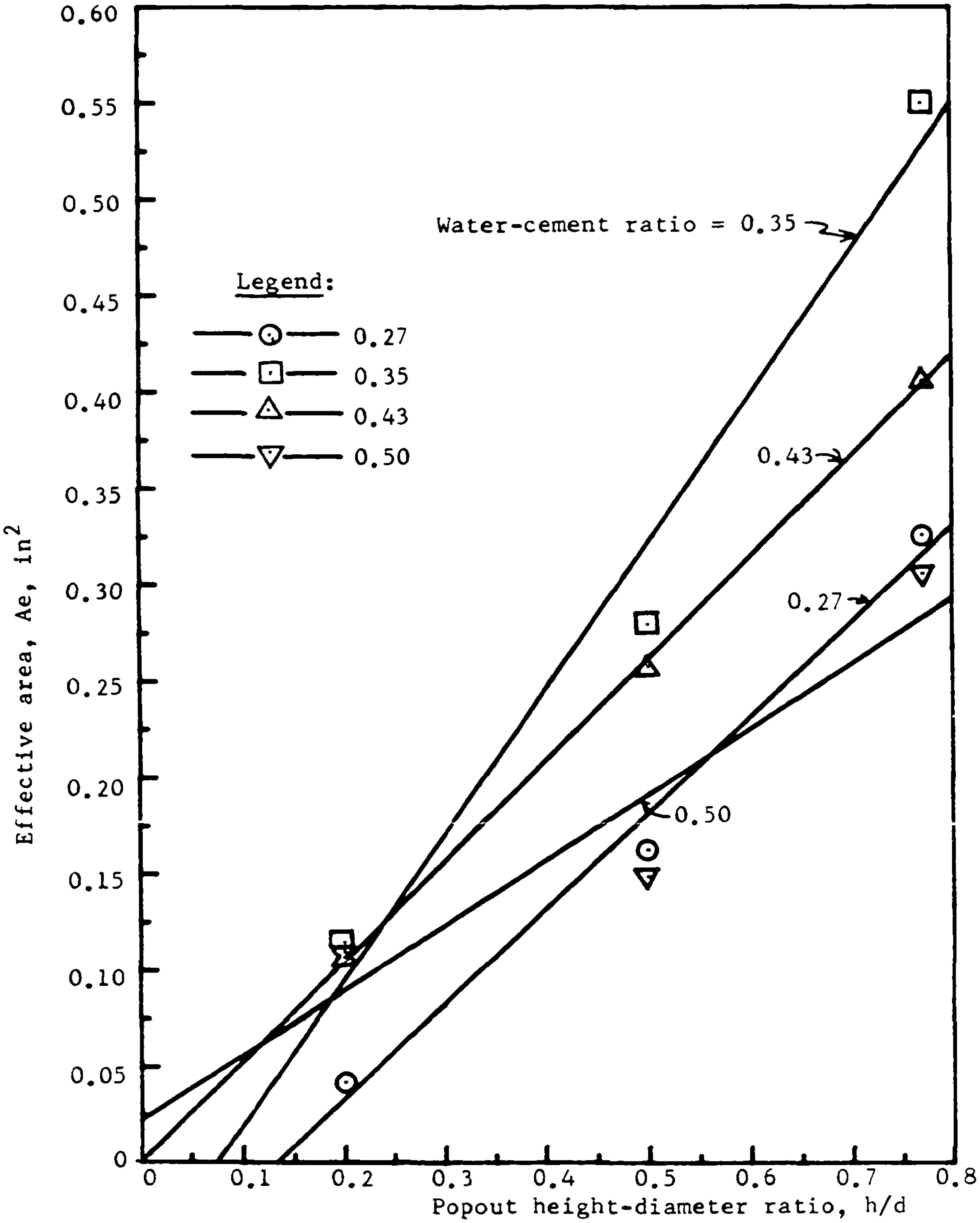

Figure 53. Effective popout area for plaster of Paris

Popout Pressure-Tensile Strength Ratio

The theoretical equations developed earlier express the popout-tensile strength ratio, $\frac{\sigma_p}{\sigma_t}$, as a function of h/d and ϕ. Since the friction angle, ϕ, was determined to be independent of water-cement ratio, W/C as shown in Table 18 it seemed adivsable to see if $\frac{\sigma_p}{\sigma_t}$ were also independent of the water-cement ratio. Plots of $\frac{\sigma_p}{\sigma_t}$ versus W/C for portland cement and plaster of Paris are shown in Figures 54 and 55. The values for the correlation coefficient, r, and test for slope significance, t, are shown in the figures. The correlation coefficients are all quite low. The "t" values listed on Figures 54 and 55 indicate significance of the slopes of the best fit lines. For any line having a "t" value smaller than $t_{\alpha,n-2}$, the slope is not significantly different than zero at the selected significance level α, and the degrees of freedom n-2. The tests for slope significance show that the slope is not significant at the 90 percent level for all tests except the 0.50 W/C portland cement specimen which had a $t_{90,2} > 2.92$.

Based upon the above analysis, $\frac{\sigma_p}{\sigma_t}$ values at all W/C ratios are used in plotting the following figures.

Observed Portland cement popout area ratios $\frac{A_e}{A_2}$ are plotted as a function of h/d in Figure 56. The area ratios for plaster of Paris are shown in Figure 57. These experimental values are compared with theoretical values predicted by equation 46 for Model II and Model III. The best fit parabola was drawn for each set of data. By coincidence the best fit

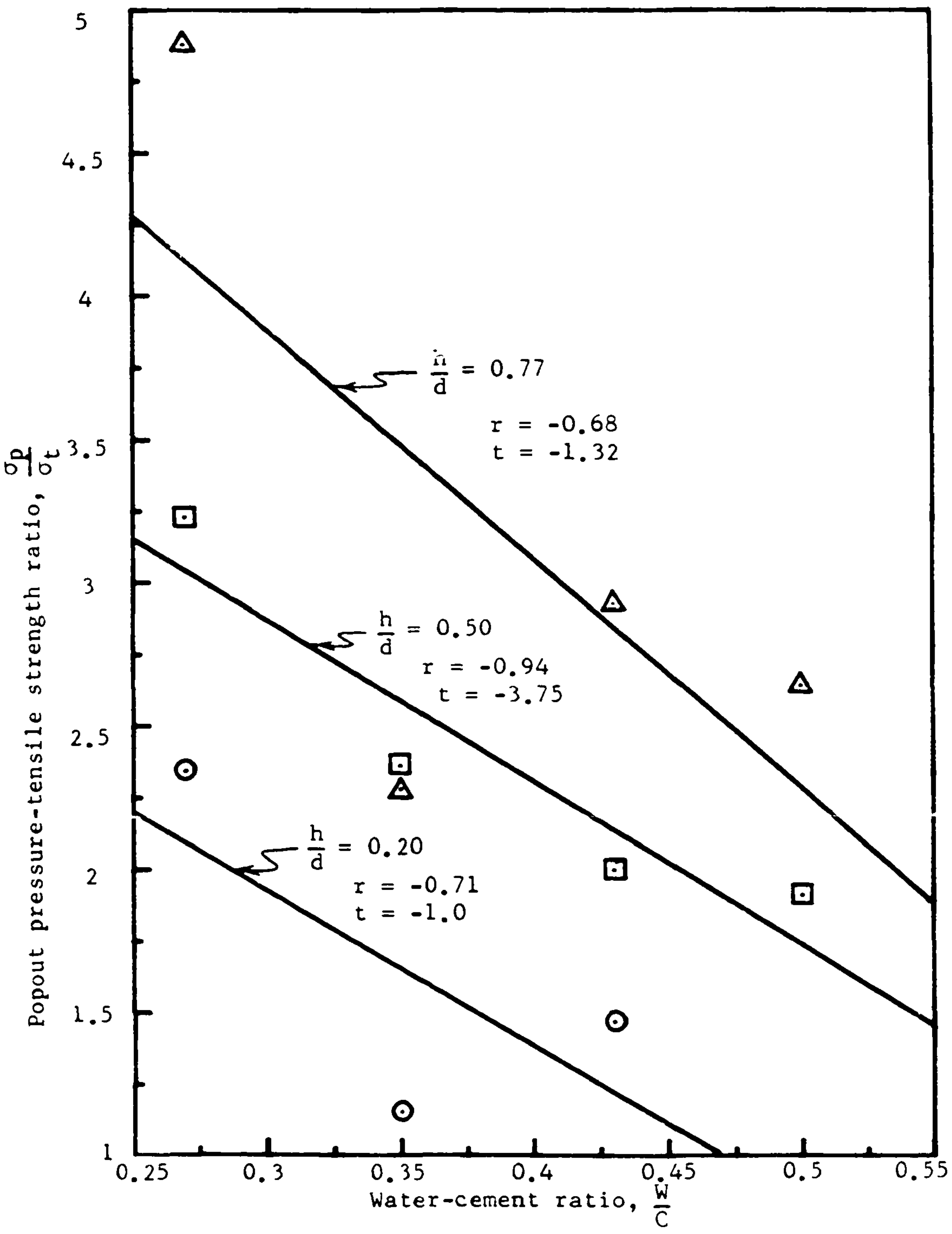

Figure 54. Effect of water-cement ratio on popout stress ratio for portland cement

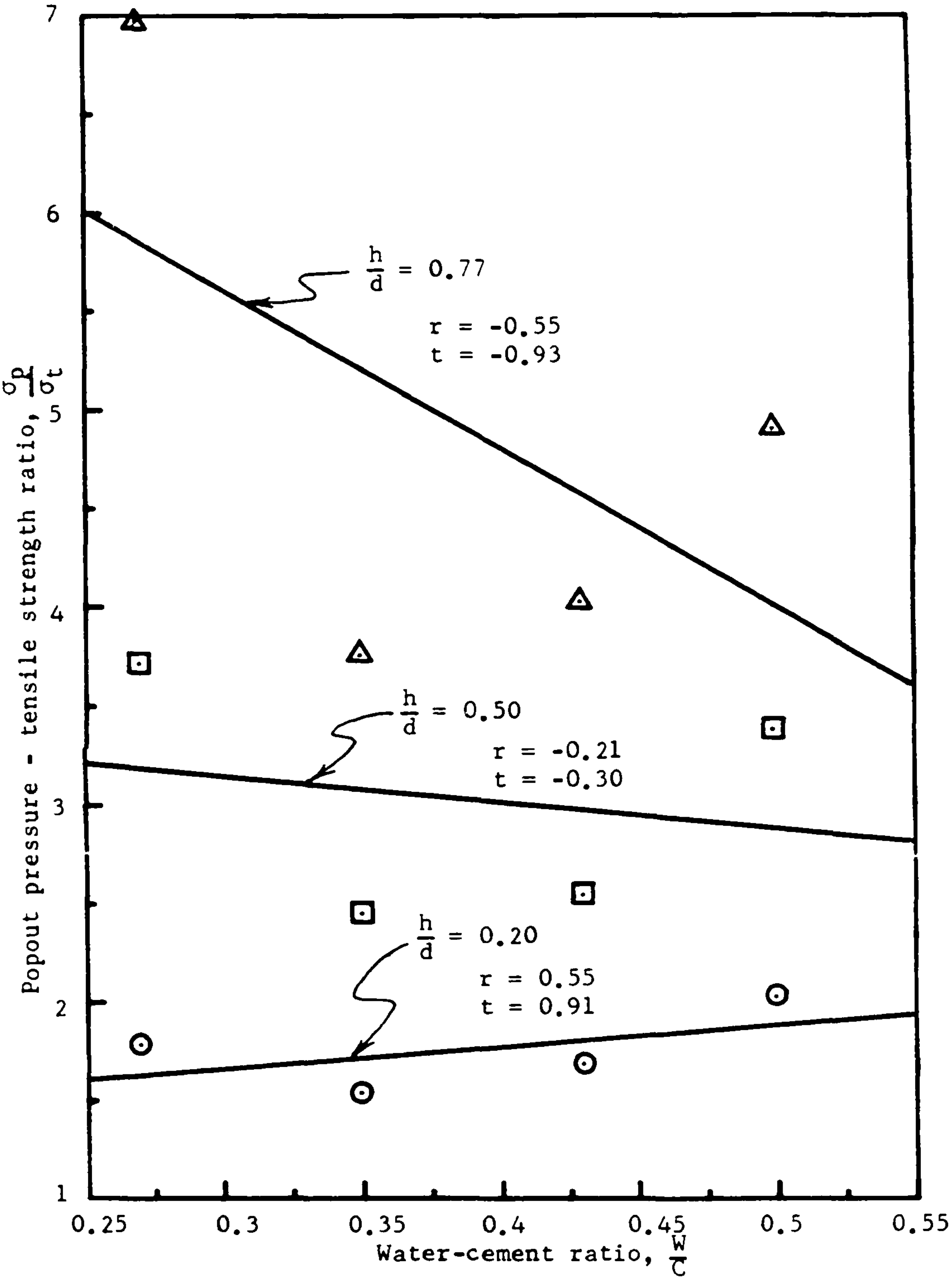

Figure 55. Effect of water-cement ratio on popout stress ratio for plaster of Paris

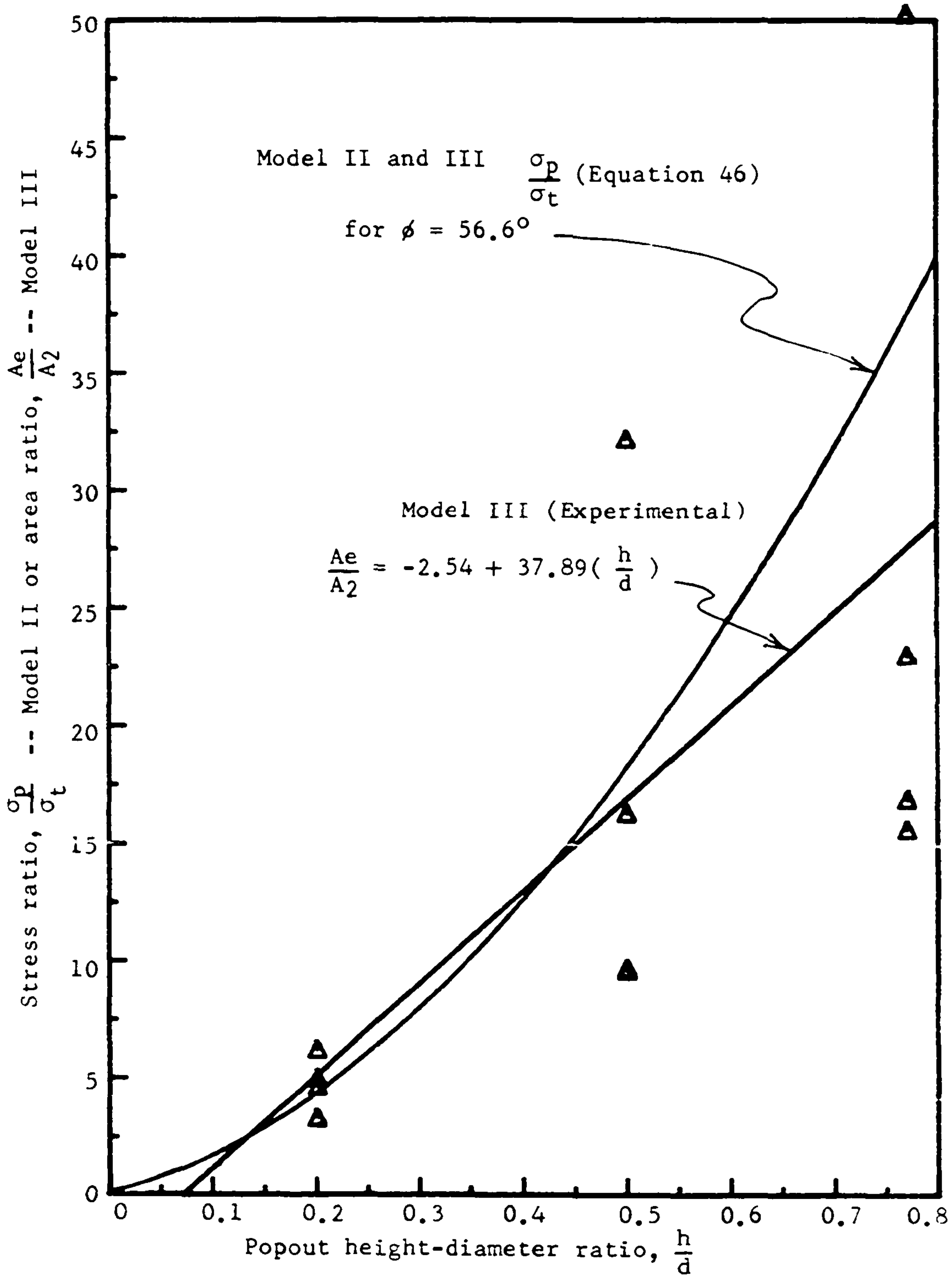

Figure 56. Comparison of experimental area ratio with theoretical stress ratio for portland cement popouts

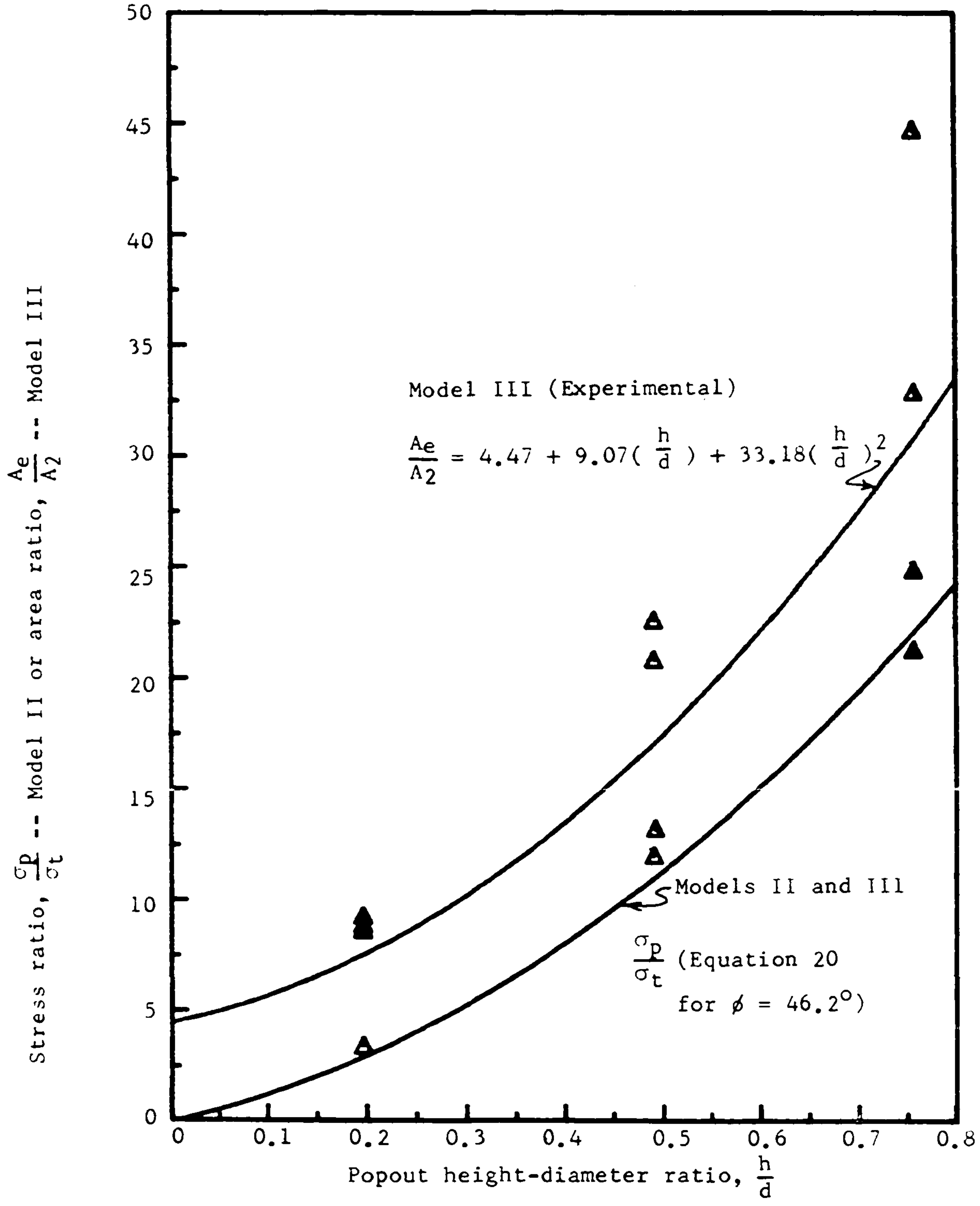

Figure 57. Comparison of experimental area ratio with theoretical stress ratio for plaster of Paris popouts

parabola for portland cement popouts reduced to a straight line. There is fairly good agreement between the stress ratios predicted from area ratios by Equation 80 and those predicted by equation 46.

If the concrete fails in simple tension the experimental area ratios determined would require much higher stress ratios than were actually measured.

Figure 58 compares the experimental popout stress ratio for portland cement to the theoretical relationships derived for Models I, II and III. Figure 59 compares the experimental popout stress ratio for plaster of Paris to the theoretical relationships derived for Models I, II, and III. The experimental stress ratios are much lower than predicted by Models II and III. The deviation from the predicted values increases as the height-diameter, h/d ratio increases. Model I seems to predict the popout stress ratio quite well for plaster of Paris but over-predicts for portland cement. This suggests that of the three models, Model I is the most acceptable for predicting popout pressure. Unfortunately the shape of the failure plane does not agree with the shape assumed in Figure 18 for Model I. Observed failure planes are like the one assumed for Model III shown in Figure 30.

Shape of the Popout Failure Surface

A photograph showing the shape of a mechanically induced popout failure surface is shown in Figure 60. Microphotographic slides of failure surface profiles were obtained, projected, and the profile traced to give the typical popout failure surfaces shown in Figure 61 for several water-cement ratios and for h/d values of 0.2, 0.5, and 0.77. Most

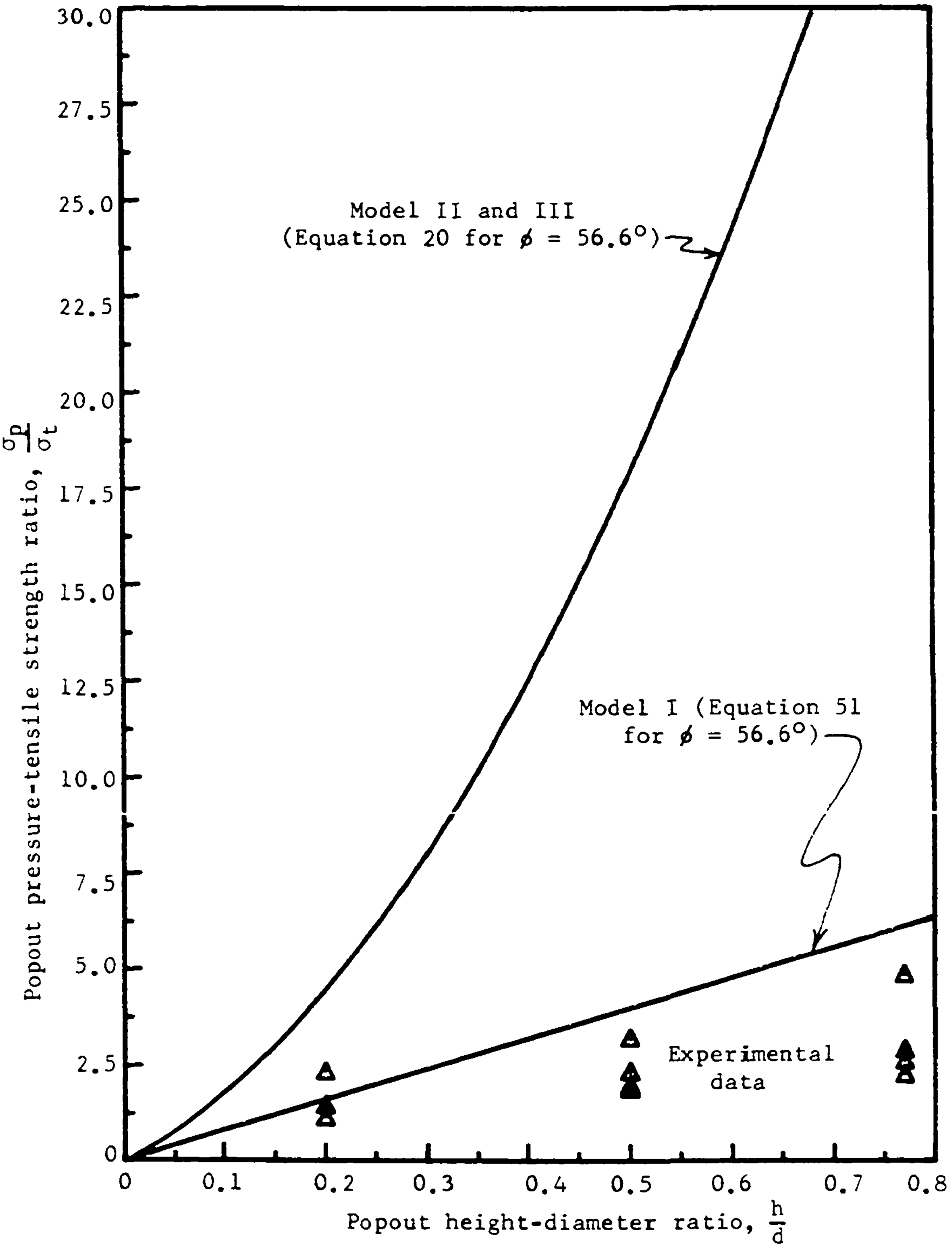

Figure 58. Comparison of experimental stress ratio with Model I and Model II theoretical stress ratios for portland cement popouts

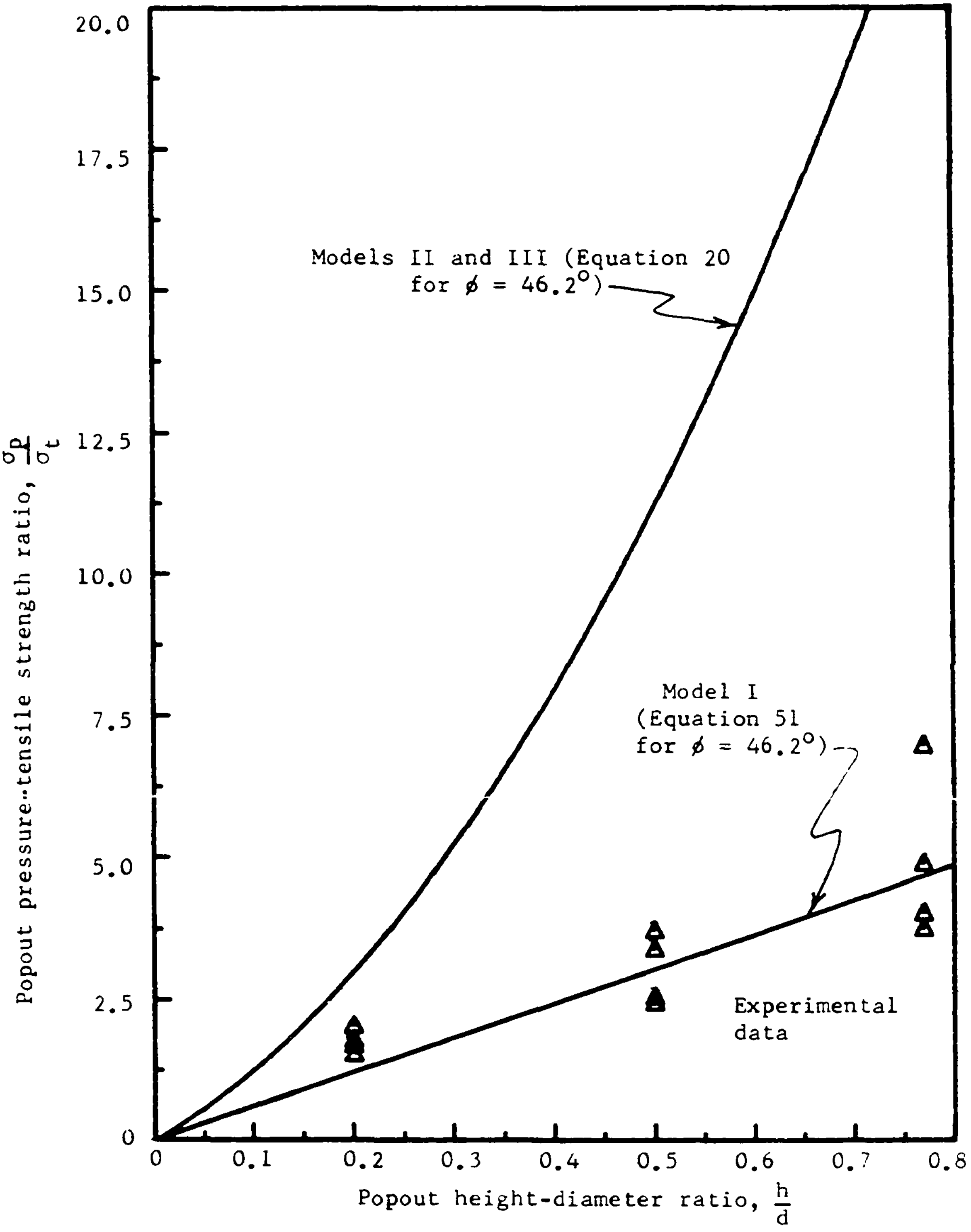

Figure 59. Comparison of experimental stress ratio with Model I and Model II theoretical stress ratios for plaster of Paris popouts

failure surfaces make an angle of between 30° and 40° with the vertical at the aggregate-mortar interface. This angle will be referred to in the following sections as the failure surface angle α.

All twenty-four of the popouts induced had a curved failure surface. In an effort to theoretically determine the geometry of the failure surface several approaches were tried.

Parabolic failure surface

A parabolic failure surface such as the one shown in Figure 62 was assumed. The popout of radius R is shown upside down for convenience in axis orientation. The parabola $y = kx^2$ has its vertex at the surface plane and is tangent to a radial line making an angle α with the horizontal surface. Since α can take on any value, the problem has an infinite number of solutions. The assumption used to provide a unique solution was that the ratio of the resisting area, A_r to the activating area, A_2 is a minimum. The failure surface of least resistance is the one where the ratio of the resisting to activating area, $\frac{A_r}{A_2}$, is a minimum. The resisting area is the area generated when the parabola in Figure 62 is rotated about a vertical axis through the center of the popout. The area was determined by Pappus' theorem. The activating area is the area given by $\pi d^2/4$ where d is as defined in Figure 62. The angle α was incremented and a computer was used to search for the α which would result in a minimum $\frac{A_r}{A_2}$ for a given h/d. Table 19 summarizes the results. The definitions of symbols are given in Figure 62. The distance P is in terms of a popout particle radius, R of 1.0.

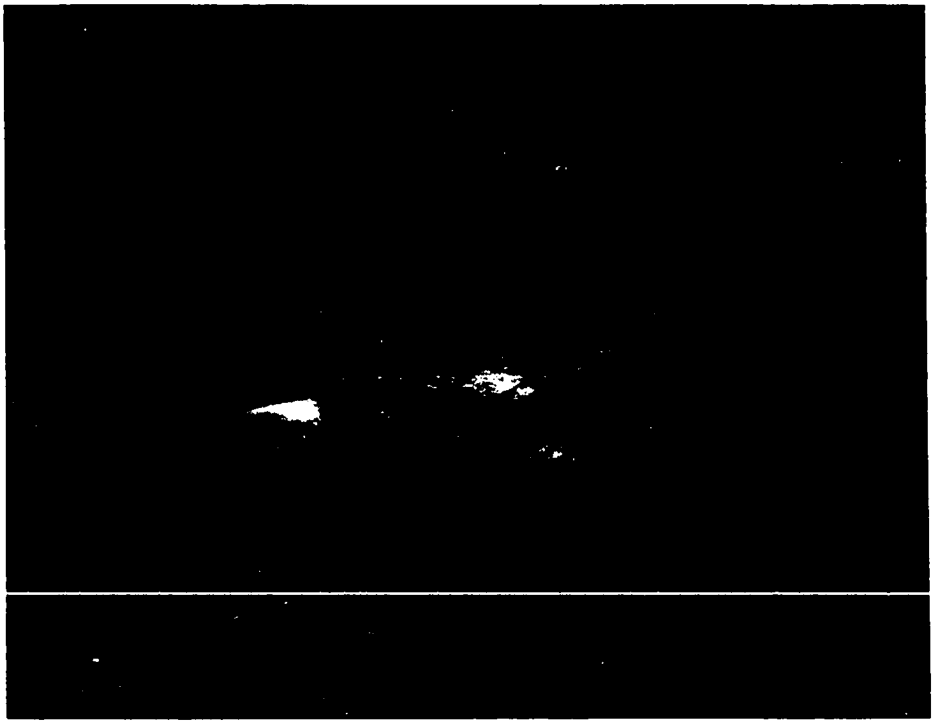

Figure 60. Mechanically induced popout

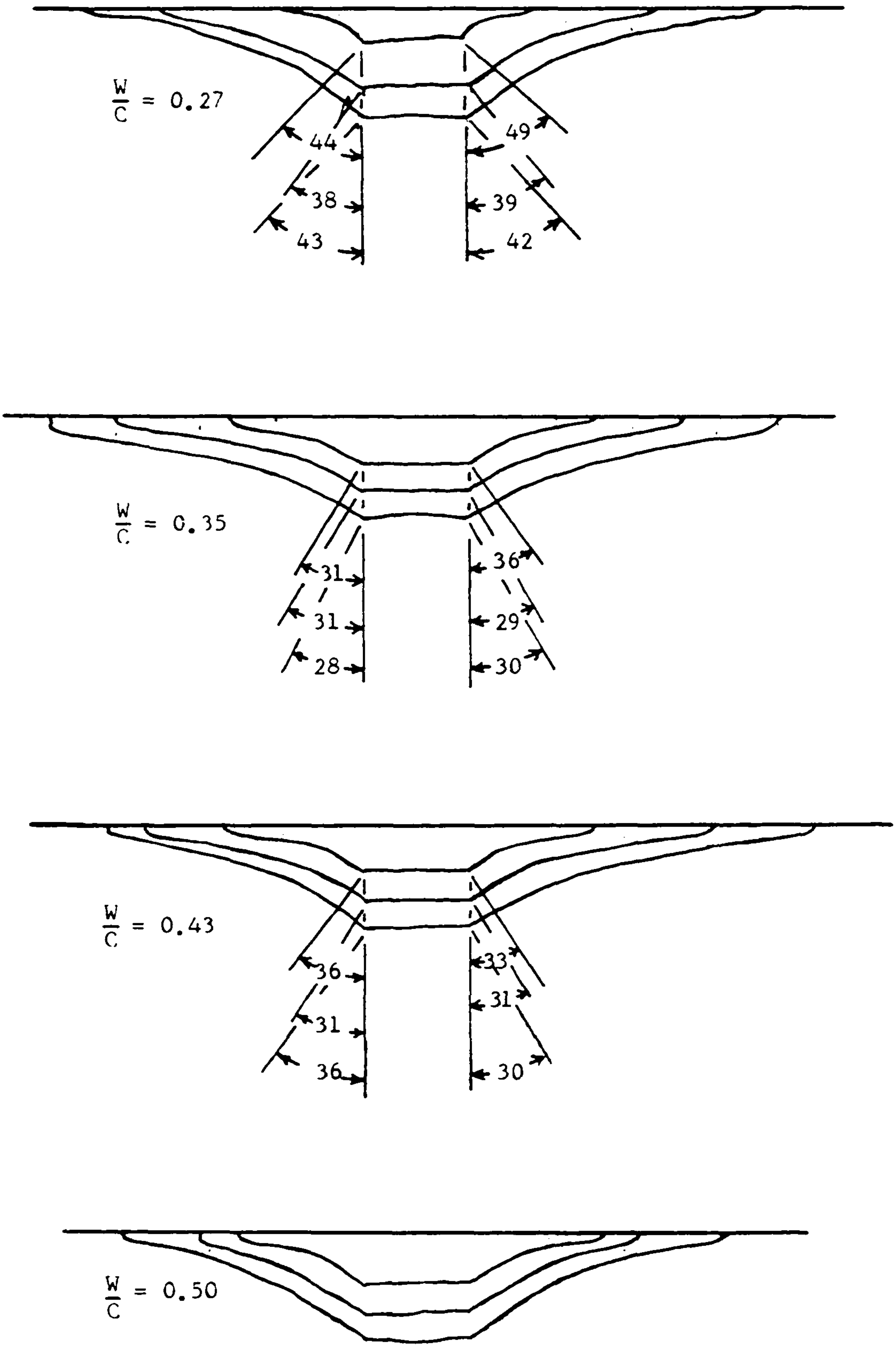

Figure 61. Profiles of mechanically induced popouts

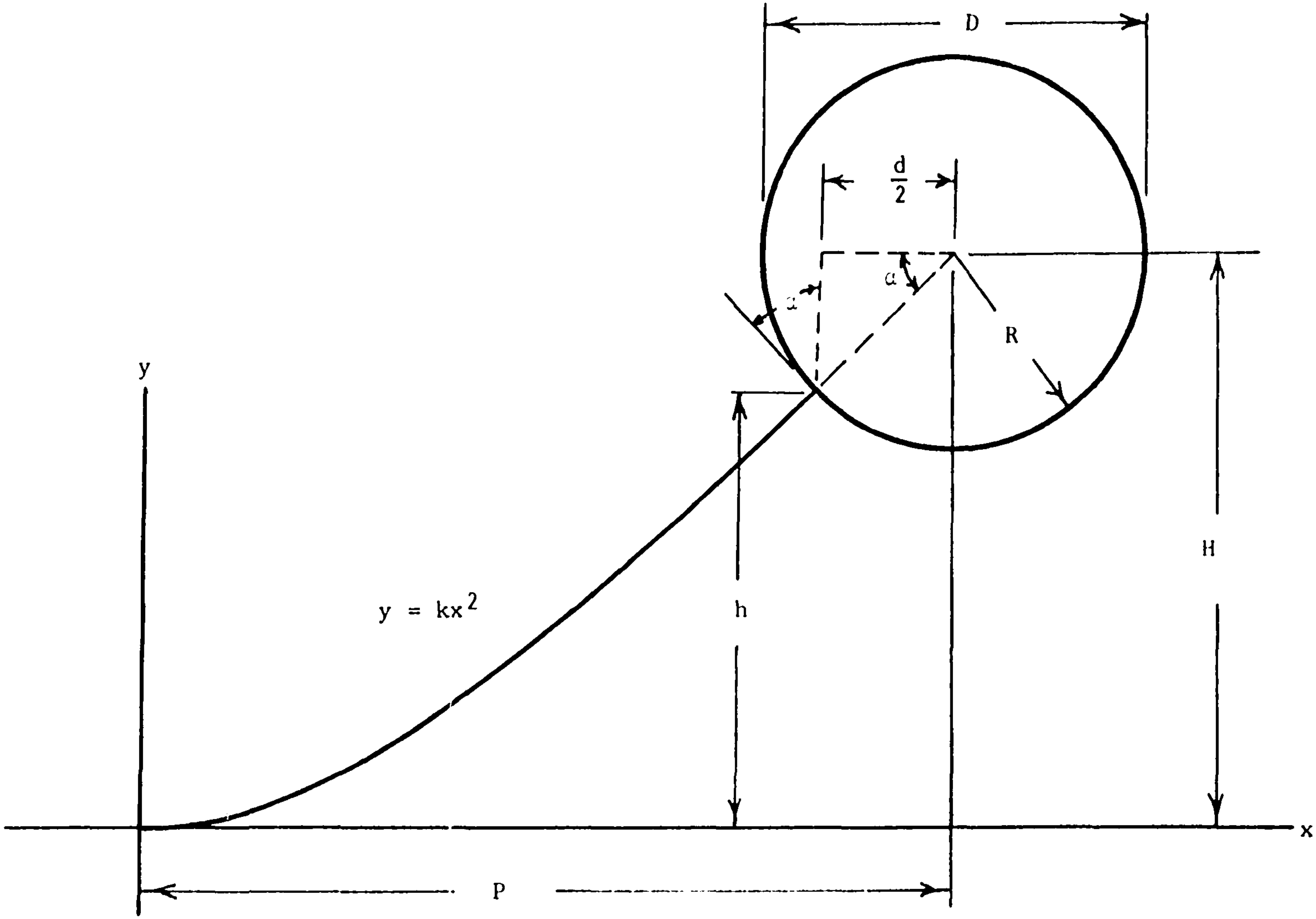

Figure 62. Parabolic popout failure surface

Table 19. Parabola shaped popout failure surface[a]

H/D	h/d	A_r/A_a	α	P[b]	k
10	22.7	2425	64.61	18.548	0.058
5	10.61	582	64.61	9.064	0.122
2	3.62	81.2	64.71	3.351	0.362
1	1.319	14.93	65.62	1.400	1.119
0.8	0.860	7.70	66.64	0.986	1.967
0.7	0.627	4.82	67.78	0.765	3.163
0.6	0.384	2.41	70.33	0.422	7.583
0.55	0.248	1.344	73.37	0.371	19.791
0.51	0.102	0.454	80.30	0.280	250.221
0.501	0.032	0.129	86.48	0.061	17144.077

[a] Definition of terms given in Figure 62.

[b] P is given in terms of a popout particle radius of 1.0.

Figure 63 shows the parabolic failure surface with a minimum resisting to activating area ratio, A_r/A_2 for two height to diameter ratios. The theoretical derived failure surface does not agree with those determined in actual experiments. The angle, α, actually observed is about 30° to 40° as shown in Figure 61. The α determined theoretically is about 70° for popouts with h/d values comparable to the range tested. As can be observed in Table 19, the lowest value of α approaches 64°

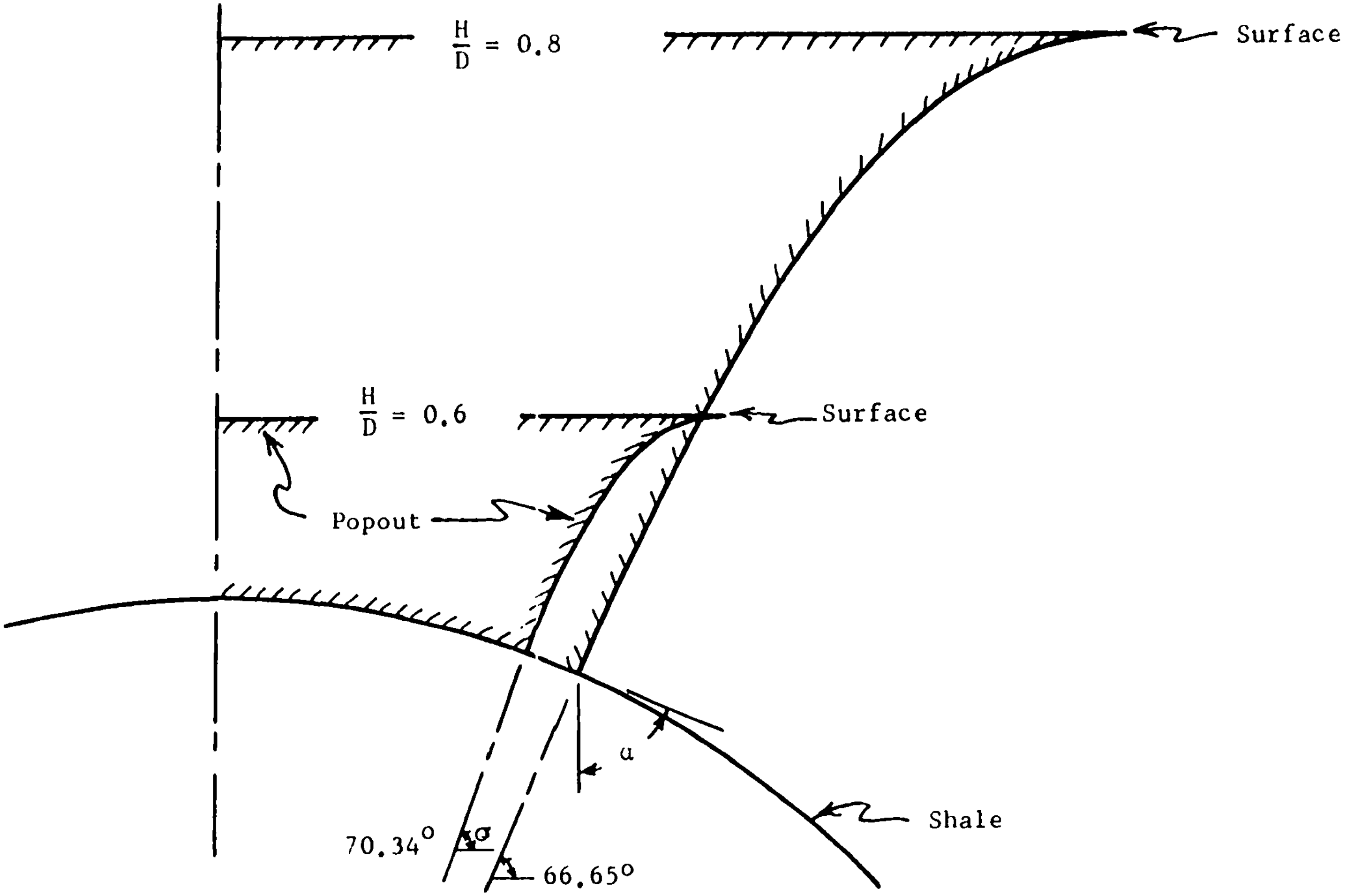

Figure 63. Parabolic popout failure surface based on minimum area ratio

for very deep embedment. Also the sharp curvature near the surface depicted in Figure 63 is not typical of the actual failure surfaces observed in Figure 61. For these reasons the parabolic failure surface is not representative of the actual failure surface, and another alternative must be examined.

Circular failure surface based on minimum area ratio

A circular failure surface such as the one shown in Figure 64 was assumed. The shale inclusion for this case was assumed to have an elliptical cross-section. The end conditions prescribed for the circular failure surface are that the circle is normal to the ellipse and tangent to the surface plane. Since an infinite number of failure surfaces can meet the end conditions prescribed, it was necessary to solve for the surface where the area ratio, A_r/A_2 was a minimum. A_r is the resisting area generated when the arc of a circle shown in Figure 64 is rotated about a vertical axis through the center of the popout. The area was determined by Pappus' theorem. The activating area, A_2, is the area given by $\pi d^2/4$ where d is as defined in Figure 64. The value d/2 was incremented and a computer was used to search for the d/2 which would result in a minimum A_r/A_2 for a given H/D. Table 20 summarizes the results. The critical failure plane parameters are defined for several H/D ratios and particle diameter to thickness ratios, D/T. If D/T = 1 the inclusion is considered spherical. D/T of 3 would mean the inclusion cross-section is an ellipse with the major axis 3 times the minor axis. D/T of 3 is about average as can be seen from Figure 42. From Table 20

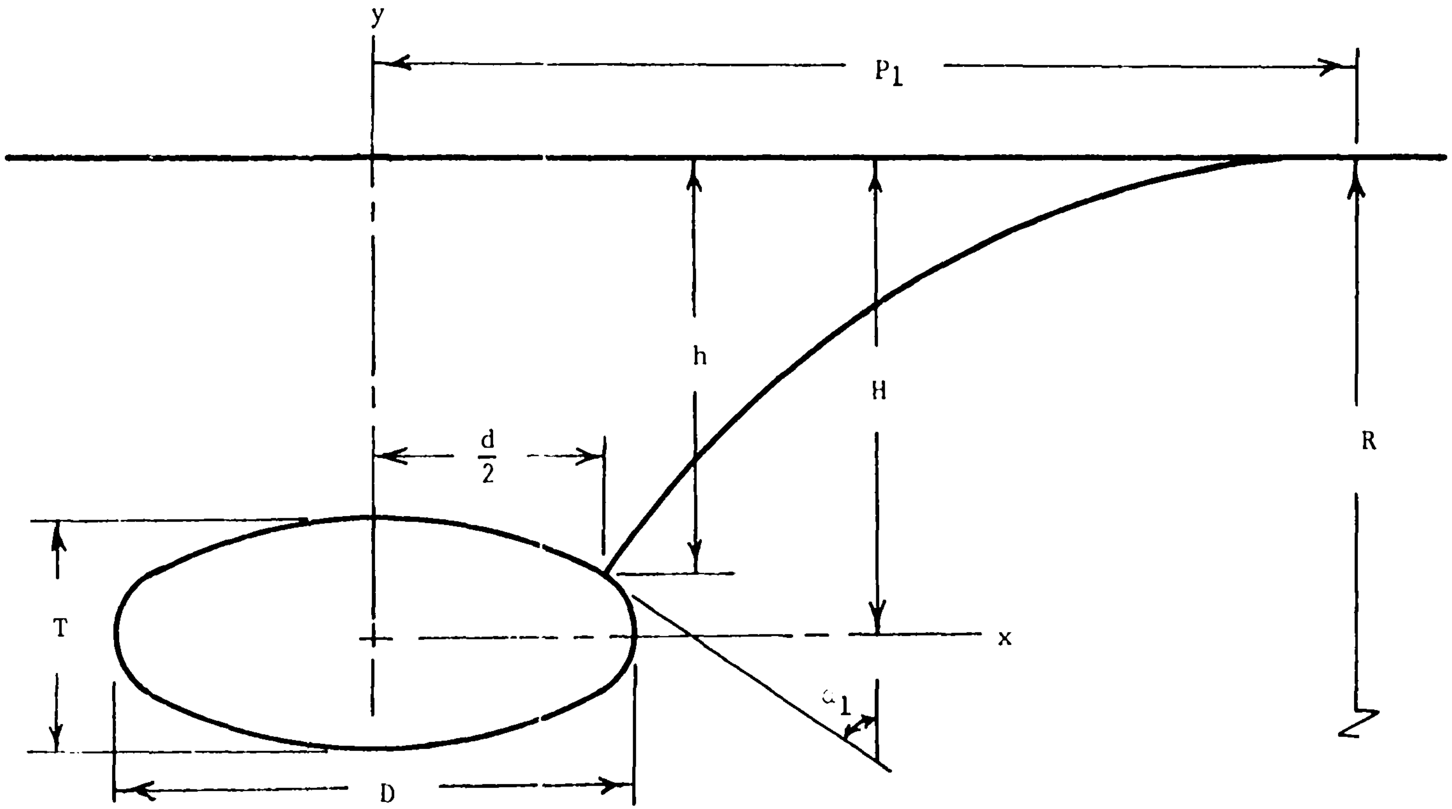

Figure 64. Circular popout failure surface

Table 20. Circular shaped popout failure surface based on minimum area ratio[a]

D/T	H/D	$d/2^b$	h/d	A_r/A_2	α_1	P_1^b	R^b
1	0.51	0.179	0.101	3.00	79.71	0.223	0.044
1	0.52	0.238	0.144	4.64	76.25	0.325	0.090
1	0.53	0.277	0.179	6.12	73.92	0.409	0.137
1	0.54	0.307	0.209	7.54	72.13	0.483	0.185
1	0.55	0.330	0.236	8.94	70.71	0.550	0.233
1	0.57	0.366	0.286	11.76	68.50	0.674	0.331
1	0.60	0.405	0.353	16.11	66.13	0.843	0.480
1	0.65	0.446	0.454	23.95	63.49	1.101	0.732
1	0.70	0.474	0.548	32.62	61.71	1.343	0.987
1	0.80	0.509	0.726	52.63	59.39	1.805	1.506
1	0.90	0.531	0.897	76.32	57.93	2.252	2.031
1	1.00	0.546	1.064	103.75	58.90	2.691	2.561
2	0.26	0.514	0.072	2.02	82.42	0.598	0.085
2	0.27	0.685	0.103	3.05	79.67	0.853	0.171
2	0.28	0.796	0.127	3.96	77.75	1.048	0.257
2	0.29	0.878	0.149	4.81	76.27	1.211	0.343
2	0.30	0.941	0.169	5.63	75.06	1.355	0.428
2	0.35	1.126	0.255	9.73	71.20	1.926	0.846
2	0.40	1.216	0.331	14.06	69.05	2.388	1.255
2	0.45	1.270	0.405	18.77	67.65	2.803	1.658
2	0.50	1.306	0.476	23.88	66.68	3.195	2.057
2	0.60	1.351	0.615	35.41	65.40	3.940	2.848
2	0.80	1.395	0.890	63.80	64.05	5.365	4.415
2	1.00	1.417	1.163	99.40	63.35	6.755	5.973
3	0.17	0.575	0.034	0.89	86.27	0.616	0.041
3	0.18	1.065	0.068	1.91	82.79	1.230	0.166
3	0.19	1.323	0.092	2.67	80.70	1.608	0.289
3	0.20	1.494	0.111	3.36	79.16	1.897	0.410
3	0.25	1.902	0.191	6.54	74.72	2.853	0.987
3	0.30	2.061	0.260	9.79	72.52	3.524	1.534
3	0.35	2.144	0.327	13.29	71.20	4.100	2.067
3	0.40	2.194	0.392	17.08	70.32	4.633	2.590

---

[a] Definition of terms given in Figure 64.

[b] Expressed in terms of T = 2.

Table 20. (Continued)

D/T	H/D	$d/2^b$	h/d	A_r/A_2	α_1	${P_1}^b$	R^b
3	0.50	2.252	0.519	25.58	69.26	5.639	3.622
3	0.60	2.283	0.646	35.36	68.62	6.606	4.642
3	0.80	2.315	0.899	58.76	67.77	8.492	6.663
3	1.00	2.332	1.152	87.37	67.62	10.351	8.673
4	0.13	1.066	0.036	0.95	86.04	1.148	0.082
4	0.14	1.703	0.063	1.76	83.29	1.944	0.244
4	0.15	2.050	0.083	2.39	81.51	2.446	0.400
4	0.17	2.443	0.116	3.53	79.08	3.131	0.701
4	0.19	2.661	0.145	4.61	77.44	3.626	0.988
4	0.22	2.849	0.186	6.24	75.77	4.209	1.403
4	0.25	2.959	0.224	7.91	74.64	4.699	1.805
4	0.30	3.064	0.287	10.87	73.42	5.420	2.459
4	0.35	3.123	0.348	14.07	72.65	6.082	3.100
4	0.40	3.161	0.409	17.53	72.13	6.714	3.733
4	0.50	3.206	0.531	25.41	71.48	7.933	4.985
4	0.60	3.230	0.552	33.94	71.11	9.121	6.226
4	0.80	3.255	0.894	54.59	70.71	11.457	8.690
4	1.00	3.268	1.136	79.49	70.50	13.771	11.142
5	0.11	2.002	0.046	1.24	85.10	2.203	0.210
5	0.12	2.606	0.067	1.86	83.04	2.997	0.394
5	0.13	2.967	0.083	2.40	81.61	3.540	0.580
5	0.14	3.209	0.099	2.90	80.60	3.957	0.758
5	0.15	3.383	0.113	3.39	79.59	4.299	0.932
5	0.17	3.612	0.140	4.37	78.20	4.853	1.268
5	0.20	3.807	0.178	5.84	76.78	5.513	1.753
5	0.25	3.969	0.238	8.42	75.37	6.419	2.531
5	0.30	4.051	0.298	11.20	74.54	7.223	3.291
5	0.40	4.130	0.416	17.43	73.67	8.718	4.781
5	0.50	4.166	0.534	24.57	73.23	10.152	6.251
5	0.70	4.198	0.769	41.62	72.82	12.953	9.164
5	1.00	4.213	1.122	74.16	72.59	17.098	13.501

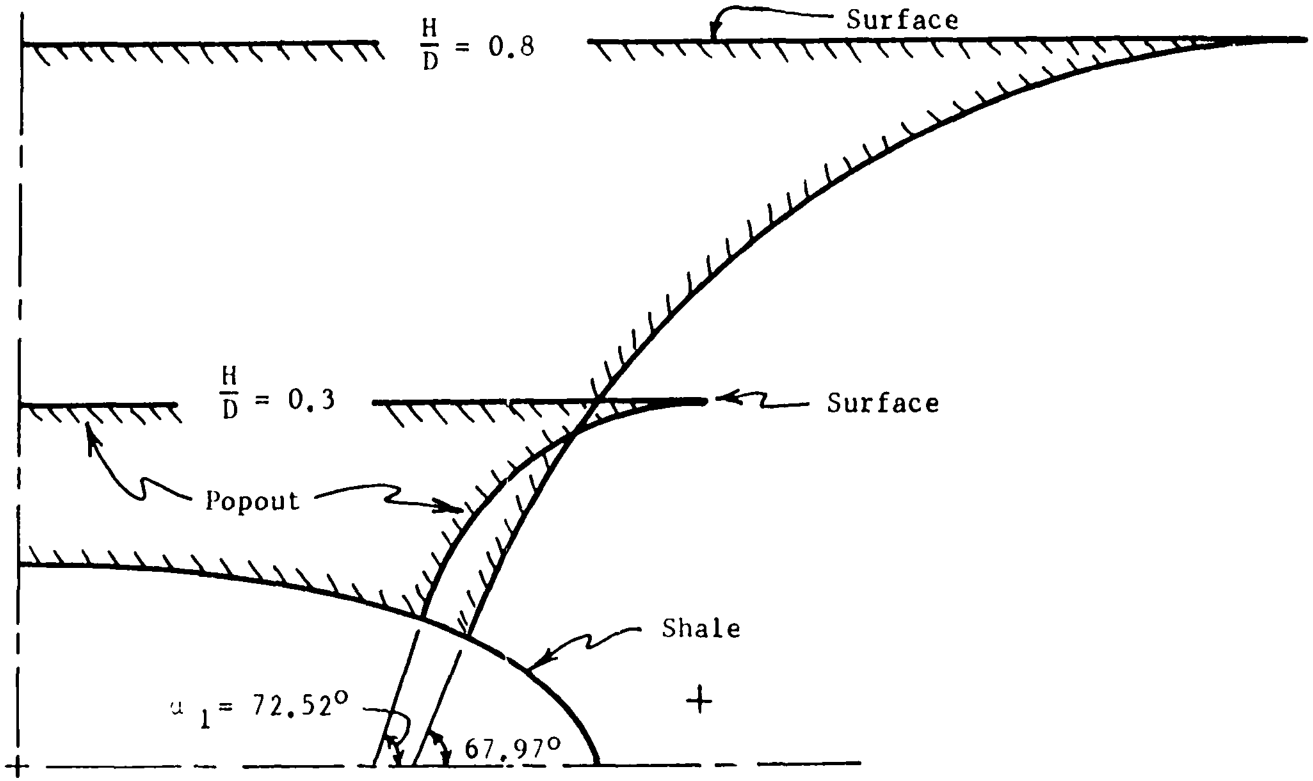

Figure 65. Circular failure surface based on minimum area ratio

the smallest value of failure surface angle, α_1, is 67.62° for a H/D of 1.0 and a D/T of 3. All other α_1 values for a D/T of 3 are larger than 67.62°. Typical failure surfaces as given by the failure surface parameters in Table 20 for H/D values of 0.8 and 0.3 and a D/T of 3 are given in Figure 65. Although the general shape of the failure surface seems to match the actual experimental failure surfaces shown in Figure 61, the angle α_1 is considerably larger and the radius of curvature is considerably less. The minimum area concept requires failure surface angles α_1 much higher than actually found. A third alternative must therefore be examined.

Circular failure surface based on minimum height-diameter ratio

The procedure was the same as in the preceding section except that the minimum h/d value determined by equation 95 was used to compute failure surface parameters rather than searching for the minimum area ratio, A_T/A_2. Table 21 summarizes the results for a D/T of 3. This method predicts angles α_1 that are too high for small h/d values and too low for high h/d values.

The experimental results shown in Figure 61 indicate that the failure surface angle is rather consistently between 30° and 40° with most angles being nearer 30°. All three theoretically derived failure surfaces discussed above over-predict this angle for h/d values in the range investigated.

There may well be a trade-off between stress concentration and the minimum area ratio concept. The stresses are undoubtedly more highly concentrated at the minimum radius of curvature of the elliptical inclusion. However, a horizontal tensile crack initiated at the minimum radius of curvature of an elliptical inclusion in a half space would require a failure plane with an infinite area. Tensile cracks undoubtedly occur for failure plane angles between 0° and 30°. However, the required fracture area is so large that the cracks terminate and additional cracks at higher α values form until the required failure surface area is reduced sufficiently to allow a popout to occur. The critical values for the failure plane angle α thus could come in the range 30° to 40° for the h/d values investigated.

Table 21. Circular shaped popout failure surface based on minimum height-diameter ratio[a]

D/T	H/D	d/2[b]	h/d	A_r/A_2	α_1	P_1[b]	R[b]
3	0.17	0.591	0.034	0.89	86.16	0.634	0.042
3	0.18	1.133	0.068	1.92	82.26	1.310	0.178
3	0.19	1.440	0.091	2.69	79.66	1.756	0.320
3	0.20	1.658	0.111	3.39	77.53	2.115	0.468
3	0.25	2.236	0.186	6.84	69.56	3.436	1.281
3	0.30	2.494	0.249	10.83	63.49	4.506	2.248
3	0.35	2.638	0.308	15.79	58.39	5.544	3.413
3	0.40	2.727	0.364	22.04	53.97	6.622	4.816
3	0.50	2.828	0.471	39.68	46.69	9.008	8.492
3	0.60	2.882	0.576	55.67	40.94	11.782	13.582
3	0.80	2.934	0.782	163.00	32.58	18.647	29.180
3	1.00	2.958	0.986	345.63	26.89	27.360	53.954

[a] Definition of terms given in Figure 64.

[b] Expressed in terms of T = 2.

Crack Propagation Factor

If the tensile stresses on the popout failure plane at the time of failure were everywhere equal to the tensile strength of the material the popout stress ratios would be those shown in Figures 56 and 57 and there would be good agreement between theory and experiment. The pressure required to cause a popout given by these area ratio values is, however, much larger than the pressures actually measured as shown by Figures 58 and 59.

Crack propagation is a logical explanation as to why experimentally measured popout pressures are far lower than predicted popout pressures. As the popout pressure builds up to a value less than twice the tensile strength of the material a tensile crack will form at the aggregate-mortar interface. Figure 32 shows why this first crack must appear before the popout pressure reaches the value of twice the tensile strength. For popouts with h/d values of 0.5 and 0.77 the measured popout pressure, σ_p, in Table 16 was always more than twice the tensile strength σ_t. Therefore, tensile cracks must be propagating for popout stresses over $2\sigma_t$ and the area resisting final catastrophic failure is much reduced from that observed on the actual popout. From Figures 58 and 59 it is obvious that the deviation of experimental stress ratios from theoretical stress ratios is a function of the height-diameter ratio, h/d. A crack propagation factor C_f was selected such that

$$C_f = C_1 \frac{h}{d} \tag{99}$$

where C_1 is a constant. Dividing the right side of equation 46 by the crack propagation factor C_f gives a predicted stress ratio of

$$\frac{\sigma_p}{\sigma_t} = \frac{K_1(\frac{h}{d})^2 + K_2\frac{h}{d}}{C_1\frac{h}{d}} \tag{100}$$

or

$$\frac{\sigma_p}{\sigma_t} = \frac{K_1(\frac{h}{d}) + K_2}{C_1} \tag{101}$$

which is the equation of a straight line. The values for K_1 and K_2 are given by equations 47 and 48. The value of C_1 was calculated from equation 101 using the actual experimental stress ratio $\frac{\sigma_p}{\sigma_t}$ values shown in Table 16. For portland cement the value of C_1 was 17.35 with a standard deviation of 2.11. For plaster of Paris the value of C_1 was 7.44 with a standard deviation of 1.73. It therefore appears that the value of C_1 is fairly independent of water-cement ratio for a given material. There is however a rather significant difference between the constant C_1 for portland cement and plaster of Paris. If average values of C_1 are used in equation 101 to obtain a new prediction equation the empirical equations are:

$$\frac{\sigma_p}{\sigma_t} = 2.47\frac{h}{d} + 0.75 \tag{102}$$

for portland cement, and

$$\frac{\sigma_p}{\sigma_t} = 3.29\frac{h}{d} + 1.33 \tag{103}$$

for plaster of Paris. The theoretical-empirical equations 102 and 103 are plotted in Figures 66 and 67 along with the experimental stress ratios. The 90 percent confidence belt is also shown. The curves for the

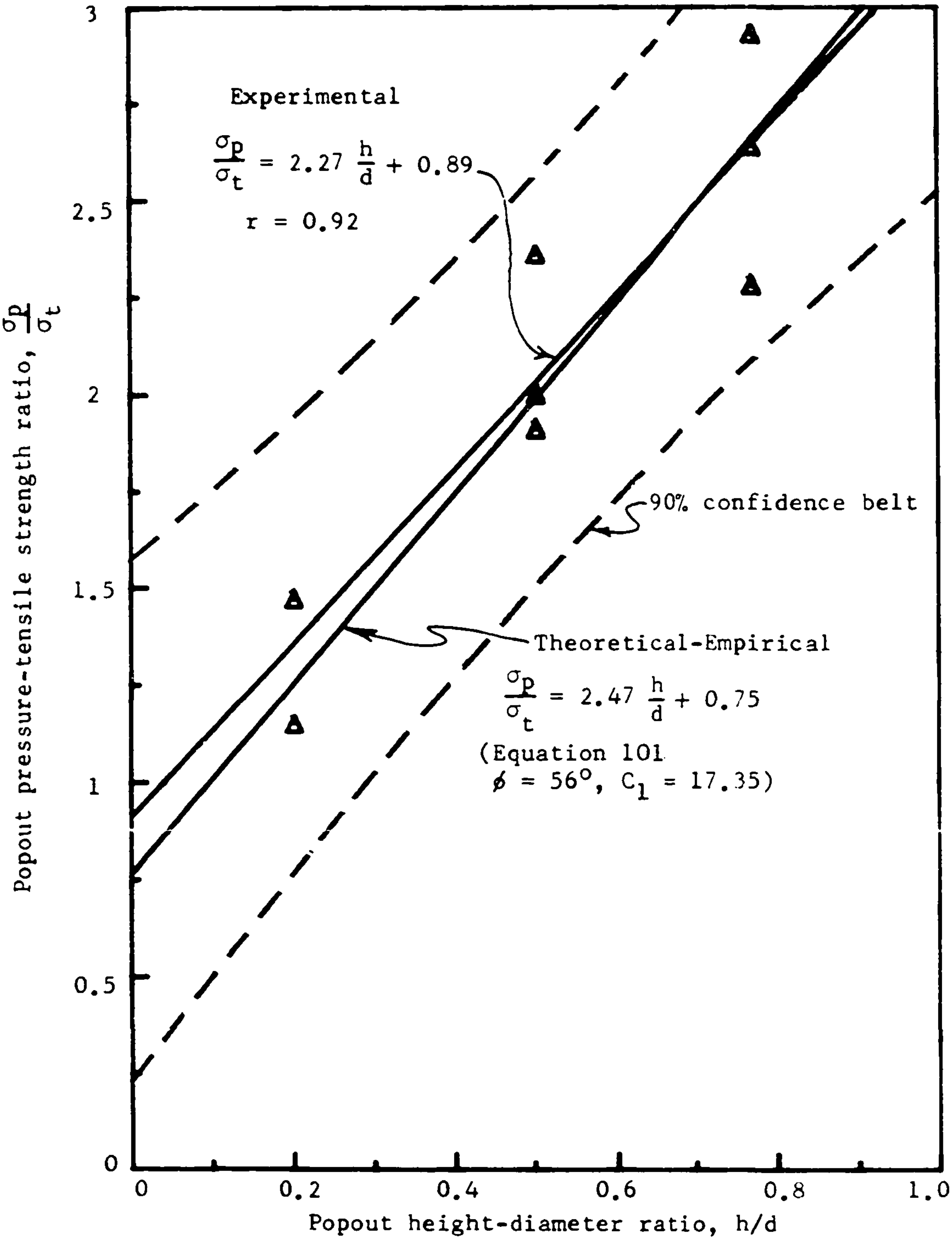

Figure 66. Comparison of theoretical and experimental popout stress ratio for portland cement

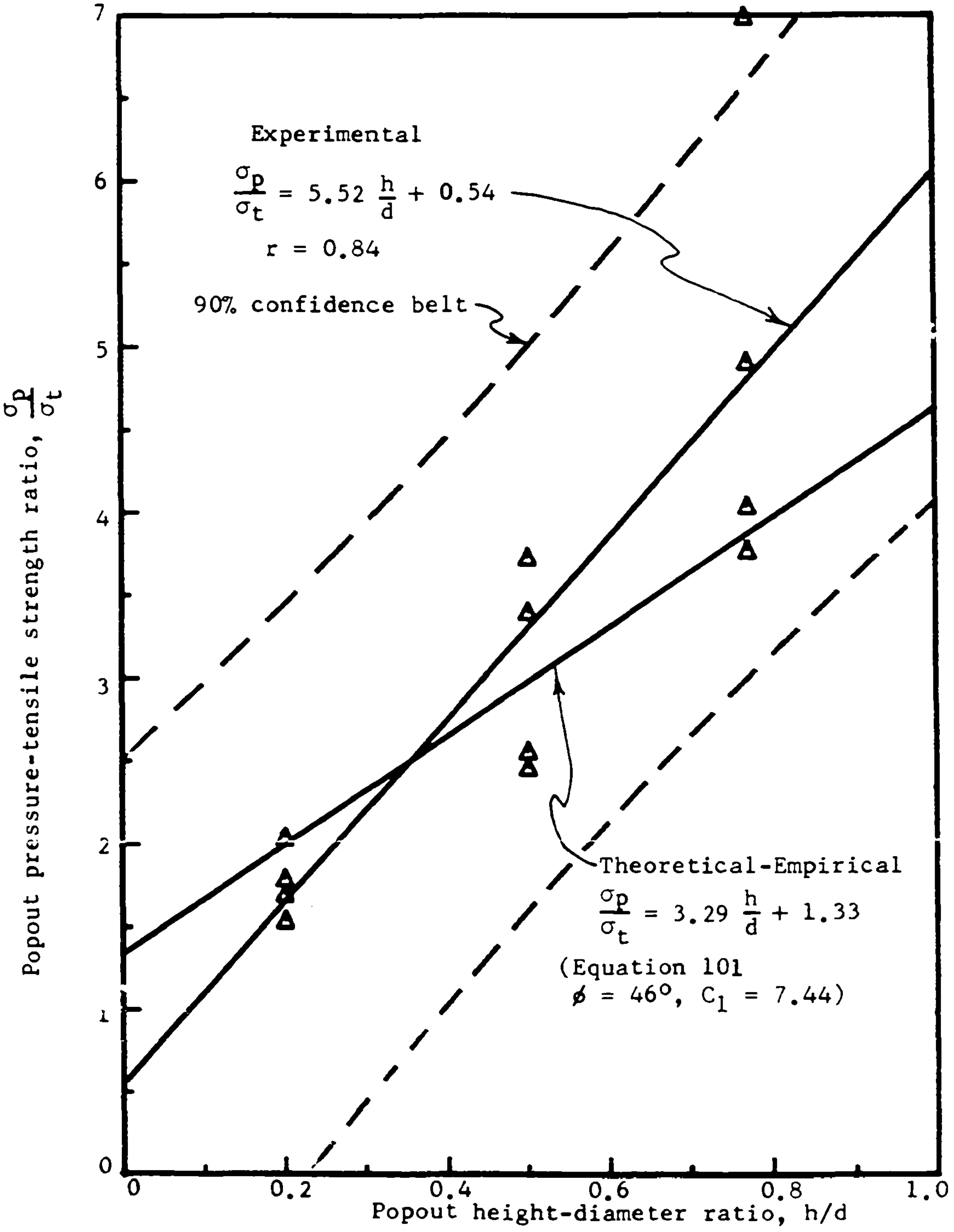

Figure 67. Comparison of theoretical and experimental popout stress ratio for plaster of Paris

theoretical-empirical equations are within the 90 percent confidence belt for both portland cement and plaster of Paris.

As stated above the constant C_1 in the crack propagation equation 99 is not dependent upon water-cement ratio, W/C. Also the friction angle ϕ as determined by equation 98 is independent of the water-cement ratio as shown in Table 18. The constants K_1 and K_2 given by equation 101 are also independent of water-cement ratio. The empirical equations (102 and 103) will, therefore, predict popout pressures for portland cement and plaster of Paris for all water-cement ratios in the range $0.27 \leq W/C \leq 0.50$.

CONCLUSIONS

1. The shape of the popout failure surface in hydrated portland cement and plaster of Paris can be represented by the theoretical surface generated when an arc of a circle is rotated about a tangent which coincides with the vertical axis through the center of the popout. The arc of the circle is tangent to the horizontal surface and subtends an angle of between 30° and 40° for all embedment depths investigated. The radius of curvature increases as embedment depth increases. In concrete popouts the curved failure surface profile is not always evident as the sand in the concrete often causes the feather edge to break off.

2. The theoretical stress equation developed to predict popout pressures is

$$\frac{\sigma_p}{\sigma_t} = \frac{4}{\tan^2(45-\frac{\phi}{2}} \left(\frac{h}{d}\right)^2 + \frac{4}{\tan(45-\frac{\phi}{2})} \left(\frac{h}{d}\right) \tag{46}$$

where σ_p is the pressure required to cause a popout to occur

σ_t is the tensile strength of the concrete

h is the height of the popout particle

d is the diameter of the base of the popout particle

ϕ is the internal friction angle of the concrete.

3. Popouts occur by progressive tensile failure in the vicinity of an expansive aggregate.

4. Because of the progressive nature of the failure when a popout occurs it is necessary to apply a crack propagation factor to the

theoretical popout equation. The resulting empirical equation is

$$\frac{\sigma_p}{\sigma_t} = 2.47\ h/d + 0.75 \tag{102}$$

for portland cement and

$$\frac{\sigma_p}{\sigma_t} = 3.29\ h/d + 1.33 \tag{103}$$

for plaster of Paris.

5. Empirical equations could be experimentally determined for materials other than portland cement and plaster of Paris. Such equations could be used to determine the force a seedling must exert on overlying soil in order to emerge, or the allowable force on an anchor bolt embedded in various materials.

BIBLIOGRAPHY

1. Stanton, T. E. Expansion of concrete through reaction between cement and aggregate. ASCE Proc. 66, No. 10: 1781-1811. Dec. 1940.

2. McConnell, D., Mielenz, R. C., Holland, W. Y. and Greene, K. T. Cement-aggregate reaction in concrete. ACI Journal, Proc. 19, No. 2: 93-128. Oct. 1947.

3. Jones, F. E. Reactions between aggregates and cements: I. Alkali-aggregate interaction - General. National Building Studies (Great Britain) Research Paper No. 14. 1952.

4. Neville, A. M. Properties of concrete. Sir Isaac Pitman and Sons Ltd., London. 1963.

5. Troxell, G. E., Davis, H. E. and Kelly, J. W. Composition and properties of concrete. 2nd ed. McGraw-Hill Book Co., New York, N.Y. 1968.

6. McConnel, D., Mielenz, C., Holland, W. Y. and Greene, K. T. Petrology of concrete affected by cement-aggregate reaction. In Application of geology to engineering practice. Pp. 225-250. The Geological Society of America, Berkeley, Calif. 1950.

7. Powers, T. C. and Steinour, H. H. An interpretation of some published researches on the alkali-aggregate reaction. Part I - The chemical reactions and mechanism of expansion. ACI Journal, Proc. 26, No. 6: 497-516. Feb. 1955.

8. Carman, P. C. Constitution of colloidal silica. Faraday Society Trans. 36: 964-973. 1940.

9a. Kalousek, G. L. Studies of portions of the quaternary system soda-lime-silica-water at 25°C. Journal of Research, National Bureau of Standards 32: 285-302. 1944.

9b. Moore, Walter J. Physical chemistry. 3rd ed. Prentice-Hall, Inc., Englewood Cliffs, N.J. 1962.

10. Hansen, W. C. Studies relating to the mechanism by which the alkali-aggregate reaction produces expansion in concrete. ACI Journal, Proc. 15, No. 3: 213-227. Jan. 1944.

11. Vivian, H. E. IV. The effect of expansion on the tensile strength of mortar. Scientific and Industrial Research Council (Melbourne, Australia) Bulletin 129: 67-73. 1947.

12. van Olphen, H. An introduction to clay colloid chemistry. John Wiley and Sons, Inc., New York, N.Y. 1963.

13. Olson, T. W., Handy, R. L. and Demirel, T. Design of a high pressure X-ray goniometer accessory and a high pressure consolidometer. Determination of swelling pressures of montmorillonites. Engineering Research Institute, Iowa State University, Ames, Iowa. 1972.

14. Franks, P. C. and Swineford, A. Character and genesis of massive opal in Kimball Member, Ogallala Formation, Scott County, Kansas. Journal of Sedimentary Petrology 29, No. 2: 186-196. June 1959.

15. Eitel, W. The physical chemistry of silicates. The University of Chicago Press, Chicago, Illinois. 1954.

16. Geologic Map of Iowa. Iowa Geological Survey, Williams and Heintz Map Corporation, Washington, D.C. 1969.

17. Selman, E. W. Humidity control by salt solutions. Unpublished M.S. thesis. Library, Iowa State University of Science and Technology, Ames, Iowa. 1933.

18. Handy, R. L. Quantitative X-ray diffraction measurements by fast scanning. Analytical Techniques for Hydraulic Cements and Concrete. ASTM STP 395: 30-47. 1965.

19. Mitchell, T. P. and Weese, J. A. Stress distributions analysed in bispherical co-ordinates. Journal of Applied Mechanics, Trans. 27, No. 4: 726-732. Dec. 1960.

20. Balla, A. The resistance to breaking-out of mushroom foundations for pylons. Fifth International Conference on Soil Mechanics and Foundation Engineering (Paris) Proc. 1: 569-576. 1962.

21. Vesic, A. S. Breakout resistance of objects embedded in ocean bottom. U.S. Naval Civil Engineering Laboratory (Port Hueneme, California) Report No. CR. 69.031, pp. 1-34. May 1969.

22. Timoshenko, S. and Goodier, J. N. Theory of Elasticity. 3rd ed. McGraw-Hill Book Co., New York, N.Y. 1970.

23. Malhotra, V. M. and Zoldners, N. G. Comparison of ring-tensile strength of concrete with compressive, flexural, and splitting-tensile strengths. Journal of Materials 2, No. 1: 160-199. March 1967.

24. Murphy, G. Similitude in Engineering. The Ronald Press Company, New York, N.Y. 1950.

25. Tinoco, F. H. Structural Properties of cement-stabilized soils. Unpublished M.S. thesis. Library, Iowa State University of Science and Technology, Ames, Iowa. 1963.

ACKNOWLEDGEMENTS

The research described in this dissertation was sponsored by the Engineering Research Institute, Iowa State University of Science and Technology and the following private and public agencies as part of programs for the improvement of concrete products:

Ames Ready-Mix Concrete Company, Ames, Iowa
Bell-Wood Construction Company, Indianola, Iowa
Clear Lake Sand and Gravel Company, Inc., Clear Lake, Iowa
Concrete Materials, Martin Marietta Corporation, Cedar Rapids, Iowa
Crown Concrete Company, Des Moines, Iowa
Eagle Iron Works, Des Moines, Iowa
Estherville Concrete Products Company, Estherville, Iowa
Fort Dodge Concrete Company, Fort Dodge, Iowa
Fred Carlson Company, Decorah, Iowa
Hallett Construction Company, Boone, Iowa
Ideal Sand and Gravel Company, Mason City, Iowa
Iowa State Highway Commission, Ames, Iowa
Iowa State University; President's Permanent Objective Committee, Ames, Iowa
Jack Stanley Company, Inc., Thurman, Iowa
King's Concrete Company, Cedar Rapids, Iowa
King, R. G. "Bob", Des Moines, Iowa
National Science Foundation, Science Faculty Improvement Fellowship Program, Washington, D.C.
Master Builders of Iowa, Inc., Des Moines, Iowa

The River Products Company, Iowa City, Iowa

Standard Ready Mix Concrete Company, Sioux City, Iowa

Walter N. Handy Company, Inc., Springfield, Missouri

Zeidler Concrete Products Company, Waterloo, Iowa

In addition to the above sponsors, the Missouri Portland Cement Company supplied low-alkali cement, Master Builders supplied the colored toppings, Walter N. Handy Co. supplied the fly-ash, and the finishing was done by Gar Mattingly, compliments of James Thompson and Sons, Ames,

The support provided by all of the above named agencies is gratefully acknowledged.

The encouragement, guidance and patience coupled with unwavering faith displayed by Dr. Richard L. Handy is greatly appreciated. Dr. Turgut Demirel's helpful review of difficult portions of the dissertation is gratefully acknowledged. The gentle jabs of encouragement from Dr. Jack L. Mickle will be appreciated in the near future.

To Ralph, Janette, Keith, Linda, and Paul for keeping our home so full of joy and happiness, my sincere thanks.

To my wonderful wife and queen, Luana, who provided encouragement, patience, and endured much sacrifice for this goal, my grateful appreciation and eternal love.

To Him who governs the infinite source of all knowledge and wisdom, my gratitude.